THE PHYSICS, DOSIMETRY AND MICRODOSIMETRY OF BORON NEUTRON CAPTURE THERAPY

by

ZAMIR GHANI

A thesis submitted to the
University of Birmingham
for the degree of
DOCTOR OF PHILOSOPHY

School of Physics and Astronomy
College of Engineering and Physical Sciences
The University of Birmingham
2012
March 2012

Abstract

There is a critical need to establish a clinically relevant, cell radiobiology based procedure to benchmark clinical and pre-clinical Boron Neutron Capture Therapy (BNCT) facilities. This data can be used to transfer safe working tolerance doses from nuclear reactor based clinical studies using differing beam characteristiscs and applied, by way of established radiobiology techniques, to developing accelerator based facilities.

A validated experimental and numerical procedure is described detailing macroscopic and microscopic dose calculations forming the basis of a protocol for the pre-clinical biological characterisation of the University of Birmingham's BNCT facility.

Fundamental reference dosimetric measurements have been carried out at the University of Birmingham's accelerator based NCT facility and the Massachusetts Institute of Technology (MIT) research reactor to characterise macroscopic and microscopic doses and derive correction factors for the irradiation of V79 cells incubated in boric acid and irradiated as monolayers. On and off-axis thermal neutron, fast neutron and photon doses have been measured and calculated with standard macroscopic dosimetry techniques (foils and ion chambers) from which normalised MCNPX calculations are used to derive perturbation factors and off-axis corrections for cell flask irradiations.

Microdosimetric correction factors are calculated for the boron dose component using Monte Carlo methods to simulate lithium ion and alpha particle tracks in semi-stochastic geometries representative of cell monolayer irradiations, incubated in a medium with 50ppm boric acid. Further simulations of recoil protons from nitrogen capture reactions allow for the calculation of correction factors for the non-uniform distribution of the nitrogen dose at the cellular level.

ACKNOWLEDGEMENTS

I would like to thank Prof. Stuart Green for offering me the opportunity to take part in this extraordinary study. It has quickly become one of the most important things in my life, next to my family.

My warmest thanks are extended to my supervisors Prof. Stuart Green and Dr. Cecile Wojnecki for their unwavering support, care and attention throughout my time at the University. It is evident to me that I would never have been able to complete this work without their help, due diligence and kindness.

To my friends; fellow students; colleagues, past and present, it has been an honour working alongside you. Ben, Dan and Francesca, your company, support and advice has been indispensable. My thanks are also extended to Arif and Adam.

This project would not have been possible without the support of Professor Cruickshank, Dr. Detta and Dr. Ngoga and the skill of John and Greg. Last but not least, I would like to thank Dr. Michael Wilson, Dr. Richard Hugtenburg and Prof. David Parker for an inspirational Masters course that led me to this point in my life.

Contents

Chapter 1:

Chapter 2:

Chapter 3:

CHAPTER 4:

Chapter 5:

Chapter 6:

Chapter 7:

Chapter 8:

Chapter 9:

Chapter 10:

Chapter 1

INTRODUCTION

Brain tumours and tumours of the central nervous system form 2% of cancers in the UK. With Grade IV Glioblastoma multiforme (GBM) having amongst the poorest prognosis, few patients surviving more than a year.

It was proposed soon after the discovery of the neutron, by Chadwick in 1932, that neutrons could be used as a means of treatment for deep-seated tumours.[1] It was believed that this could be done whilst sparing large doses to healthy tissue, provided that a pharmaceutical of sufficiently high neutron capture cross section could be delivered to the target of interest.

Trials in the 1950s and 60s proved unfruitful, primarily due to the poor localised delivery of the boronated compound and poor, very thermal, beam spectra. This led to larger than acceptable doses being administered to healthy brain tissue. However, with the development of Sulfhydryl Borane $Na_2B_{12}H_{11}SH$ (BSH) and Boronophenylalanine (BPA) the possibilities of improved targeted therapy for Glioblastomas became viable once again.

BNCT amongst targeted cancer therapies is unique in its nature and deployment. The localisation and time dependence of boron loading and its variable uptake in not only tumour cells but also healthy tissue leads to a great deal of heterogeneity on both macroscopic and microscopic estimates of boron distribution and physical dose delivered by a complex mixed field of radiations.

In order to assess the feasibility, or even to plan clinically relevant treatments using boron loading agents, a diverse set of disciplines is required to understand the critical needs and effects of such a treatment. Fields including physics, nuclear engineering, biochemistry, neuroscience, neurosurgery and radiation biology have to come together to fully plan for and comprehend the outcomes of such a complex therapy.

---

[1] Gordon Locher - 1936

The drug most apt, showing the highest intracellular selectivity and preferential uptake between tumour and healthy tissue is Boronphenyalanine (BPA). This pharmaceutical consists of boron, the vital target of neutron capture therapy, compounded or bonded with phenylalanine, an essential amino acid required for normal metabolic function. Phenylalanine transport and metabolism is known to be raised in high grade brain tumour patients and thus serves as the ideal Trojan horse to carry a seemingly innocent, inert and non-toxic element, which is virtually indistinguishable in its transport from its analogue amino acid, into the local environment of a greedy and ravaging malignant tumour mass or even a single neoplastic proliferating cell. Thus, priming it for irradiation and resulting localised cell death favourably biased towards tumour cells.

Concentrations of BPA have been experimentally determined to be ~ 15 μg/g in healthy brain tissue to 52.5 μg/g in tumour tissue. Clinical trials currently underway at the Queen Elizabeth University Hospital Birmingham show the possibilites of even higher uptake ratios and add stronger than ever support for this treatment modality.

1.1 Physical Dose Delivery

In the course of a typical BNCT treatment of GBM brain tumours, BPA is administered to the patient intravenously or through the carotid artery, entering the circulatory system and in so doing passes by the blood brain barrier. The blood brain barrier being a set of tightly packed endothelial cells which separate brain matter from the circulatory system and the rest of the body. This barrier serves to selectively transport useful biochemicals necessary for brain function and repair whilst rejecting almost everything else. It is common for GBM patients to have leaky blood brain barriers in and around the location of the malignancy, thus a suitably loaded compound can be actively transported as well as passively ‘leaked’ across the brain’s extremely resistant protective barrier.

Once preferential uptake of the pharmaceutical has taken place a waiting period follows, post infusion, for the drug levels in blood and healthy tissue to diminish whilst remaining high in tumour tissue. Figure 1.1 shows a typical, clinically measured, BPA mediated drug profile in blood and brain, clearly showing the levels of boron in tumour remain high long after BPA infusion has stopped (at 120 minutes). After the waiting period, the next phase of the treatment is to deliver a high flux of thermal neutrons to the tumour cells. This cannot be achieved without delivering a high thermal neutron flux to a large volume of the brain, but with boron having a much higher neutron capture cross section than that of normal tissue, much of the physical dose is delivered to the tumour (boron rich) region.

In order to have a high flux of thermal neutrons in the region of the brain to be treated, it becomes necessary to target the patient with a flux of higher energy neutrons (epithermal). These in turn become moderated as they pass through scalp and skull, ultimately delivering the required thermal neutron dose to which boron reacts so favorably.

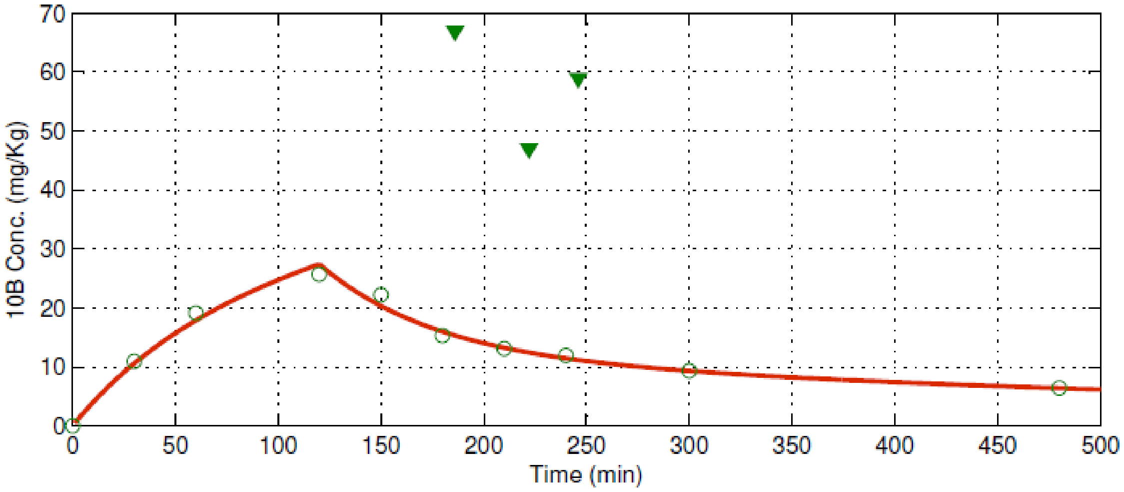

Figure 1.1 A typical pharmacokinetic Boron profile in blood (red line) and brain tumour (green triangles).

Boron, having an extremely high thermal neutron capture cross section, 3838 barns, readily captures and undergoes alpha decay with thermal neutrons. The reaction being:

$$^{10}\mathrm{B} + n \rightarrow {}^{7}Li + {}^{4}He + 2.79\mathrm{MeV}\ (6\%\ \text{of the time}) \qquad 1.1$$

$$^{10}\mathrm{B} + n \rightarrow {}^{7}Li^{*} + {}^{4}He + 2.31\mathrm{MeV}\ (94\%\ \text{of the time})$$

$$^{7}Li^{*} \rightarrow {}^{7}Li^{*} + \gamma\ (0.478\ \mathrm{MeV})$$

The products of the reaction depositing their energies with ranges of ~9μm for ^{4}He and ~6μm for ^{7}Li, i.e. comparable to that of a typical GBM cell (~10μm). This is sufficient to cause a lethal dose in most cases by virtue of a double stranded DNA break. Other dose components and microdosimetric effects will be described later in the thesis.

Before treatment planning can be embarked upon, a necessary step is to study and understand the lethality of the complex mixed radiation field to tumour and more importantly healthy tissue cells, which both encounter this mixed field at varying rates and mixes during therapy.

1.2 Scope of the current work

The objectives of the current study were to carry out fundamental reference dosimetric measurements and calculate macroscopic and microscopic correction factors for cell survival experiments in order to aid the development of a cell-based radiobiology protocol to provide essential data on the safety and efficacy of epithermal neutron beams for BNCT in advance of clinical trials.

To provide the macroscopic and microscopic dosimetry for the first of a validated protocol for the pre-clinical biological characterisation of BNCT facilities of varying dose rate and beam characteristics, by carrying out measurements at the Birmingham epithermal facility and the variable dose rate MITR-II research reactor at the Massachusetts Institute of Technology.

The broader intent of the research being to establish a clinically relevant, cell radiobiology based procedure for all BNCT facilities to be able to benchmark their beams against.

In order to fulfill this objective, work was carried out to analyse and refine dosimetric practices in the only functioning, at the time of this work, accelerator delivered epithermal neutron beam in the world.

The presence of the foils in the neutron flux which they are trying to measure causes ‘flux depression’ and ‘self shielding’ i.e. the measured flux is perturbed as measurements are being made. Correction factors for flux depression and self shielding for solid gold and manganese foils have been meticulously calculated and measured for the Birmingham facility and are the subject of a poster presented at the international Conference on Neutron Capture Therapy [Appendix A: ‘Neutron self-shielding effects and correction factors for foil activation measurements used in BNCT dosimetry']. The results of the measured correction factors showing extremely good agreement with simulations done with MCNPX.

Various beam monitors are used to monitor and quantify the patient dose; a Keithley electrometer is used to measure the integrated proton current onto the target, a Geiger counter to monitor the gamma ray field, and two fission chambers, a primary and a secondary, to monitor the thermal neutron flux near the beam exit port. The change in trend of neutron yields as measured by the Keithley electrometer and fission chambers over several years, clearly shows a drift in the calibration voltage and also hints at movement in the monitor chambers and beam collimation issues. The subject of which was presented at ICNCT13 in the form of a poster [Appendix A: 'BNCT beam monitoring, characterisation and dosimetry'] addressing the stability of the monitor chambers and to relocate them to a more stable, lower count rate environment.

A dedicated transport code capable of simulating stochastic cell geometries, with variable boron loading was developed to calculate correction factors) for microscopic dose inhomogeneities in boron and nitrogen distributions.

Some of the work done over the past years has been summarised and reported in the form of three posters presented at the International conference on Neutron Capture Therapy [ICNCT13, October 2008], and two oral presentation given at ICNCT14, November 2010, the abstracts of which can be found in Appendix A.

1.3 Additional work carried out during the research period includes:

1. Compared (calculated) in air beam characteristics with other facilities [C-BENS (Japan) / MIT (USA)].
2. Corrected foil measurements for yield variability and current drifts during irradiations.
3. Modeled a thermal pile irradiation facility and validate MCNP calculations in an epithermal and thermal beam simultaneously with foil measurements.

4. Routinely carried out proton beam energy calibrations and calculate, the spread in the proton energy impinging on the thin natural lithium target.
5. Collaborated with visiting research groups for SPECT imaging and ion chamber inter-comparison.[Appendix A]
6. Assessed the possibility of employing a lead reflector over the existing graphite reflector and look again at Lithium filters as a means of shifting the depth dose curve. [Appendix B]
7. Calculated the impact of impurities in lead on build-up in activity in the beam shaping assembly following extensive irradiation.
8. Carried out radiation inventory calculations on all components in the beam shaping assembly using MCNPX and FISPACT.
9. Calculated yield losses due to ion implantation in target. [i.e. LiH targets of varying ratios].
10. Calculated the feasibility of Accelerator based Tc generator, project carried forward by The University of Manchester.
11. Calculated organ doses to a voxelised human phantom – VIP man, in the exisiting Birmingham facility and study possible improvements in treatment room shielding. [Appendix A]
12. Wrote a dedicated transport code capable of simulating stochastic cell geometries, with variable boron loading- readily biased for LAT transporter expression, scoring doses and survival from ion traversals.
13. Implemented the GSI Local effect model in Matlab for further analysis of preclinical data and to optimise a mixed regimen of BNCT and radiotherapy.
14. Assisted in in-vitro boron uptake study with preloading and transport markers.
15. Assisted in the CRUK funded pharmacokinetic drug study underway at the Queen Elizabeth, University hospital, Birmingham – tumour sample collection and imprinting for sims analysis. [Appendix A]

16. Modelled the time course levels of Boron in blood from patient trials using Simulink and Matlab to create generic open two compartmental, pharmacokinetic, models to help analyse patient outcome and serve as a boron/blood model for future treatments. [Appendix A]
17. Addressed and calculated corrections for cell density in addressing mass spectrometry results of boron levels in tumour and brain around tumour samples. [Appendix A]
18. Carried out preliminary analysis of the Boron levels in extra cellular fluid (in brain) through different means of drug delivery and blood brain barrier disruption. [Appendix A]
19. Analysed imaging data for LAT transport and sought correlation with boron uptake in tumour samples. [Appendix A]
20. Assisted in analysing Boron distributions in tumour/brain around tumour from SIMS images. [Appendix A]
21. Assisted in the supervision of Masters student projects, neutron radiography, room shielding, proportional counter measurements in neutron and proton beams/data analysis, Fluka / MCNP BSA simulations and foil irradiations.

Chapter 2

NEUTRON GENERATION, SOURCE MODELLING AND THE BIRMINGHAM BEAM SHAPING ASSEMBLY

2.1 Neutron Generation

Neutrons are generated, at the Birmingham NCT facility, by accelerating protons to energies of 2.8MeV at a current of 1mA striking a natural lithium target inducing the reaction $^{7}Li(p,n)^{7}Be$. This produces a neutron source intensity of $1.37x10^{12}$ n/s. Although this is of high yield it is still relatively soft in its spectrum when compared to other neutron generating reactions (table 2.1). Thus, it does not require substantial moderation, but the lithium target does have the draw backs of a low melting point (180°C) and poor thermal conductivity. This complication, which would result in the target blistering at high currents and for extended usage, has been overcome at the University of Birmingham, by the implementation of a thick target construction and a pressurised D_2O cooling jet system to maintain a solid target despite high beam currents.

Reaction	***E*(particle)**	***Q*-value**	**$E_n(max)$**	**$\langle E_n \rangle$**	**Neutron yield**
	(MeV)	**(MeV)**	**(MeV)**	**(MeV)**	**$(mA\ S)^{-1}$**
$^{7}Li(p,n)^{7}Be$	2.5	−1.64	0.78	~0.6	9.091×10^{11}
$^{9}Be(p,n)^{9}B$	4–5	−1.85	2–3	~1.6	$0.53–1.2\times10^{12}$
$^{9}Be(d,n)^{10}B$	1.5	4.36	5.9	1.66	3.3×10^{11}
$^{13}C(p,n)^{13}N$	5	−3	2	1.16	3.8×10^{11}
$^{13}C(d,n)^{14}N$	1.5	5.33	6.8	1.08	1.9×10^{11}
$^{12}C(d,n)^{14}N$	1.5	−0.28	1.2	0.55	6×10^{10}
D–D	0.16	3.27	2.9	2.45	6.6×10^{8}

Table 2.1.Properties of various neutron sources considered for BNCT [1]

An undesired product of the ^{7}Li(p,n)^{7}Be reaction are the gamma rays [2]:

i. $431\,keV\ \gamma-rays\ are\ produced\ by\ {}^7Be*\ decaying\ to\ its\ ground\ state.$
ii. $478\,keV\,\gamma-rays\ are\ produced\ by\ the\ scattering\ reaction\ {}^7Li(p,p')\,{}^7Li*(478\,keV).$
iii. $^7Be\ decays\ by\ electron\ capture\ to\ {}^7Li,\ with\ a\ half-life\ of\ 53.3\ d.\ Only\ 10.35\%\ of\ decays\ produce\ a\ 478\ keV\ \gamma-ray.$

These gamma rays require attenuating and this is achieved by having a cylindrical annulus of lead shielding surrounding the target and backing plate in the direction of the patient.

For 2.8MeV proton irradiation, neutrons emitted from the ^{7}Li(p,n)^{7}Be reaction have a maximum energy of 1.2MeV and in order to be of therapeutic value, they need to be slowed down to ~ 10keV (i.e. epithermal). Hence, there is a need for moderating material to be placed between the target and the beam exit port, in order to maximize dose rate and achieve workable epithermal yields. We need to confine to the best of our ability, these neutrons, and channel them towards the beam exit port. Thus the moderator is surrounded by a ‘reflector’ material in all but the beam exit direction.

2.2 Classical Kinematics

Much research has gone into designing and optimizing the exisiting University of Brmingham facility. The results of published research led to the current build of the pre-clinical facility [2][3]. Amongst its unique design concepts was that a vertical beam of protons of 2.8MeV striking a natural lithium target used to produce a horizontally extracted beam of neutrons. This ‘beam’ of neutrons is moderated by 25cm of Fluental^{TM} to produce an extremely good spectrum at the beam exit port for treatment of deep seated head tumours.

From classical kinematics it is possible to determine the neutron energies and spatial distribution from the target as a function of incoming proton energy:

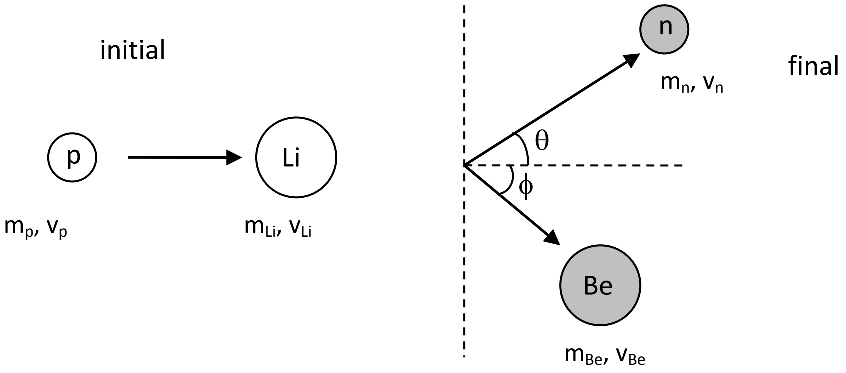

Figure 2.1. Schematic diagram for the Li(p,n)Be nuclear reaction with a proton incident upon a lithium target nucleus at rest in the laboratory coordinate.

In the non-relativistic limit, the kinetic energy is given by $T=1/2mv^2=p^2/2m$

The inelastic scatter of two bodies in the lab frame, as depicted in figure 2.1, when conserving linear momentum and energy, is governed by the kinematics equation:

$$T_p(\frac{m_p}{m_{Be}}-1)+T_n(\frac{m_n}{m_{Be}}+1)-\frac{2\sqrt{m_p m_n}}{m_{Be}}T_p^{1/2}T_n^{1/2}\cos\theta-Q=0 \tag{2.1}$$

Where,

m_p, m_{Li}, m_n and m_{Be} : are the masses of p, Li, neutron and Be respectively.

T_p, T_n : are the kinetic energies of the proton and neutron respectively.

Q : the Q-value of the reaction

θ : the angle of the outgoing product (neutron) with respect to the direction of the incident particle.

Treating the equation as quadratic in $T_1^{1/2}$ and solving for T_p (the proton kinetic energy) when θ ranges from 0≤ θ ≤ 180° at 1° intervals and E_n from 0≤ E_n ≤ 1400keV at 1keV steps results in the the (θ, E_n) graph shown in figure 2.2. The contours in figure 2.2 provide insight into the double valued region near threshold (threshold=1.881MeV) where at any near threshold proton energy (<1.92MeV, see eqn 2.1), two neutron energies can be observed at any given/permissible angle of emission, with the angle of emission being limited to the forward direction.

The double valued energy limit being:

$$E_p^* = \frac{m_{Be}(m_{Be}+m_n-m_p)}{m_{Be}(m_{Be}+m_n-m_p)-m_p m_n} E_{th}$$

$$= 1.92MeV \qquad (2.2)$$

Not only do protons striking the target yield neutrons at the incoming proton energy, as protons slow down in the target, provided their energy is greater than threshold, they can also undergo the (p,n) nuclear reaction with a probability related to the cross section, σ(E_p), of the interaction.

Thus, a spectrum of neutron energies is observed at any given scattering angle and any transport calculations do indeed require a quite detailed neutron energy and spatial distribution histograms to properly predict realistic physical outcomes of computational experiments.

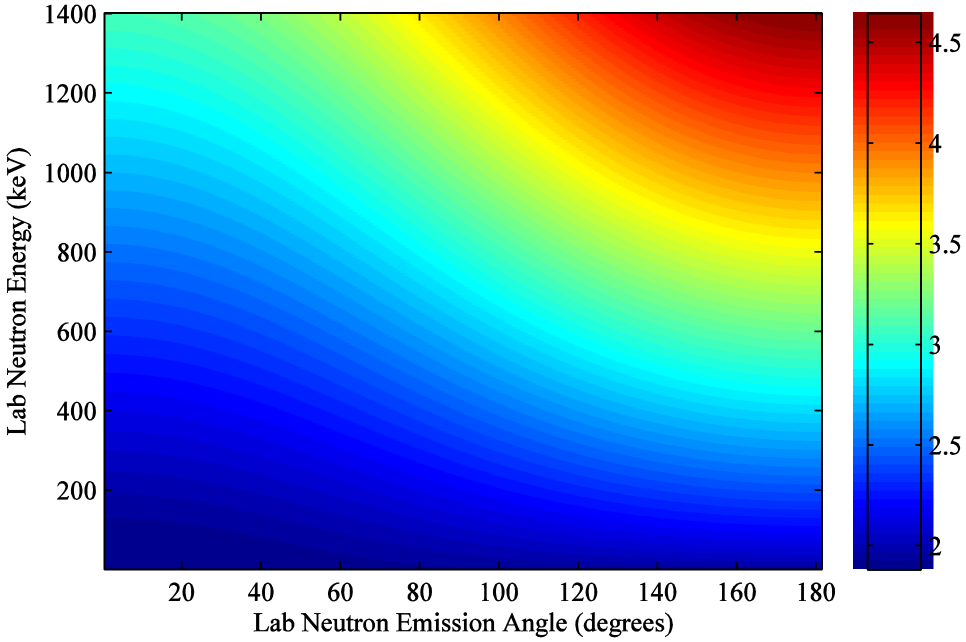

Figure 2.1 Kinematics of the Li(p,n)Be reaction from threshold to ~4.6MeV. [NB Colour bar shows incident proton energy.]

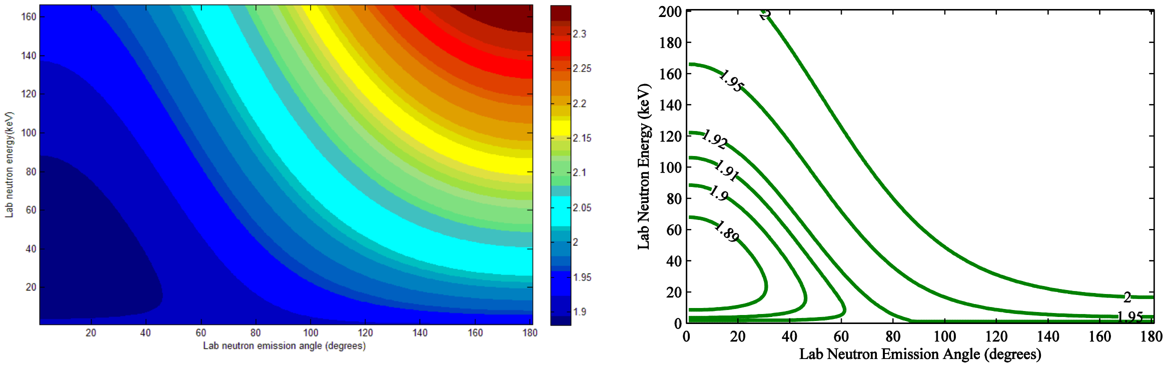

Figure 2.2 Near threshold kinematics for the Li(p,n)Be reaction with the double valued region clearly visible.

2.3 Near Threshold kinematics [Lee's Method]

In order to derive the energy and spatial neutron distribution as required by the radiation transport code MCNPX it was thought appropriate to follow the well known and established methodology of Lee and Xou [4]. In which a detailed method is discussed to overcome near threshold infinities in the Jacobians used to calculate thick target neutron yields in the energy regime below 1.95MeV. The method employs a work around that takes the product of Jacobians that are well behaved and do not result in anomalous regions in (θ, E_n) space.

Liskien and Paulsen have gathered detailed 'recommended' cross section data above 1.95MeV in the form of Legendre polynomials but don't attempt to provide any such data near threshold. Lee suggests a theoretical analytic function which he uses to interpolate reaction cross sections near threshold and is in good agreement with available experimental data.

The data provided by Liskien and Paulsen in the form of Legendre polynomials (eqn 2.3) is rather sparse and given in the centre of mass frame. To establish a reasonable degree of certainty in interpolating these values a cubic spline interpolant function was used in Matlab to interpolate values after having recalculated them in the lab frame (adopted in the rest of the calculation). The Matlab 'interp2' function interpolates between the 2-d polynomial function expanded from the Legendre coefficients, to find values of the intermediate points required on the (θ, E_n) grid space.

$$\frac{d\sigma_{pn}}{d\Omega'}(\theta') = \frac{d\sigma_{pn}}{d\Omega'}\left(0^0\right)\sum_{i=0}^{3} A_i\left(E_p\right)p_i(\cos\theta'). \tag{2.3}$$

Where,

$\frac{d\sigma_{pn}}{d\Omega'}(\theta')$ is the cross section as a function of the centre of mass angle,

A_i are the coefficients of the Legendre polynomials,

$p_i(\cos\theta')$ the Legendre polynomials as a function of centre of mass scattering angle.

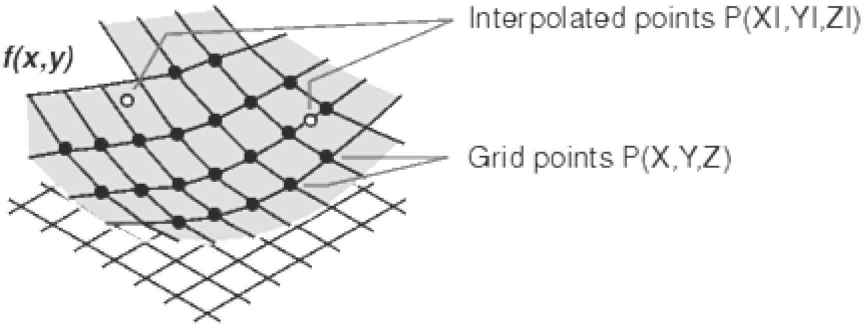

Figure 2.3 Interpolating data between 2-D grid points.

Interpolation using the Matlab built in function ‘interp2’ and using the cubic spline interpolation method, ‘looks up the elements of XI in X, YI in Y, and, based upon their location, returns values ZI interpolated within the elements of Z’ [35], as can bee seen in figure 2.3.

A considerable difference is seen when using linear interpolating functions as opposed to cubic spline interpolating functions, where linear functions calculate spectra having large plateau regions as opposed to smooth and continuous curves.

Extensive work has been done to implement Lee’s method in computational form, whereby neutron energy spectra and angular distributions can be readily calculated for any given proton energy.

Lee’s approach can be summarized in two succinct equations; one relating to near threshold double differential cross section calculations requiring an analytical form for the cross section (eqn. 2.4) and another equation beyond threshold (>1.95MeV) which uses the tabulated Legendre polynomials of recommended cross sections (eqn. 2.5).

$$\frac{d\sigma_{pn}}{d\Omega'}\frac{d\Omega'}{d\Omega}\frac{dE_p}{dE_n}=\frac{\pm\left(m_{Be}+m_n\right)^2\left(\cos\theta\pm\xi\right)\gamma E_p}{m_p m_n E_p\xi(\cos\theta\pm\xi)\pm m_{Be}(m_{Be}+m_n-m_p)E_{th}}\frac{d\sigma_{pn}}{d\Omega'} \tag{2.4}$$

$$\frac{d\sigma_{pn}}{d\Omega'}\frac{d\Omega'}{d\Omega}\frac{dE_p}{dE_n}=\frac{\pm AC_0\left(m_{Be}+m_n\right)^2\left(\cos\theta\pm\xi\right)\sqrt{m_p m_n / m_{Be}(m_{Be}+m_n-m_p)}}{(1+x)^2[m_p m_n E_p\xi(\cos\theta\pm\xi)\pm m_{Be}(m_{Be}+m_n-m_p)E_{th}]} \tag{2.5}$$

Where:

$$\xi^2=1/\gamma^2-\sin^2\theta \tag{2.6}$$

$$\gamma=\sqrt{\frac{m_p m_n}{m_{Be}(m_{Be}+m_n-m_p)}\left(\frac{E_p}{E_p-E_{th}}\right)} \tag{2.7}$$

Formulas 2.4 and 2.5 are evaluated over the relevant grid points and then divided by the mass stopping powers obtained from the transport code SRIM [5], the result multiplied by the constant, $\frac{f_{7li}N_0}{eA_{eff}}$, leading to the double differential Yield in (θ, E_n) space (eqn. 2.8).

$$\frac{d^2Y}{d\Omega dE_n}(\theta,E_n)=\frac{f_{7li}N_0}{eA_{eff}}\frac{(d\sigma_{pn}/d\Omega')(d\Omega/d\Omega)(dE_p/dE_n)}{(-dE_p/dx)} \tag{2.8}$$

Where,

f_{7li}:	Li-7 atomic fraction in natural lithium metal
N_0:	Avogadro's number
e:	electronic charge
A_{eff} :	atomic weight of natural lithium metal

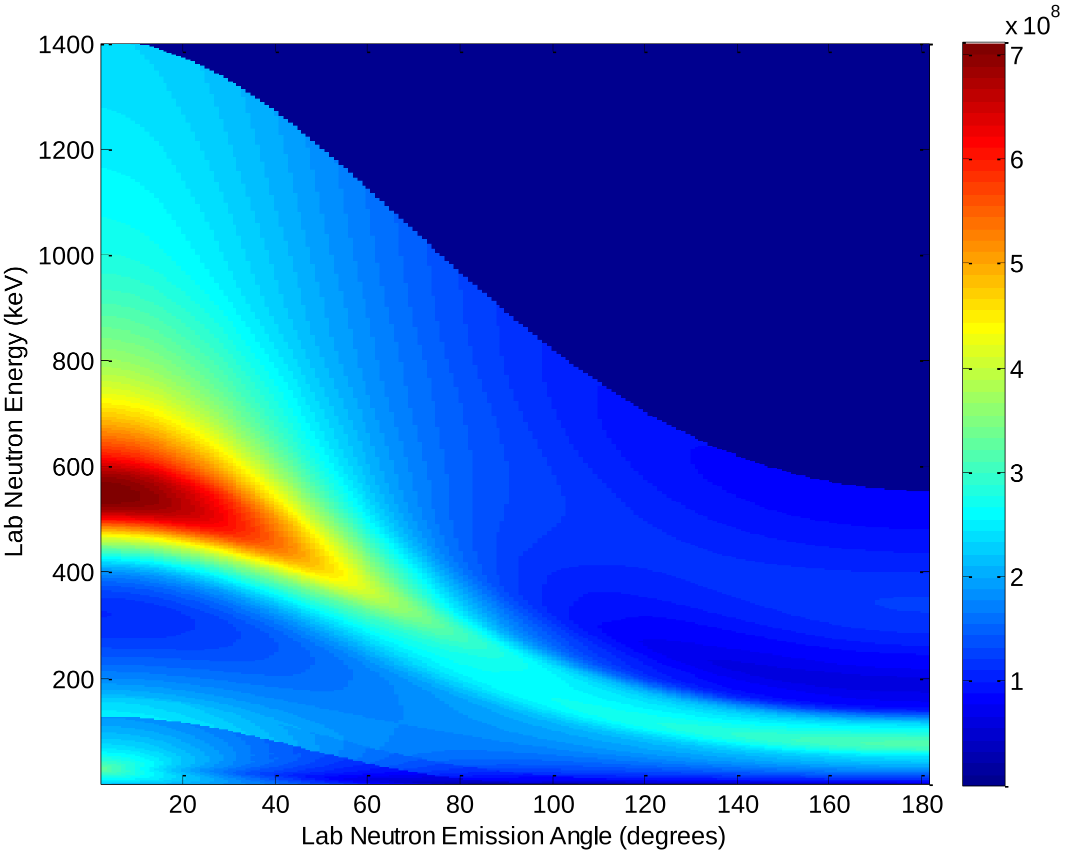

Figure 2.4 Differential Yield (neutrons / Sr keV mC) as a function of lab neutron energy and emission angle using Lee's method.

As can be seen from the above differential yield plot (figure 2.4), there exists in the interval between 1.925MeV and 1.95 MeV proton energy (below 200keV neutron energy), a region which falls beyond the 'known' theoretical resonance bound and the region where extensive and recommended experimental data (fitted to Legendre polynomials) from Liskien and Paulsen lies. Following the approach of Lee and others this region has been interpolated in a best fit manner with a smoothing spline.

2.4 Comparison of the existing source definition and that calculated with Lee's method

The neutron yield as a function of lab angle of emission is shown in figure 2.5. The existing MCNPX source definition [2] and that calculated by Lee's method show extremely good agreement bearing in mind that the newly employed Lee's method, does not yet have the small additional yield component from the excited state reaction of Be* [i.e. Li(p,n)Be*] and the energy binning structure used in Matlab is (as of yet) still a little coarse, whereby no interpolation is made between grid points in (θ, E_n) space, so that when integrating up to a given proton energy (e.g 2.8MeV) the nearest grid value has been taken as the end point.

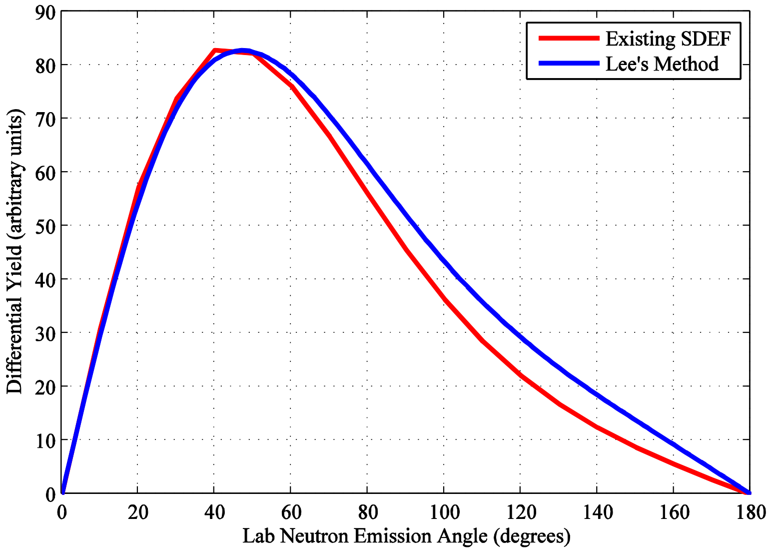

Figure 2.5. Comparison of the existing 2.8MeV source definition and calculated thick target neutron angular yield from natural Lithium metal, normalized to the peak differential yield.

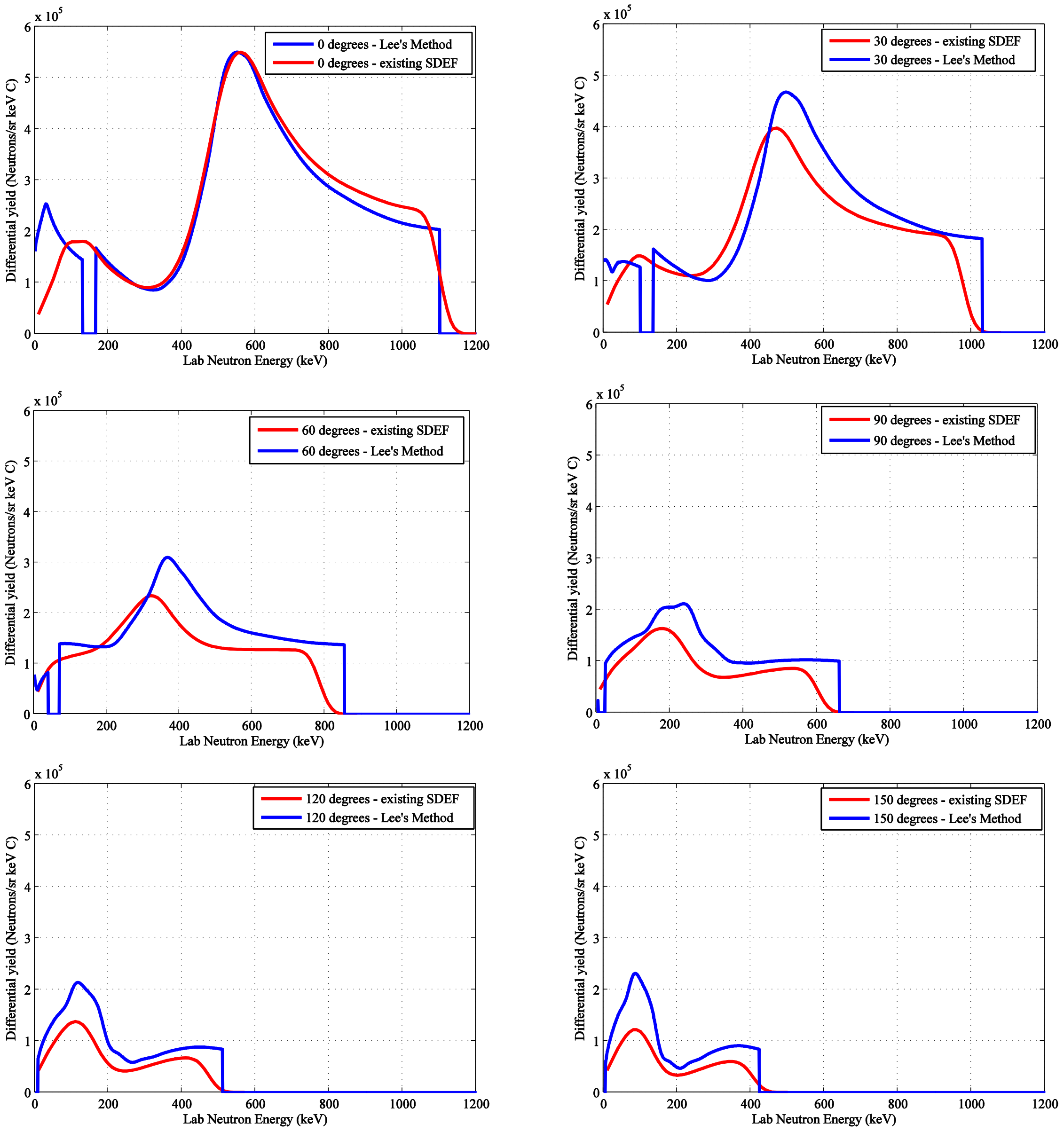

Figure 2.6 Comparison of the existing 2.8MeV source definition and calculated thick target neutron yields by Lee's method at various scattering angles, with only the 0 degree yield being normalized at the peak.

To investigate the subtle differences seen in the two source definition models, a detailed MCNPX simulation was carried out of the neutrons leaving the Lithium target, modelled as one of the two distributions shown in figures 2.5 & 2.6. The simulations included the whole beam shaping assembly and were run in neutron and photon mode. Track length estimates of flux were recorded in a simulated large water tank at the beam exit port from which photon and neutron doses were calculated at various depths. Despite the differences between the angular distribution of the differential yield of Allen & Beynon and Lee, the Monte Carlo simulations show no difference in doses recorded in the water tank to within the statistical uncertainties of the tally.

This is most likely due to the large number of interactions the average neutrons see in reaching the phantom by which time the neutron beam is very diffuse and highly scattered. Thus by the time the particles reach the beam exit port any subtle differences in energy and angular distribution between the two models are lost, bearing in mind that both models share a common neutron yield of 1.37×10^{12} n/s.

2.5 Beam Shaping Assembly (BSA); Materials and Cross sections

2.5.1 The Birmingham Facility

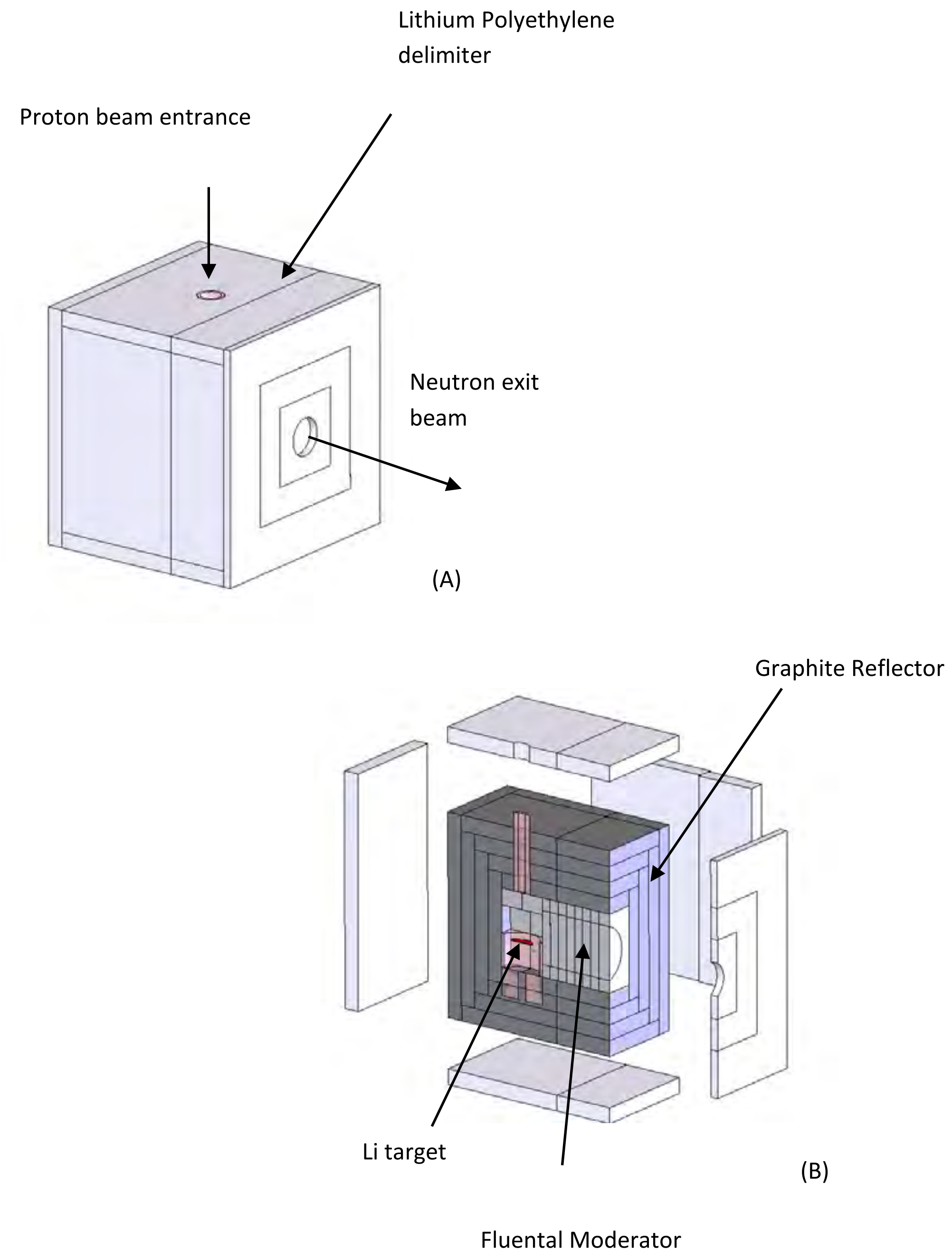

Figure 2.7 BNCT treatment facility with (A) proton beam entrance and neutron exit apertures shown. (B) Cross-sectional view showing target, moderator and reflector assembly.

Figure 2.7 shows the current Birmingham facility with Fluental^{TM} moderator and graphite reflector materials. Fluental^{TM} is a patented composite, which has been used for many years in the Finnish, reactor based, clinical BNCT facility as a moderator material. It comprises of 69% AlF, 30% Al, and 1% LiF. It has relatively high inelastic scattering cross-sections for its first and second excited states (above 100keV). These high cross-sections are efficient in losing large amounts of energy, thus having the ability to rapidly moderate the beam to less than 100keV.

Below 100keV elastic scattering dominates, and it then becomes important for the moderating material not to cause the lower energy neutrons to lose too much energy in any single collision, nor to retain too much energy. The former causing neutrons energies to fall below those required and the latter requiring greater lengths of moderator.

As we have a broad spectrum of neutron energies from our accelerator driven charge stripping reaction, the material of choice has to posses a combination of properties, they being:

- High inelastic scattering cross section between our maximum neutron energy (1.2MeV) down to the elastic scattering energies (~100keV)

- High elastic scattering cross sections down to epithermal energies

- Low epithermal and low fast neutron absorption cross sections.

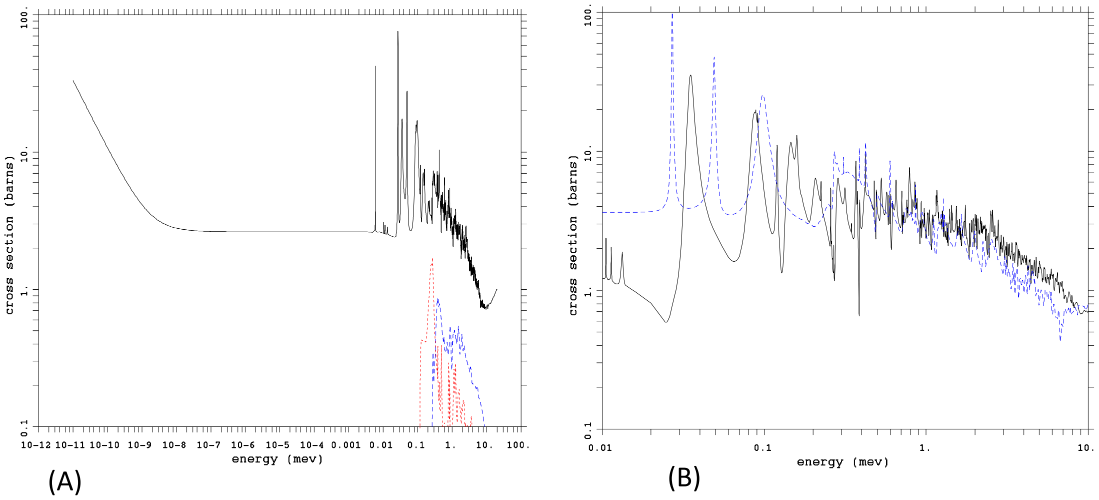

Figure 2.8 Elastic scattering cross sections of (A) Fluental along with its first and second (n,n') excited states (B) Aluminium (solid line) and Fluorine (dashed line). [x-axis units are in MeV – incorrectly plotted by MCNPX/mcplot]

Fluental exhibits such properties, the Aluminium content having useful first and second excited states to inelastically scatter neutrons from energies above 843.8keV (figure 2.8), with high elastic scattering cross section down to ~30keV.

The problem arising with the choice of pure Aluminium, or any other suitable element, as a moderator is that the neutron energies tend to gather in the valleys between resonances i.e. being too high energy to be scattered by lower energy cross-sections and too low energy to be scattered by high energy cross sections. The advantage of then combining materials to have complementary cross sections, the combination of which fills in the gaps in the resonances of the other, see figure 2.8 (B) which illustrates the complimentary cross sections of Al and Fl. This becomes particularly relevant for Fluental above 27keV see figure 2.8(B).

Fluental also contains 1% LiF added to absorb thermal neutrons which provide no useful dose to the tumour tissue but just adds to the skin dose (if they reach the patient). ^{6}Li has a high thermal neutron capture cross section (see fig. 2.10). This not only serves to reduce the thermal neutron contamination but also reduces the gamma contamination which is caused by thermal neutron capture by ^{27}Al to produce $^{27}\text{Al}(n,\gamma)^{28}\text{Al}$, with gamma rays of 7.73MeV. The ^{28}Al decays with a half-life of 2.24 minutes producing further 1.799MeV Gamma rays.

The thermal neutron capture in Li does not produce the same unwanted gamma effect as in Al. The neutron capture results in $^{6}\text{Li}(n,\alpha)^{3}\text{H}$, the products of the reaction being alpha particles and tritium, which are not as penetrating as photons hence requiring relatively little shielding.

2.6 An Improved Beam Shaping Assembly

Extensive re-modelling work has been carried out using the Monte Carlo transport code MCNPX. Results of simulations were presented in the form of a poster at ICNCT 13, [Appendix B]. A brief outline and summary of which follows.

The current Birmingham facility has a 25.1cm FLUENTAL™ moderator between the target and beam exit port, which provides an extremely good beam profile in phantom. The aims of this study were to compare the merits of FLUENTAL™ to MgF_2 and Teflon moderators, and to assess the effects of Graphite and Lead reflectors on designing and building an optimal facility.

Published findings indicate that MgF_2 might serve as a better moderating material in accelerator driven systems over other materials more commonly used [6]. Various moderator and reflector materials have been assessed for their impact on improved therapeutic depth dose profiles.

The moderators, Magnesium Fluorine (MgF_2) and Teflon (CF_2), show remarkably similar complimentary cross sections to that of Fluental, (figure 2.9(A) (B)), in both elastic and inelastic scattering regions and thus are particularly efficient in inelastically scattering the higher energy neutrons produced by the Li target (see first and second excited states) where the elastic scattering regions fall sharply. Once neutrons fall to energies below ~100keV the only means of moderation is via elastic scattering. Here, the sharp rise in cross sections rapidly and efficiently moderates them to epithermal energies. One advantage of using MgF_2 over Fluental is that it has a lower neutron absorption cross section, thus retaining more neutrons of useful energy in the beam.

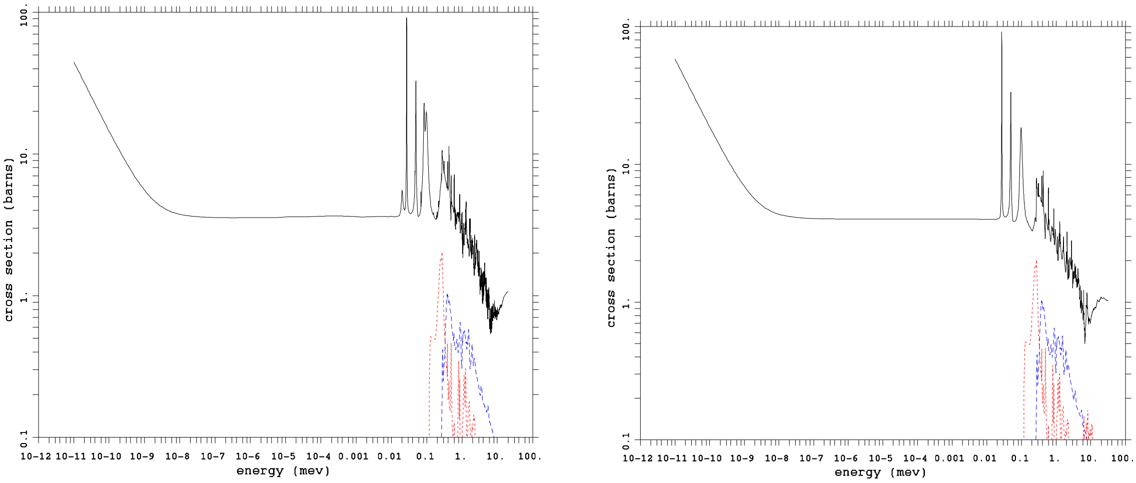

(A)

(B)

Fig. 2.9 Elastic scattering cross sections (A) MgF_2 (B) Teflon along with their first and second excited states.

The absence of any thermal neutron filtering significantly impacts on the quality of our beam which shows moderate improvement when using MgF_2 or Teflon as moderators, which we have seen, possess excellent moderating properties but lack thermal neutron absorption properties. The addition of a 5mm thick Li-Si thermal filter, composed of 5% Li to 95% Si, at the beam’s exit port significantly shifts depth dose curves in favour of an improved ‘quality’ beam, in terms of penetration, for both these materials and, surprisingly, even Fluental. Thus showing the need for a good thermal neutron filter.

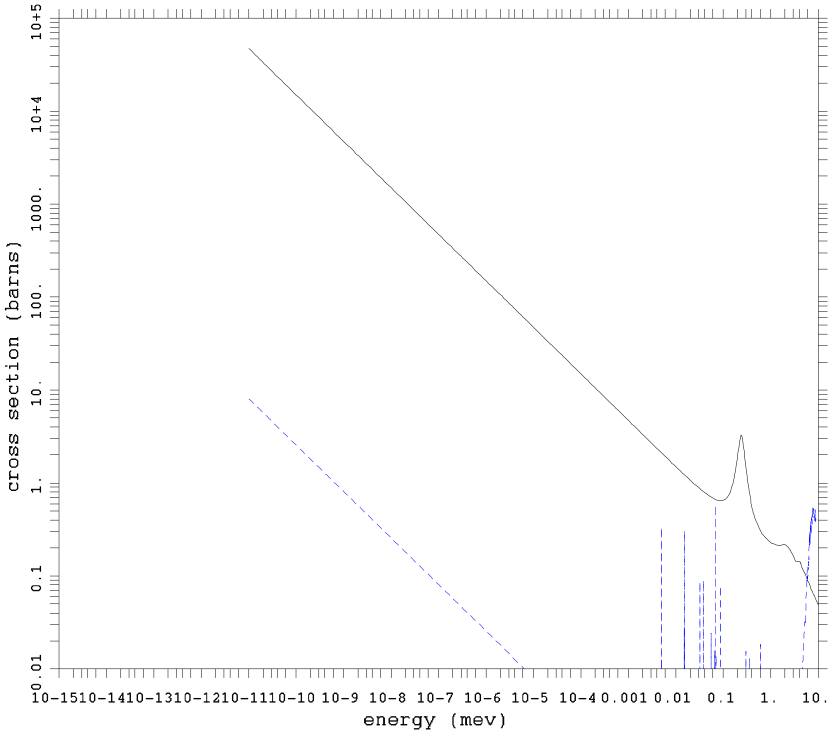

Fig. 2.10 Neutron absorption cross sections of lithium and silicon (Li=Solid line)

In terms of reflector materials, the elastic scattering cross sections of graphite (figure 2.12 (A) (B)) show high elastic scattering up to ~1MeV, which thereafter falls very sharply. It is here that it becomes advantageous for us to adopt Lead as a reflector material over graphite, as it has much higher elastic scattering cross sections than graphite at both lower and higher neutron energies (figure 2.11). Graphite remaining considerably below 10 barns and lead above 10 barns up to 1MeV. After which the lead elastic scattering cross section falls much more slowly than that of graphite.

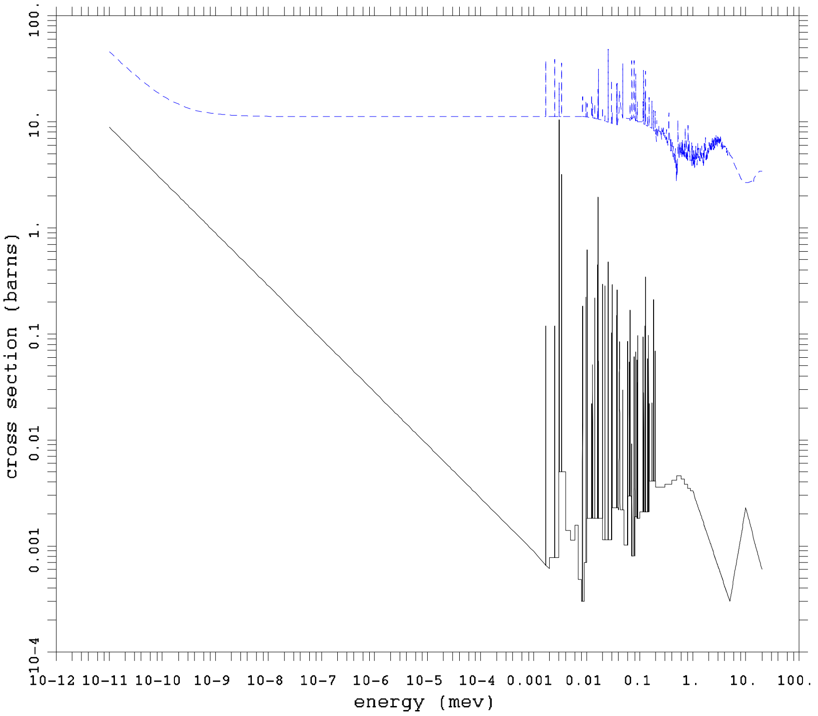

Fig. 2.11 Absorption and Elastic scattering cross sections of lead (absorption = solid line)

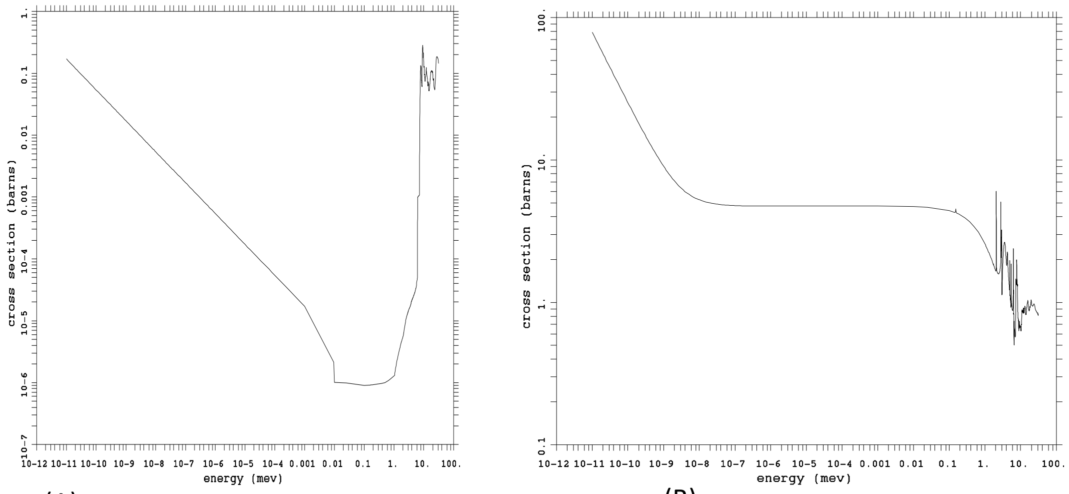

(A) (B)

Fig. 2.12 (A) Absorption (B) Elastic scattering cross sections of graphite

2.6.1 Beam Figures of Merit (FOM)

The motivation for optimising and re-modelling the treatment facility was to maximize the dose to tumour tissue while keeping the weighted dose to healthy brain tissues below 12.5 Gy. Five key indices (Figures of Merit (FOM)) were calculated for three moderator materials (Fluental, MgF_2 and Teflon) and two reflector materials (graphite and lead). The Figures of Merit being:

- Therapeutic Ratio (TR) – [defined as the weighted dose to the tumour at that depth divided by the maximum weighted dose to healthy tissue].
- Therapeutic Ratio at mid-brain (i.e. 6.5 cm),
- The peak or maximum Therapeutic Ratio
- Treatment Time (the time taken to deliver a weighted dose to healthy tissue of 12.5 Gy). [based on 1mA proton beam current]
- The Advantage Depth (AD) – the depth at which the Therapeutic Ratio falls to 1.

The FOMs of the current Birmingham facility exhibit extremely good Therapeutic Ratios and relatively low skin doses when compared to employing other BSA materials. Calculations show improvements in all Figures of Merit with 21.1 cm of MgF_2 moderator combined with a lead reflector system over the current Birmingham assembly [Appendix B].

It is evident from the calculated TRs that deeper seated tumours are better treated with the short Post Moderator Reflector (PMR) at the beam exit port. The mid-brain TR increases by a considerable 11% advantage over the filtered MgF_2 assembly without PMR and 39% over the existing facility. Treatment times are severely impacted with increased PMR length as well as mid-brain TRs.

If a facility were to be designed for the treatment of ONLY shallow tumours, the TR at 6.5 cm and the AD are not as important a factor as the Max TR. Which shows very little improvement with the addition of the filter and post moderator reflector (PMR).

Changing the graphite reflector to one made of lead (for 25 cm Fluental moderator) delivered a substantial improvement. It resulted in an increase in beam quality in terms of Therapeutic Ratio and AD. The AD increased from 9.1 to 9.8 ±0.1cm, the TR at 6.5 cm deep from 2.23 to 2.75 and the max TR from 5.34±0.05 to 5.40±0.05, with a 10 % reduction in treatment time from 198 minutes to 176 minutes.

In order to increase the dose rates obtained with the MgF_2 moderator / lead reflector, and thus reduce the treatment time, it becomes necessary to compromise beam quality. By moving to a shorter moderator depth of 18.1 cm treatment time was brought down from 198 minutes to 146 minutes. The change in other key indices being AD from 9.1±0.1 to >10cm, the TR from 2.23 to 2.76 and the max TR from 5.34 ±0.05 to 5.26 ±0.03 when compared to the current facility.

2.6.2 Conclusion

Various compositions of beam shaping assembly have been considered for optimal dose delivery. Competing merits make it difficult to single out any one design as being optimal, especially when costs and practicality of construction are factored in. The MgF_2 / lead assembly has a small advantage over the existing Birmingham facility (max TR has less than a 2% advantage) and shorter treatment time, but exhibits a higher skin dose. In light of this study it is evident that replacing the current graphite reflector with one made of lead and to add an optional lithium filter to treat deeper seated tumours is the optimal way forward for the Birmingham facility.

Chapter 3

Beam Monitoring and Calibration

3.1.1 Beam Monitors

The University of Birmingham's experimental NCT facility is based on a 3MV Dynamitron particle accelerator, which is used to accelerate and bombard a high current of protons of anything up to one milliamp onto a thick natural lithium target to generate neutrons [7]. Various beam monitors are used to monitor beam stability, gauge dose delivery, and to help in beam characterisation and calibration. A Keithley electrometer is used to measure the integrated proton current delivered onto the target, a Geiger counter to monitor the gamma ray field passing the beam aperture, and two fission chambers, a primary and a secondary, to monitor the thermal neutron flux near the beam exit port.

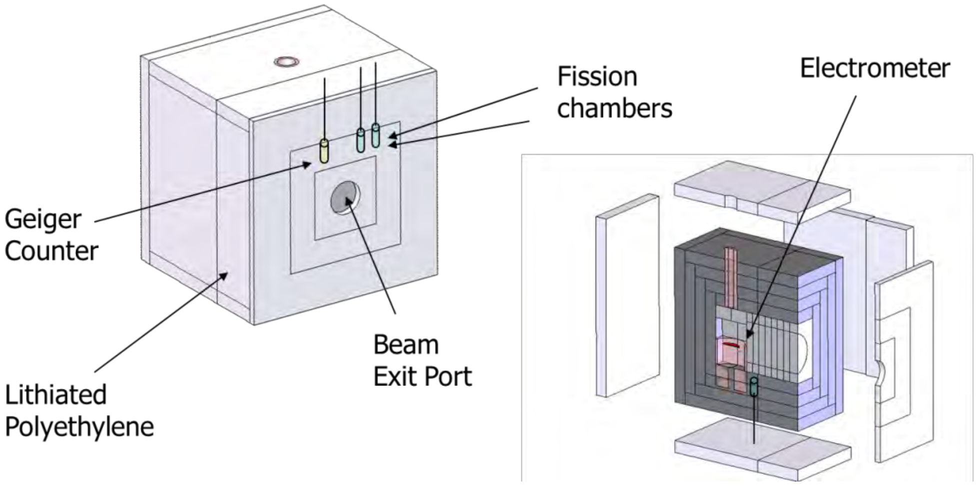

Figure 3.1 - showing the location of beam monitors relative to the Facility's Beam Shaping Assembly.

Computational and experimental work has been carried out at the treatment facility to relocate two neutron monitor chambers (^{235}U fission chambers - Centronic Ltd., FC05A/500/u235). IEC requirements for monitoring radiotherapy beams require the counters to be in the 'treatment' beam. In placing the monitor chambers within the treatment beam, the problem arises of neutrons backscattering from patient or phantom affecting the counts at these detectors, which can only be practically located within the 25 mm layer of lithium polyethylene shielding surrounding the exit port of the treatment facility. The revised monitor position was chosen after detailed consideration of sensitivity to backscattered radiation and detector count-rate.

The fission chambers were originally positioned such that they were separated from the patient / phantom by 20 mm of Li-polyethylene , the chambers being located in the back of the 25 mm Li-polyethylene beam delimiter, adjacent to the graphite neutron reflector. It was found that the original chamber positions were susceptible to movement. Even though this movement might only be slight, the chambers were located close enough to a boundary between two surfaces (the graphite reflector and the Li-polyethylene delimiter) such that they could easily move into high flux regions (out of the shielding). It was decided to relocate the chambers away from the boundary into a more reliable position.

Future plans for the NCT facility include the upgrade of the ion source to yield higher proton currents in order to produce a higher neutron flux at the beam exit port. This could cause unacceptable dead time losses in the fission chambers. A further aim of the relocation of the fission chambers is to reduce the count rate seen by the chambers by a factor greater than 2.

The simulations also aimed at maintaining the neutronic coupling levels to less than or equal to 5%. The coupling being the effect of 'multiple' back-scattered neutrons from patient /

phantom positioned at the beam exit port, which cause the chambers to record higher count rates than those recorded for a free beam.

Thus the goals were to locate the chambers such that:

- the chamber positions are stable
- the count rate is reduced to less than half its current rate (i.e to ~approx 4000 cps at 1 mA proton current)
- the neutronic Coupling Ratios are maintained below 5%

3.1.2 Fission chamber Modelling & Simulation

To investigate these requirements, detailed Monte Carlo simulations were carried out to quantify the degree of neutronic coupling using the radiation transport code MCNPX 2.6. Mesh tallies, employing voxelised track length estimators of flux, were used over the entirety of the shielding /delimiter surrounding the beam exit port. The simulation consisted of the entire beam shaping assembly, heavy water cooling system and outer shielding with a 12cm diameter beam exit aperture, as shown in figure 3.1.

Simulations were carried out in full electron, photon and neutron physics modes. ENDF/B-VII, continuous energy nuclear and atomic data was used, along with LA150U photo-nuclear data libraries. Thermal (S(alpha, Beta)) treatment was envoked for the graphite reflector, water (in the phantom), the polyethylene phantom and the Li-polyethylene delimeter.

The Centronic pulse fission chambers used in the facility (FC05A/500/U235) are coated with 500 μgcm^{-2} of UO_2, have an active length of 0.2″ (5.1 mm), an outside diameter 0.25″ (6.4

mm) and a neutron sensitivity of 2.1e-4cps/nv. The incoming neutrons cause fission in the UO_2 to yield high energy fission fragments which cause ionisation in the active detector volume resulting in measureable pulses from the chamber. The rate of pulse output is proportional to the rate of fission reactions and consequently to the neutron flux. [see schematic diagram fig 3.2]

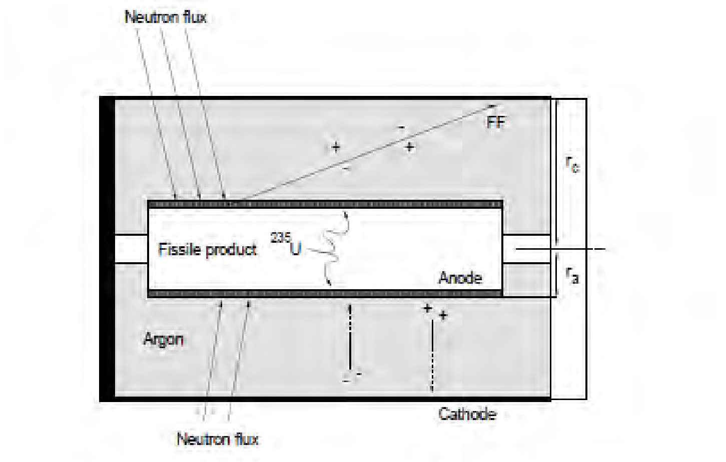

Figure 3.2 A schematic diagram of a fission chamber [37].

The neutron spectrum at the beam exit port is shaped to have its maximum intensity in the epithermal region and thus there is a need to model the chamber sensitivity to a spectrum of neutron energies when simulating any possible response to the movement and repositioning of these chambers. This is readily done by multiplying the eventwise calculated track length estimate of neutron fluence with the ^{235}U total fission cross-section (i.e. the active detector material) This is done in MCNPX using the tally multiplier card to obtain a reaction rate in the chambers at any given position relative to their old reference position. Thus the MCNPX mesh tally was used to divide the 25 mm lithium polyethylene layer into small voxels of 1 cm x 1 cm x 0.5 cm. Transport calculations were optimised by using weight windows and tallies were resolved to better than 1% statistical uncertainty.

3.1.3 Neutronic Coupling

The neutronic Coupling Ratio (CR) was used as a measure of increase in neutron flux due to the presence of phantom / patient at the beam exit port and can be defined as:

$$CR = \frac{\text{Counts in chamber with phantom}}{\text{Counts in chamber without phantom}} \tag{3.1}$$

Simulations were carried out with and without the presence of a standard large water tank phantom (40 x 40 x 20 cm^3), external to the beam shaping assembly and abutting the beam exit port each voxel thus recording a measure of the count rate as seen by a typical fission chamber.

Results of simulations are presented as variations along a vertical line through the centre of the beam exit port. Separate data sets refer to the position within the 25 mm of Li-polyethylene. Figure 3.3 shows the count rate without the phantom and Figure 3.4 shows the count rate with the large water phantom. In Figure 3.3 the greatest detector count rates are seen at positions closer to the neutron source, while in Figure 3.4 the count rates are greatly increased in the open beam port due to backscatter from the phantom.

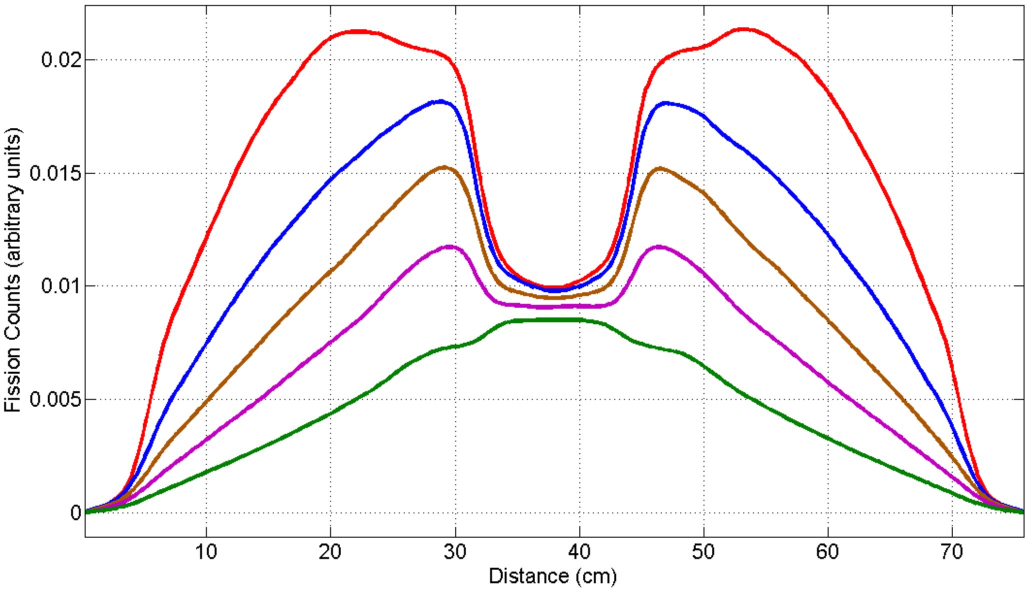

Figure 3.3 - Fission counts as a function of vertical position (from top of BSA) in each of the five layers of delimiter, in the absence of any phantom [Green curves being the outermost layer, red curve being the innermost].

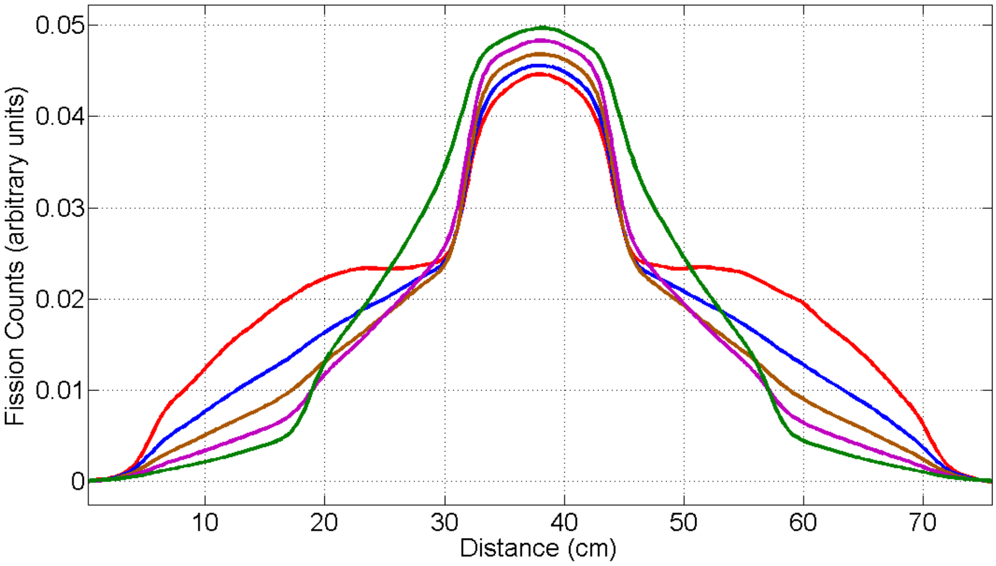

Figure 3.4 - Fission counts as a function of vertical position (from top of BSA) in each of the five layers of delimeter, with large water phantom at the beam exit port. [Green curves being the outermost layer, red curve being the innermost].

The requirement to reduce count rate in the monitor chambers suggests that the middle position in the Li-polyethylene delimiter would solve this need.

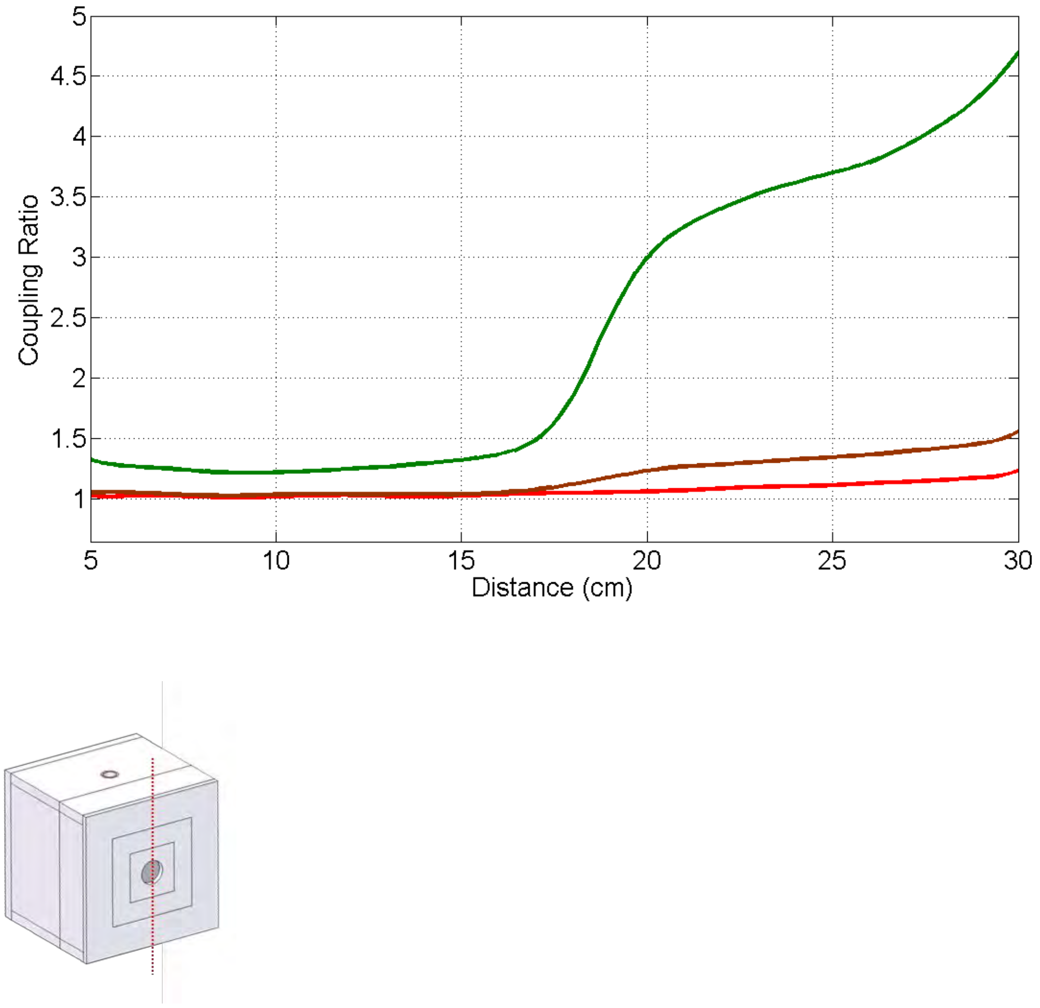

Figure 3.5 Coupling Ratio as function of Depth (from top of BSA) in three layers of delimiter (middle and two extremes). [Green curves being the outermost layer, red curve being the innermost].

Figure 3.5 shows coupling ratios (with and without the large water phantom), it can be seen that the high degree of coupling very closely matches the size of the large water phantom (40cm x 40cm x 20cm^3), as is clearly illustrated in the surface mesh plots of coupling calculated from MCNPX in figure 3.6 and 3.7. It also falls rapidly with distance in shielding both at the front surface and around the beam port. A reference fission chamber used to sit ~15cm from the top of the Li-polyethylene delimeter, where there was very little measured neutronic coupling (~1.02) and were it to be repositioned in the centre of the Li-polyethylene, simulations show it would still be of the same order as the very back of the delimeter.

The coupling ratios for a restricted set of positions where monitor chambers could feasibly be located can be seen in Figure 3.5. Three data sets are shown corresponding to the inner, middle and outer layers of the Li-polyethylene delimiter. As the fission chamber position is moved from the top of the BSA towards the aperture the degree of coupling is greatly increased as these are the points which are closest to where the LWT meets the delimeter surface, moving even further down and into the aperture region, which is an air filled void, further pushes up the degree of coupling seen as there is no longer any shielding and neutrons can undergo multiple scattering events and traverse the detector location many more times (in the absence of Li-polyethylene).

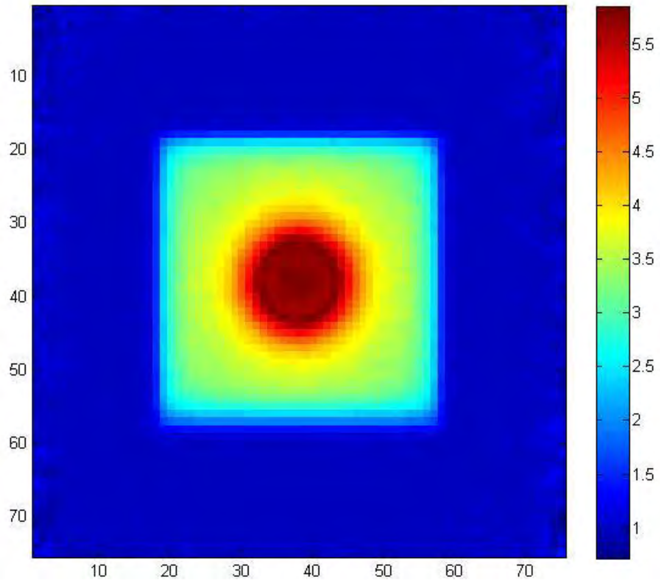

Figure 3.6 Coupling ratios in the outer surface voxels of the Li-polyethylene delimiter.

Figure 3.7 and 3.8 show the neutron fluence (un-normalised) within various layers (of 0.5cm) in the shielding both in profile and in cross section, Coupling again can be seen, being significant at the outer layers extending to ~20cm from centre, i.e. ~17.5 cm from the edge. Relocating the Monitor chambers to the centre clearly shows the large reduction in fluence with respect to the inside surface.

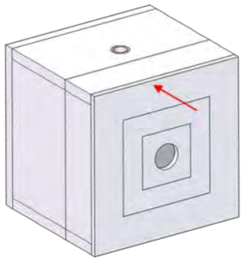

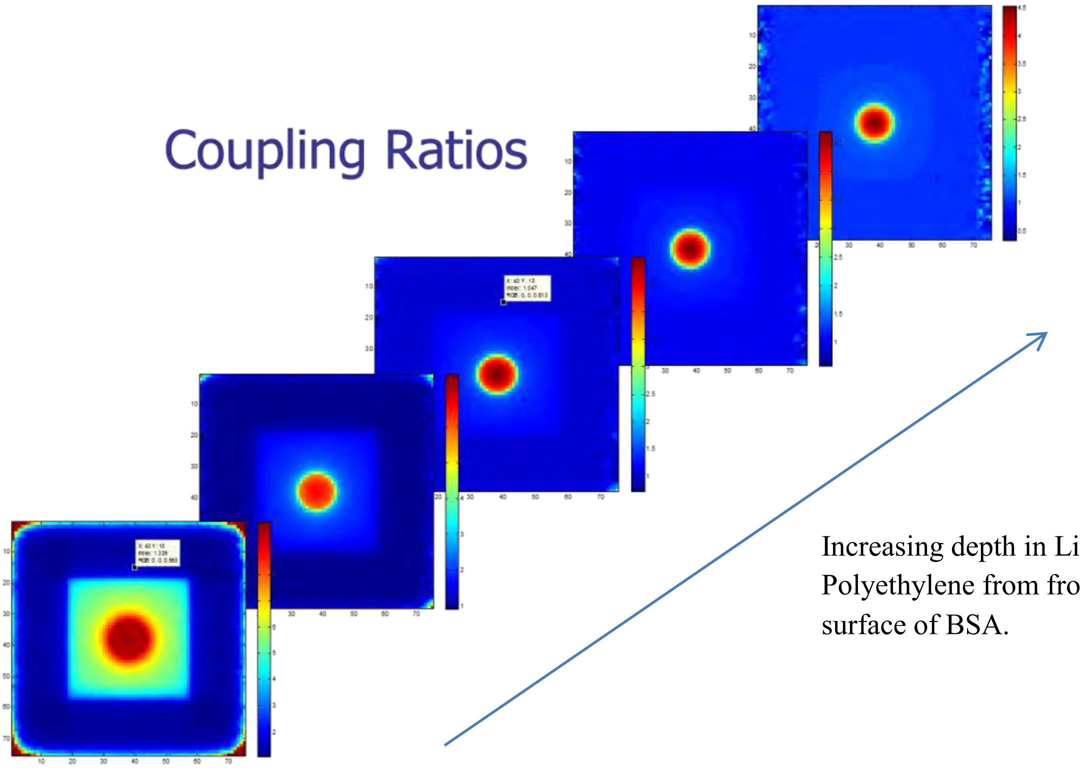

Coupling Ratios

Increasing depth in Li-Polyethylene from front surface of BSA.

Figure 3.7 Coupling ratios as a function of depth throughout the Li-polyethylene delimeter.

The requirement for CR of less than 5% (1.05 on Figure 3.5) suggests that the chamber be located no closer to the phantom than the centre of the delimiter and no further from the top of the BSA than 15cm.

3.1.4 Experimental validation

The original monitor chamber position was separated from the patient / phantom by 20 mm of Li-polyethylene, as chambers were located in the back of the 25 mm Li-polyethylene beam delimiter, adjacent to the graphite neutron reflector. Experimental coupling with the chambers in this position was measured to be 2.3 ± 0.2% in the presence and absence of the LWT, and the corresponding MCNP simulated prediction being 2.6 ± 1%.

Changing the monitor position to be centered within the Li-polyethylene delimiter, separated from the patient / phantom by 12 mm Li-polyethylene (instead of 20 mm) was predicted by MCNP to reduce the count-rate by a factor of 2.5 ± 0.1. This was verified experimentally to be a factor of 2.4 ± 0.1, producing typical detector count-rates at 1 mA proton current of approximately 4000 cps. This change of position was predicted to increase the phantom coupling to 3.9%, which has been verified experimentally to be less than 4%.

Note that this coupling is anticipated to be negligible (<1%) for other smaller phantoms and for actual patients, but experimental validation was sought with the largest phantom which provides the greatest degree of coupling.

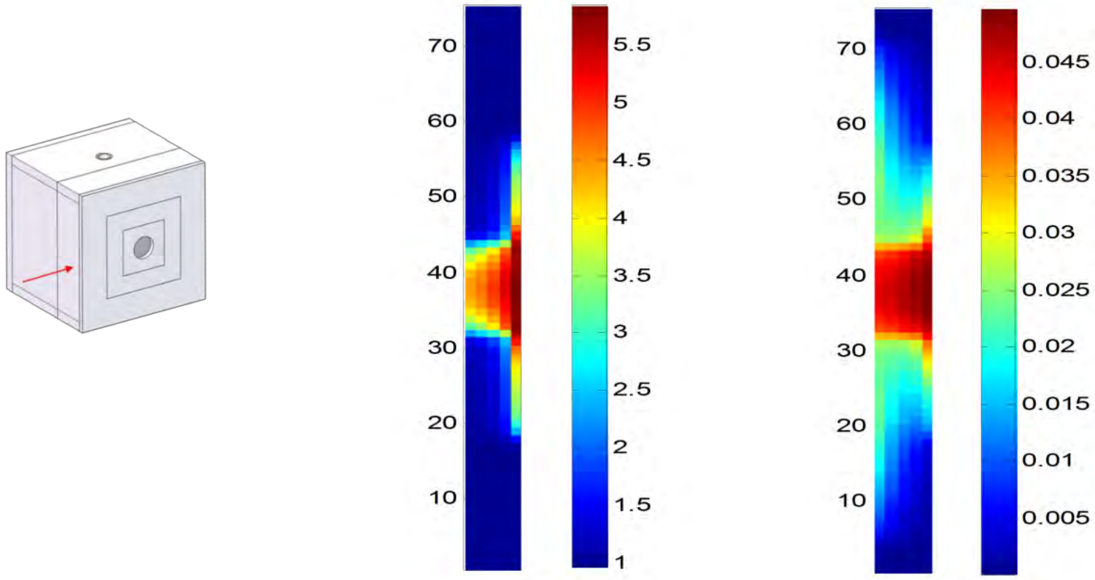

Figure 3.8 Simulated Coupling Ratio (left) and fission counts (right) as function of Depth (from top of BSA) in the five layers of delimiter.

3.2 Beam Calibration

‘The nominal machine output voltage is determined during standard operation by the voltage drop across 10 GΩ resistor exposed to the accelerating potential, as read on a 1.5 kΩ shunt resistor by a digital volt-meter (DVM). Procedure for setting a given machine voltage requires the operators to increase the voltage of the transmitted 130 kHz R.F. signal until the DVM reading matches the reading predicted from previous calibration.’ [41]

Aluminium targets are commonly used for calibrating low energy accelerator beams. The singular stable isotope of the metal, aluminium-27, has 22 low energy (p, γ) resonances, some of which are used as threshold energy calibration points. Specific well resolved single resonances, with very narrow resonance widths, can also serve to gauge the energy resolution of the incoming proton beam.

The need for a 2.8MeV proton beam requires that the Dynamitron accelerator be accurately calibrated and the DVM setting to be stable. The calibration is carried out using some of the aforementioned thresholds in the Al(p,γ)Si reaction as well as the Li(p,n)Be threshold reaction at 1880.6 keV. The Li(p,n)Be threshold being measured with fission counters, the Al(p,γ)Si thresholds being measured, in a modified beam line with a thick aluminium target and scintillation detector (NaI).

In order to carry out the calibration a beam line is drawn from the accelerator at the end of which is fixed an aluminium target, on the external surface is positioned a NaI detector and associated electronics. The voltage of the transmitted R.F. is gradually increased by the operator (as monitored by the DVM) and the integrated gamma ray counts in the detector gathered, as ^{13}Al(p,γ)^{14}Si resonance thresholds are crossed noticeable steps are seen in the yield data collected. Mass 2 protons are used to probe higher energy DVM calibration points as half the total energy per nucleon is imparted in the reaction, thus a 1388keV resonance can be used as calibration for a 2776keV accelerator potential using mass 2 protons.

Figure 3.9 shows the experimental ^{13}Al(p,γ)^{14}Si thresholds as measured by Deconninck and Demortier [38], the experimental data has been re-plotted against Birmingham DVM settings to aid in the search for thresholds during calibration. The overlayed blue arrows show the thresholds used for a typical full beam calibration, the red arrows being additional points suggested and used by the author for the last full beam calibration. The full experimental DVM calibration is very time consuming and thus a more regular interim measure of DVM settings carried out by searching for the 1880.6 keV Li(p,n)Be threshold can serve as a stability check on the overall behaviour and drift in the calibration voltage.

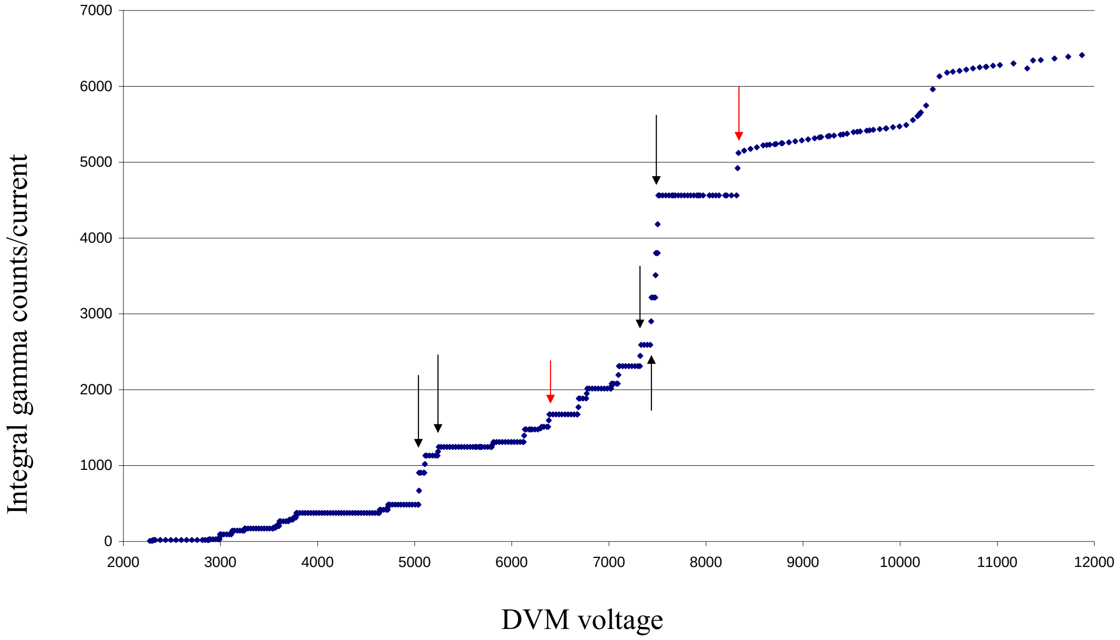

Figure 3.9 Experimental ^{13}Al(p,γ)^{14}Si thresholds as a function of (interim) DVM settings [Blue dots are the experimental data of Deconninck and Demortier [38], overlayed with arrows highlighting Birmingham calibration points].

Though prompt gamma ray production thresholds in aluminium are discrete, in a non-mono energetic beam the spread in proton energies (which resemble a Gaussian) trigger the reaction through higher energy protons (leading the Gaussian spread) and result in a sigmoidal step through each threshold. From the sigmoidal step function it is possible to deduce the spread in proton beam energies impinging on the aluminium target.

One such 'sigmoidal' step through a threshold is shown in figure 3.10, the first derivate of which shows the Gaussian like nature of the beam spread. The beam spread ~ 65DVM settings. Though this analysis is rudimentary it does show that the method could be used to calculate a more accurate spread in beam energy using the entirety of the threshold data, albeit at lower energies and currents than those normally used [the DVM calibration is typically done at a few microamps beam current and at proton energies below that at which we operate i.e. 2.8MeV].

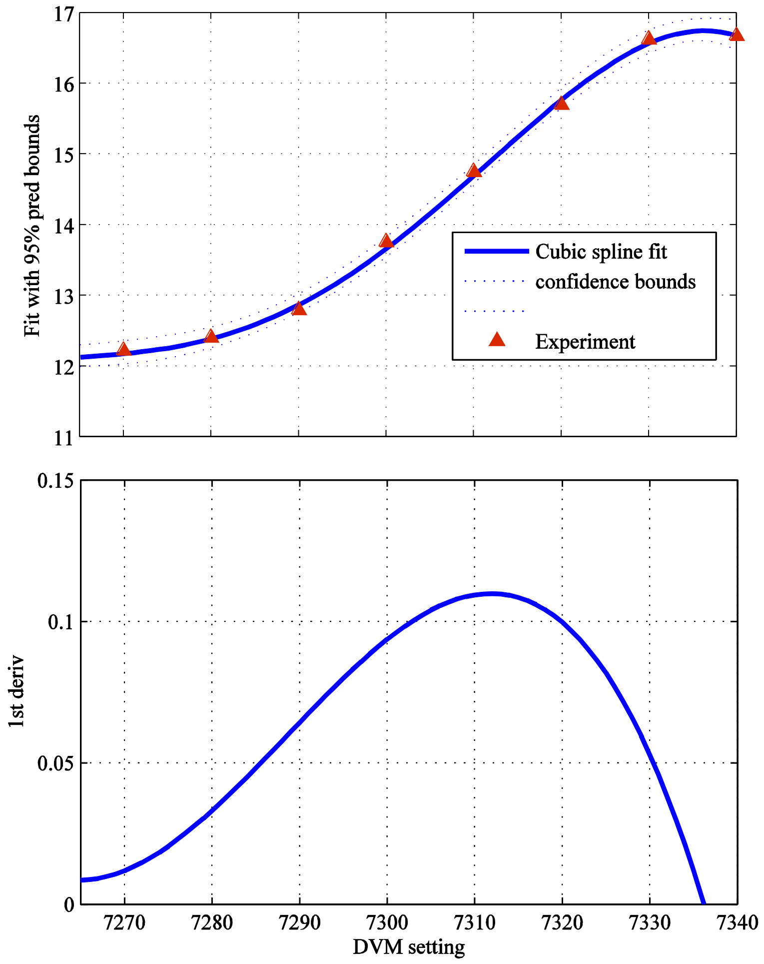

Figure 3.10 Typical threshold DVM setting vs integrated count and its first derivative.

A full beam calibration curve, using mass 1 and mass 2 protons and the lithium neutron threshold calibration point (pink square) is shown in figure 3.11. A quadratic curve is fitted from which the 2.8MeV DVM setting is calculated.

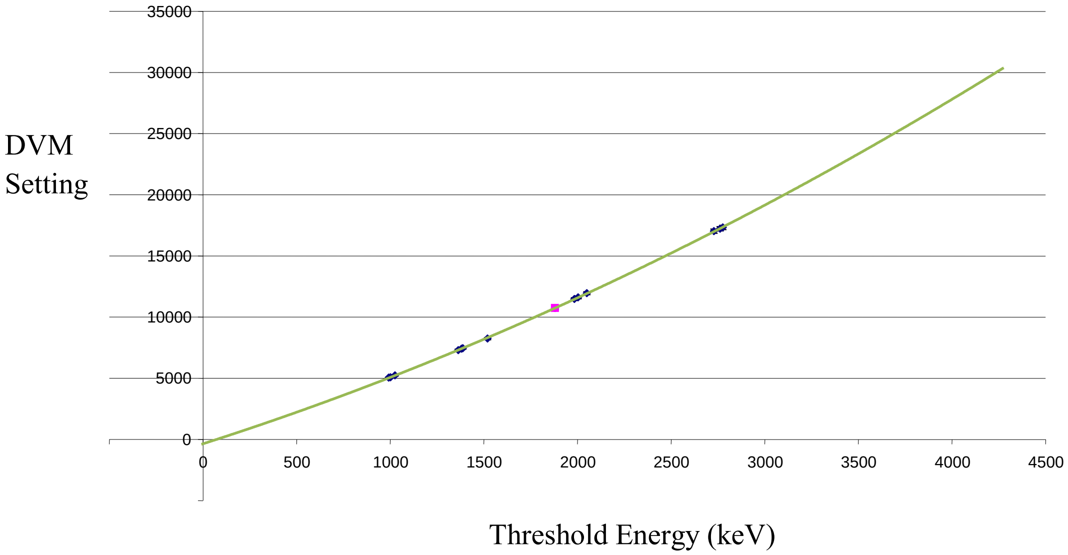

Figure 3.11 Complete DVM calibration using the 1880.6 keV Li(p,n)Be threshold (pink square) and Al(p,γ)Si thresholds (blue symbols). [6/2008]

Historic data of the voltage calibration via aluminium resonance threshold activations fitted with an established quadratic model [41] is shown in Figure 3.12. Showing clearly the changes in trend of the DVM calibration as a consequence of drift in accelerator voltage. This drift in voltage and consequently accelerated proton energy not only impacts neutron yield but also modifies the neutron spectra which is tailored for ideal performance. Left unnoticed it would create a discrepany between delivered treatment and that planned.

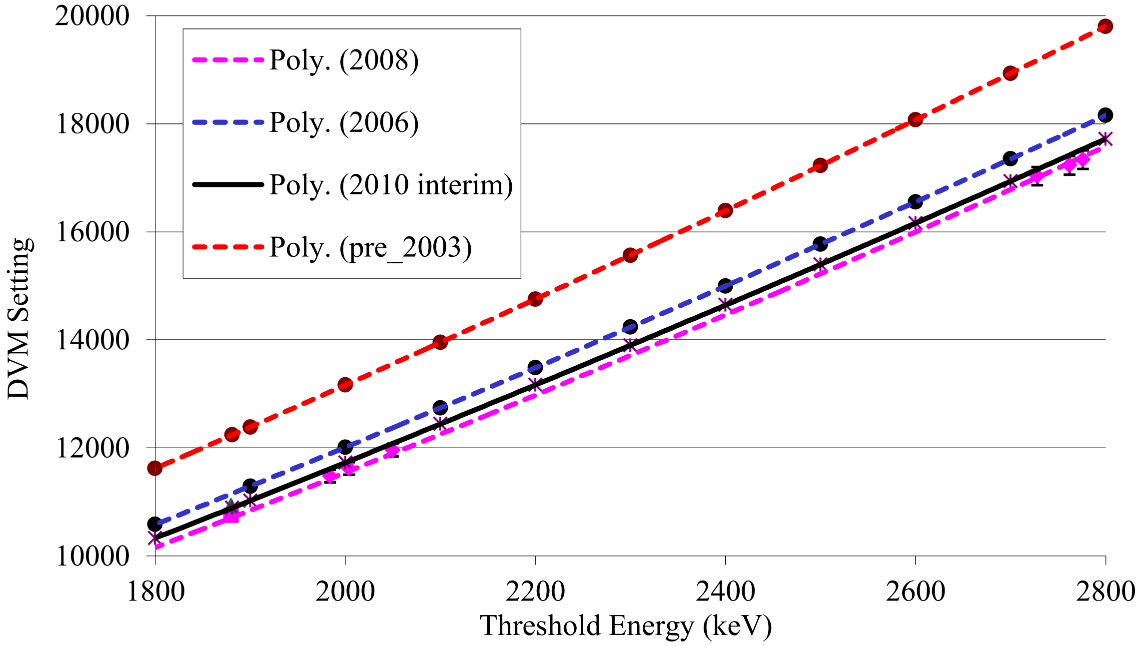

Figure 3.12 Experimental DVM calibration curve interpolated from the low energy aluminium resonance thresholds.

3.3 Yield Variations

It is extremely important to regularly check the energy calibration of the accelerator. Relatively small changes in voltage settings result in quite large changes in yield and spectra.

Figure 3.13 shows the variation in count rates recorded on the fission chambers at the beam exit port vs the average current delivered on target for a particular measurement. The measurements span from 2003 to the present day.

As can be seen the ratio of the average beam current during an irradiation and the count rate in the monitor chambers, follows four distinct groupings. The lower yield line being the relocation of the fission chamber to a newer ‘low count rate environment’ [discussed earlier in the chapter]. A number of interesting observations can be made from this ‘yield history’. One being that the upper two linear fits have been shown to be at different proton energies due to a drift in DVM setting, which has been calculated and shows good agreement with the shift in yield curve.

It is also plausible that some of the other ‘spreads’ in the yield curve are a consequence of a movement of the fission chambers into higher flux environments. Another more apparent reason is that the beam line and steering is leading to bombarding protons recording currents on the copper backing plate of the target but missing the target itself leading one to expect to see higher yield curves than those observed. [discussed in more detail in Chapter 4].

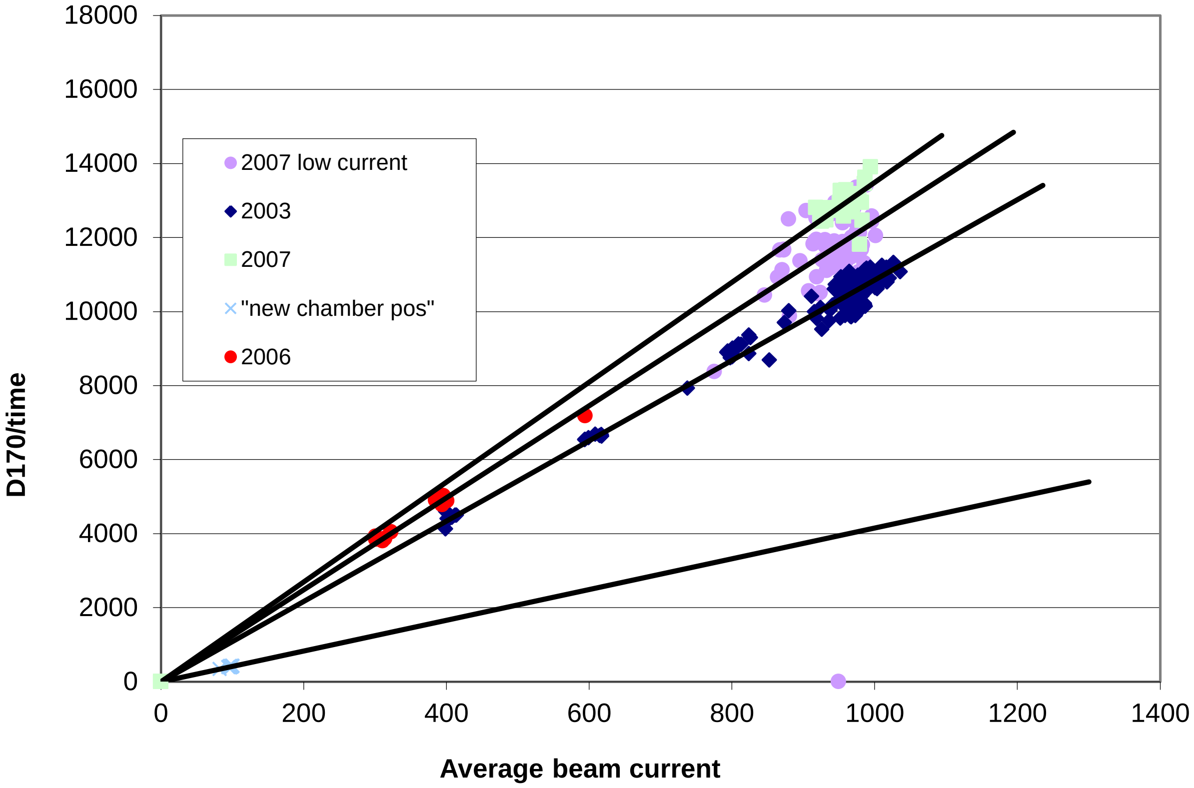

Figure 3.13 Neutron yield history of the Birmingham beam showing the change in fission count rate as recorded in the fission monitor chamber (D170) as a function of beam current.

3.4 Neutron Yields / ENDFB VII / SRIM

The drift in DVM calibration is evident from the preceding graphs. The change in neutron yield at higher incident proton energies can be easily calculated by taking the cross section for the Li(p,n)Be reaction from an evaluated nuclear data file (ENDFB VII) [figure 3.14(B)] and the mass stopping powers (calculated in the radiation transport code SRIM [5] [figure 3.14(A)]) and employing the thick target yield equation :

$$Y_{thick}(E_0) = \frac{N\int_0^{E_0} \frac{\sigma(E)}{dE/dx} dE}{q_d} \qquad (3.1)$$

Where,

$\sigma(E)$ = Energy dependant cross section (Li(p,n))

dE/dx = mass stopping power

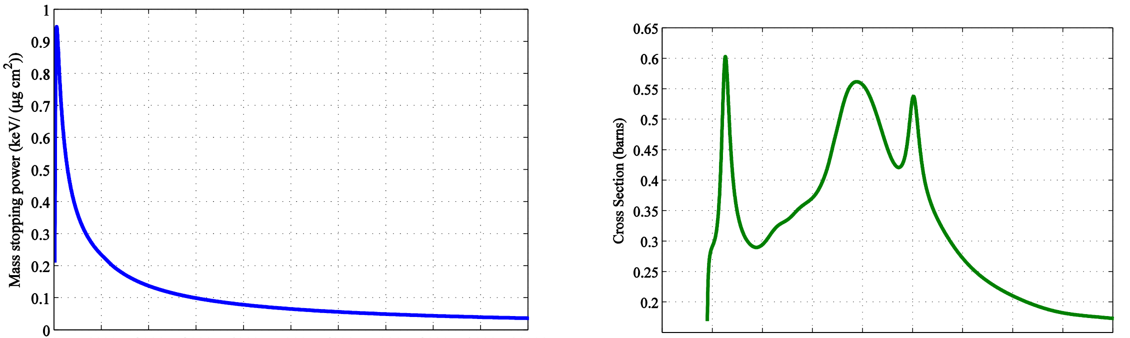

(A) (B)

Figure 3.14 Mass stopping powers for protons in lithium (A) and Li(p, n) interaction cross sections (B) as a function of proton energy.

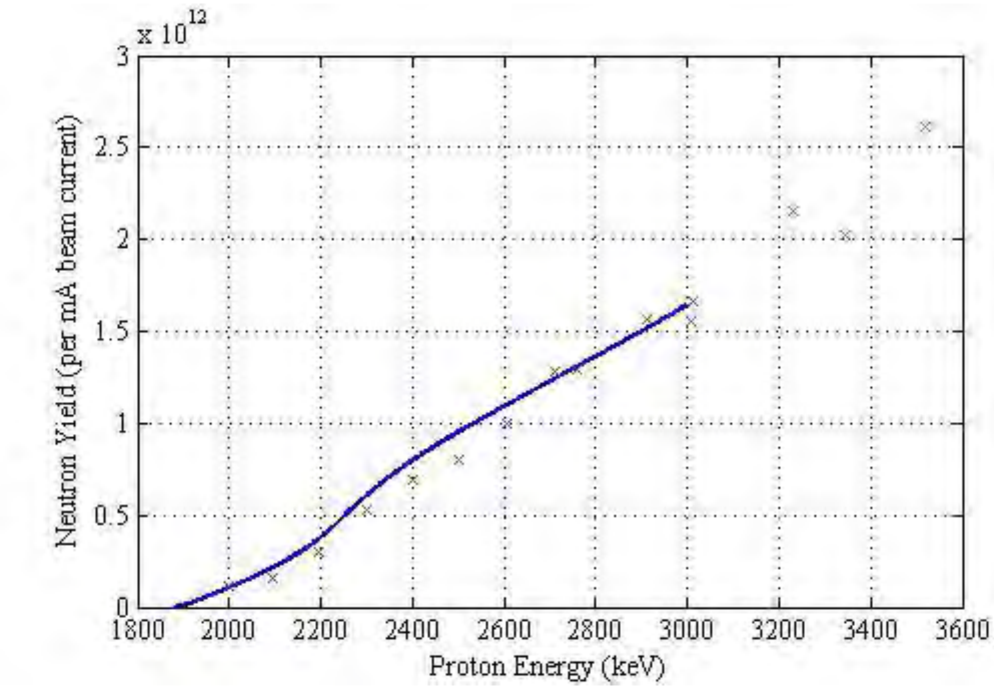

Figure 3.15 Neutron Yield plot as a function of proton energy (smooth line) along with experimental yield measurements (Campbell and Scott [8]).

Figure 3.15 shows historic measured thick target Li(p,n) yields [8] vs those calculated from the thick target yield equation. A change in proton energy from 2.8MeV to 2.9MeV results in an increase of neutron yield of 11%.

The Birmingham moderator/beam shaping assembly is calculated and engineered to be at its therapeutic peak when protons of 2.8MeV are accelerated onto a thick lithium target, [3]. Care has to be taken in order to prevent a systematic drift in voltage, over long periods of time, from impacting considerably on beam characteristics. This can only be done by carrying out regular calibrations and frequent Li(p,n)Be threshold checks.

With stabilised beam monitors, good historic data and a regular calibration procedure much more confidence can be placed in delivering a beam of nominal intensity and spectra for both experimental and clinical work in the future.

CHAPTER 4

EPITHERMAL NEUTRON BEAM DOSIMETRY – FOIL ACTIVATIONS

4.1 Foil Dosimetry

At any appreciable depth in a full scatter phantom, the impinging epithermal neutron spectrum is well moderated with a Maxwellian thermal distribution coupled with a 1/E tail.

With this in mind, the beam spectrum at any particular depth can be characterised by two quantities, the thermal neutron fluence rate (2200ms^{-1}) and the fluence per unit lethargy. With only these two unknowns, a suitable pair of foils is sufficient to quantify the fluence..

Using measured reaction rates in suitably paired foils, empirically calculated relationships between foil reaction rates can be exploited [9], to establish reaction rates in boron and nitrogen**:**

$$R(x) = [a \times R(Au)/R(Mn) + b] \times R(Mn) \tag{4.1}$$

Where,

$$a = \frac{\sigma_{0,x} \cdot I_j - \sigma_{0,j} \cdot I_x}{\sigma_{0,i} \cdot I_j - \sigma_{0,j} \cdot I_i}$$

$$b = \frac{\sigma_{0,i} \cdot I_x - \sigma_{0,x} \cdot I_i}{\sigma_{0,i} \cdot I_j - \sigma_{0,j} \cdot I_i}$$

I is the resonance integral and is defined as $I = \int_{0.55eV}^{\infty} \frac{\sigma(E)}{E} dE$,

Indices i and j refer to the foil pair being used and x, the material for which the reaction rate is sought.

Various combinations of foil are commonly used in clinical BNCT facilities: manganese and gold dilute foils in aluminium alloy are used by the clinical facility based at the Fir1 reactor VTT, Finland. These are chosen because of the manganese foil having a nearly 1/v absorption cross-section and the gold foil having a large resonance peak and its resonance integral is large compared to its thermal cross section.

Manganese and gold foil pairs are the subject of the remainder of the chapter and are the foils of choice in the Birmingham facility to determine doses in phantom. Two sets of foils are discussed, solid (i.e. non dilute) and dilute. For the non-dilute metal foils, the experimentally determined reaction rates require correction for flux depression caused by self-shielding and gamma self absorbtion before applying the spectral indices method above.

4.2 HpGe Efficiency Calibration and Cascade summing

All past reference foil activation measurements carried out at the University of Birmingham's BNCT facility to quantify the dose delivered in phantom [7] have been measured on a calibrated High-Purity Germanium Detector (HpGe) at distances of 10cm to 15cm with active non-dilute foils which are far enough from the active detector volume to limit the contribution of true coincidence events and minimize the effects of pulse pile-up. The activity induced in the newly acquired dilute foils (MnAl, 1.00 ±0.02% by weight Mn and AuAl, 1.00 ±0.01% by weight Au) is far less, per given irradiation, than that of the non-dilute foils due to the lower number of target atoms present in the foil. With lower activities it becomes extremely time consuming to counts foils at large distances from the detector surface with good statistics and this combined with the short half life of Mn makes the attempt to do so prohibitively difficult.

A thorough investigation was carried out on the effects of calibration source size, distance and detector efficiency using reference standard radionuclide point sources, including Co-60, Cs-137, Ba-133 and Eu-152, as a function of distance from the detector surface. As well as point sources a dilute, voluminous, mixed nuclide, [Nycomed Amersham plc, QCD1], traceable gamma-ray reference source containing 9 radionuclides spanning gamma ray energies 88.03keV (Cadmium-109) to 1333keV (Cobalt-60) was used. This mixed source is sealed between two plastic films and spans an area equivalent to the older Birmingham solid foils and served as a good measure of point source detector efficiency calibration and volume source detector efficiency calibration as a function of distance.

The results of the exercise showed that point source calibration and volume source calibrations agreed at large distances from the detector surface (>10cm) but as the sources approached closer to the detector a noticeable difference is seen in efficiency calibration curves and in order to avoid point/volume efficiency calibration errors, calibration and standard foil counting ought to be done at an extremely well positioned, reproduceable reference distance ~15cm from the detector surface.

Photopeak efficiency curves, at this new reference distance, were plotted in Matlab with weighted least squares fits, weighted by the individual estimated standard deviations of the reference radionuclide, fitted against an analytic model of HpGe efficiency as a function of energy of the form

$$\ln \varepsilon_\gamma(E_\gamma) = a_1 \ln E_\gamma + a_2(\ln E_\gamma)^2 - \frac{a_3}{E_\gamma^3} \qquad (4.2)$$

Activated gold and manganese foils range from 5mm in diameter (solid foils) to 12mm in diameter (dilute foils). Another problem which arises as you move closer to the detector surface for counting is that our efficiency calibrations had been all done with point sources and as you approach closer to the detector surface our foils which have quite large diameters (5mm to 12mm) no longer behave like point sources.

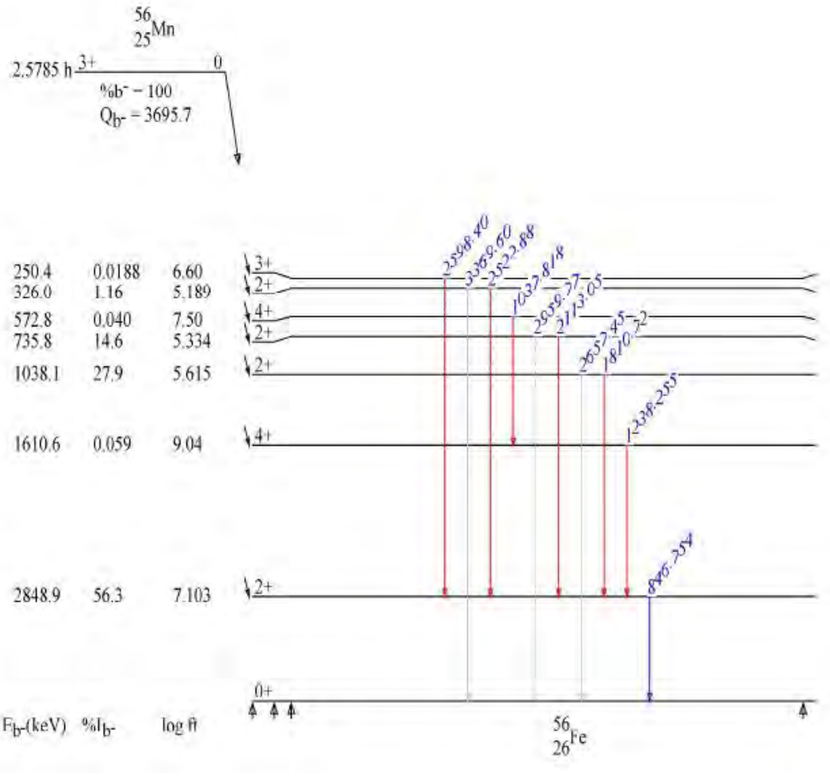

Figure 4.1 Nuclear decay scheme of activated manganese foil.

From the Mn decay scheme (figure 4.1) it can be seen that the 847keV gamma ray used to quantify the saturated activity induced in the Mn foil for a given neutron flux is related in a complex way to the cascading decay of gamma rays of other energies - shown highlighted in red on the decay scheme. These cascading effects are often referred to as ‘true coincidence’ or ‘cascade summing’ events in the literature.

The fact that these cascading nuclear decays occur on the pico and femto second timescale, which is within the resolving time of a typical HPGe detector, is of concern when measuring weakly active foils close to the detector surface. If these coincident events together enter the detector active volume at the same time they no longer show up as unique full energy peak lines in a spectra but a summed total. Hence these combinatorial events are often referred to as cascade summing or true coincidence summing events as opposed to random coincidence events. Cascade summing does not occur in gold foils at the reference 411keV photo – peak.

True coincidence events, which relates wholly on the geometry of the problem, decrease with increasing distance from the active volume because of the diminishing solid angle into which both coincident photons have to traverse in order to cause the summative effect in the detector.

Thus it is necessary, with dilute foils of weak activity, to address the problem of counting the foils at a more practical distance i.e. closer to the detector, and factoring in of coincident events into the counting process is necessary.

A simple method was employed to correct for the increased summing effect and increased geometrical problems caused by non-point size objects as they move ever closer to the detector surface.

The correction for cascade summing and geometric effects relies on the assumption that point and volume sources behave alike at large distances from the detector surface and that cascade summing is negligible at these distances. Knowing the efficiency and relative efficiency thus leads us to the corrected efficiency at the new point of measurement with all geometric anomalies factored in.

4.3 Foil Correction factors

For a decaying foil, having been activated in a neutron beam, the saturated activity, A_{sat}, induced in the foil can be calculated using equation 4.3 [10], with additional correction factors applied for $c_s, c_\gamma, c_\emptyset$, self shielding, gamma self absorbtion and variable neutron flux during irradiation respectively.

$$A_{sat} = \frac{\lambda(C-B)}{\varepsilon I\left(1-e^{-\lambda t_o}\right)e^{\lambda t_o}\left(e^{-\lambda t_1}-e^{-\lambda t_2}\right)} \; c_s c_\gamma c_\emptyset \qquad (4.3)$$

Where,

λ : decay constant for radionuclide of interest,

$C - B$: net area in photopeak (counts – background);

ε : Full energy Photopeak efficiency of detector,

I : gamma ray decay probability,

t_o : irradiation time,

t_1 : cooling time (transit time),

t_2 : measurement time

c_s : correction factor for neutron self shielding

c_{γ} : correction factor for gamma ray self asborption

$c_{\emptyset}$: correction factor for fluctuation in neutron flux over irradiation time

4.3.1 Corrections for yield fluctuations ($c_{\emptyset}$)

In 2011 a new National Instruments hardware and software monitoring system was installed on the accelerator by Phoenix et al. [19]. The safety system primarily monitors temperatures on the copper backing plate on to which the lithium target is heat bonded. But also serves a number of other purposes now including the continuous monitoring of the beam current on target, collected from a Keithley electrometer, and the neutron monitor (fission) chamber counts [discussed in Chapter 3.] collected from a scalar NIM module, via a NI PCI-6602 8-Channel 32-bit Counter/Timer.

This has now led to the ability to monitor near instant yields i.e. the ratio of the number of neutrons produced per unit current, and for the operators to fine tune and correct magnetic steering and focusing to improved levels during long irradiations.

It has also shed light on the continuous variability of the yield during long and short irradiations, which fluctuates more than the evident counting statistics observed in the detectors alone and often shows a distinct drift over the time course of the irradiation. Figures 4.2 , 4.3 and 4.4 show an example of the measured variation in neutron count rate at beam exit, beam current on target and neutron yield per unit source current at progressive 5s time bins throughout a long irradiation. The yield moves clearly from 0.06 at the start of the irradiation to 0.05 by the end.

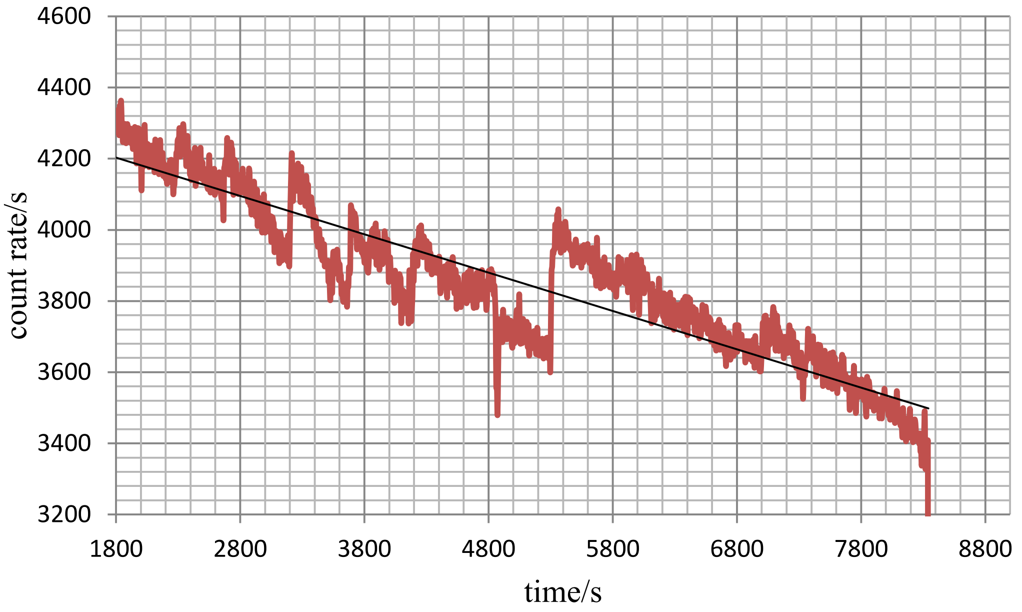

Figure 4.2. Measure of the Variation of neutron flux with time, as seen by the reference pulse fission chamber located near the aperture of the beam exit port. Counts are collected in 5s time interval.

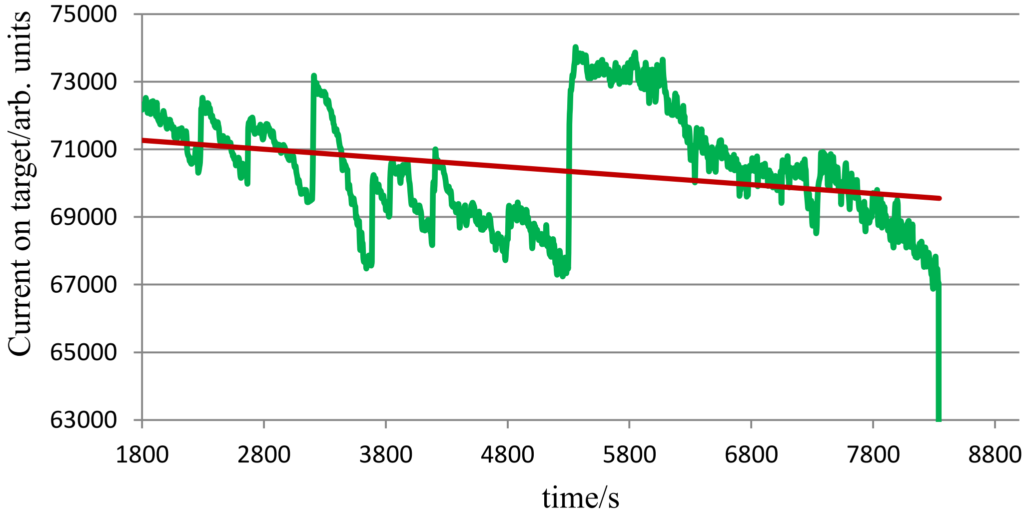

Figure 4.3. Measure of the Variation of beam current on target with time, as recorded by the Keithley electrometer. Counts are collected in 5s bins.

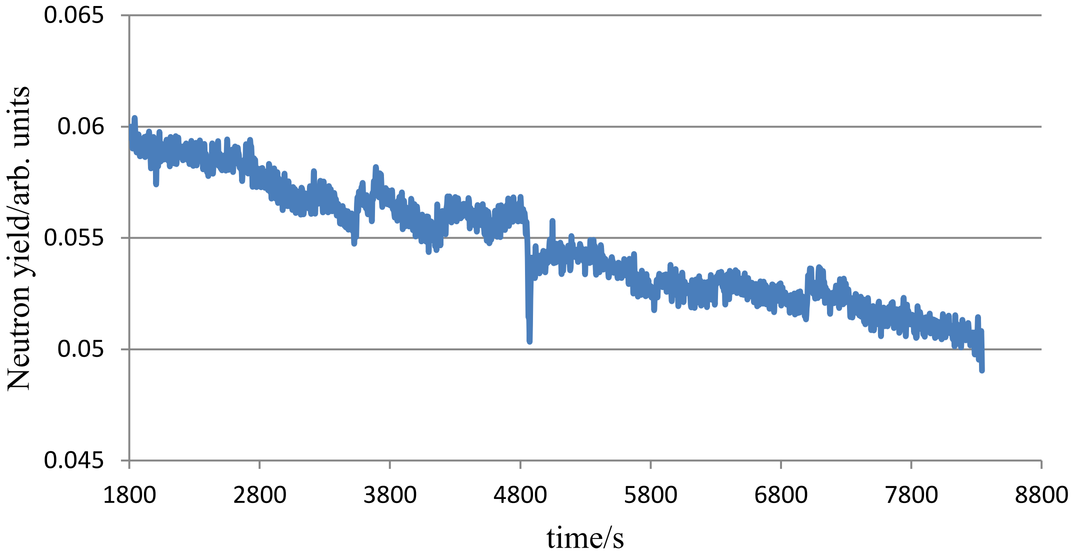

Figure 4.4. Measure of the Variation of neutron yield with time. Counts are collected in 5s bins.

It has been long thought that the normalisation factor between full Monte Carlo simulations of thermal dose in the large water tank [LWT] and measured foil activations derived thermal doses, was likely due to the imperfect collimation of the proton beam line [7]. Leading to a fraction of protons missing their target yet still recording a current on the copper backing plate from which the beam current is monitored.

This has become ever more evident during the last change in target, figure 4.5 (a) shows the replaced target with distinctive scorch marks on the copper backing outside of the target area, figure 4.5(b) shows the same target with demarcated target area, filled black circle, with a white circle demarking the estimated beam rastor size, some of which misses the target yet hits the scorched zone on the backing plate.

An estimate of the loss of beam on target can be made from the ratio of arc angle off target to that on target, which seems to be ~70%. This estimate depends on how often the rastered proton beam drifts or is steered off target during an irradiation and serves as a very rough approximation on beam losses. In view of these problems it becomes almost impossible to base flux and dose calculations from foil activations on the integrated current alone and hence all corrections for variation in neutron beam intensity, whatever the cause, during a typical foil activation run are now corrected for by the fluctuation observed in the neutron beam monitors at the beam exit.

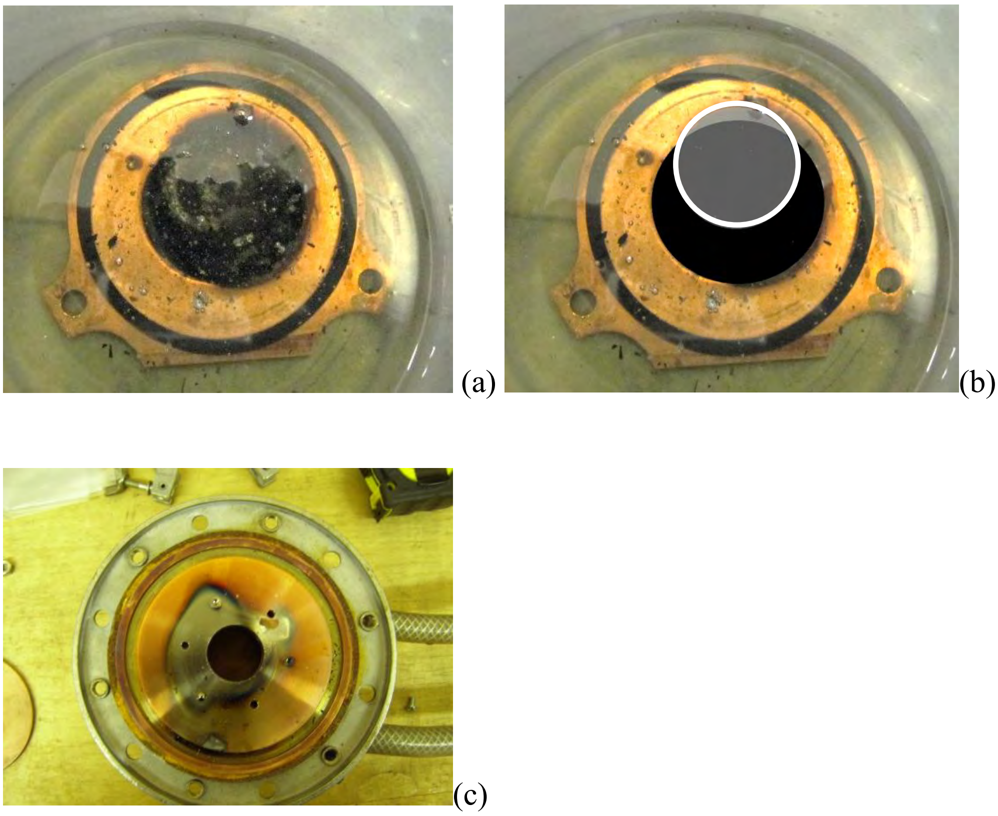

Figure 4.5. (a) Used lithium target and copper backing (removed from the beam line). (b) The same target with black filled circle demarking the lithium target and white circle showing a plausible rastered beam missing part of the target. (c) Beam collimator showing definitive markings of beam missing the aperture by large margins.

The correction factor, $c_{\emptyset}$, which corrects the measured saturated activity for a non uniform, time varying flux, can be calculated from [11]:

$$c_{\emptyset} = \frac{c'}{c} = \frac{\bar{\phi}(1-e^{-\lambda t_{irr}})}{\sum_{i=0}^{n} \phi_i((1-e^{-\lambda \Delta t})e^{-\lambda(n-i)\Delta t}} \tag{4.4}$$

c’ and c being the gamma ray counts measured as a consequence of a uniform and non-uniform irradiation respectively.

$$c = \sigma\{\sum_{j=1}^{n} \phi_j \left(1 - e^{-\lambda t}\right) e^{-\lambda(n-j)\Delta t}\} e^{-\lambda t_c}(1 - e^{-\lambda t_m})\lambda^{-1} e_\gamma \varepsilon_\gamma N \tag{4.5a}$$

$$c' = \bar{\phi}(1 - e^{-\lambda t_{irr}})e^{-\lambda t_c}(1 - e^{-\lambda t_m})\lambda^{-1} e_\gamma \varepsilon_\gamma N \tag{4.5b}$$

Where,

c’ : number of gamma rays emitted under an irradiation of constant flux

σ : cross section,

n :number of total time bins,

ϕ_j : fraction of flux at time bin j in the fission monitor chamber,

λ : decay constant,

Δt : bin width of measurements,

e_γ : gamma emission probability,

ε_γ : detector efficiency,

N : number density of atoms

In typical circumstances, during long foil irradiations, this correction factor is less than 1% unless there is a systematic large drift in neutron flux, as recorded in the fission chambers, from the beginning to the end of the irradiation. Large fluctuations in flux without significant drift over the irradiation period tend to balance out.

4.3.2 Correction for gamma self-absorption (c_γ)

Gamma self absorption coefficient can be calculated using [12] mass attenuation coefficients for gold and the known thickness of the foil. Gold has a mass attenuation coefficient of 0.218 g/cm^2 at photon energies of 400keV, the density of gold is 19.29 g/cm^3 and the approximate foil thicknesses is 130μm for the Birmingham solid gold foils. This results in a self absorption correction of:

$$e^{-\left(\frac{\mu}{\rho}\right)_{Au}\rho d} \tag{4.6}$$

$$=\exp(-0.218*0.0065*19.29)=0.973$$

Rogus [36] calculated similar self absorption factors at MIT for foils of 0.0051cm thick and using lead mass attenuation coefficients, resulting in a 411keV self absorption coefficient of 0.989.

Experimentally calculated Reaction Rates require correcting for flux depression and self shielding caused by the non homogeneous distribution of neutron flux across the foil and self shielding factors resulting from photon interactions and attenuation.

Defining the self shielding factors in the foils as the ratio of the reaction rates per atom in the detectors to the same reaction rates in an infinitely thin detectors. These factors were determined by means of MCNP calculations and were verified experimentally to be in excellent agreement with simulated results. The correction factors for flux depression and self shielding as well as their impact on the derived thermal neutron dose (in tissue) follow.

4.3.3 Neutron self-shielding effects and correction factors for foil activation measurements (c_s)

Monte Carlo simulations were carried out using MCNPX to quantify the degree of self shielding caused by non-dilute foils. Simulations directly compare self shielding effects in dilute and non-dilute foils. The simulations tallied the track length estimate of flux in both dilute and non-dilute foils at various depths in the LWT. These tallies were multiplied by the neutron energy dependant (n,γ) capture cross-sections of the Mn and Au foils respectively.

The ratio of the dilute to non-dilute saturation activities is the derived correction factor to be applied to non-dilute foils. Separate calculations were performed to determine the correction factors from dilute foils to water.

Saturation activity in the foils change rapidly with depth (as shown in figures 4.6. and 4.7.). It was therefore deemed necessary to put an upper and lower bound on the simulated results caused by the ±1 mm positional uncertainty on the non-dilute foils. A cubic spline was fitted to the MCNP simulated data for the dilute foil saturation activities vs depth (not shown). Activities 1 mm either side of the assumed measured foil position were then determined.

Experimental work has been carried out to assess the validity of these calculated correction factors in the standard LWT. Non-dilute foils were used as follows:

- Mn/Ni (88 % Mn by wt.) of approx 7 mm diameter and 35 mg mass.

- Au of approx 5 mm diameter and 50 mg mass.
- Dilute foils were approximately 12 mm in diameter and 60 mg in mass [MnAl (1% Mn by wt.), AuAl (1% Au by wt.)].

Two rods were inserted 7 cm apart into the phantom, parallel to the neutron beam central axis. Each rod was loaded with either five dilute or non-dilute foils. With this experimental setup dilute and non-dilute foils were irradiated simultaneously overcoming any problems with irradiation reproducibility.

Each activation run was set such that the induced activity in the dilute foils was sufficient to arrive at good counting statistics (<1 %) on a HpGe detector in a reasonable time. The measured counts were converted to saturation activities per gram and the ratio of the saturation activities for dilute to non-dilute foils is the experimental correction factor.

In carrying out the experimental work it was noted that the depth at which the dilute foils were positioned couldn't be ascertained to better than an uncertainty of ±1 mm, whereas the non-dilute foils were positioned in a far more precise manner with a positional uncertainty of < ±0.5 mm. This mandated the additional calculations described previously to address the positional uncertainty of the dilute foils.

All results are presented for the neutron field generated by the action of a 1mA proton current in the Birmingham facility described by Culbertson et al. [7]. Figures 4.6. and 4.7. show the measured saturation activity per gram of activation material in the foil, for manganese and gold foils respectively.

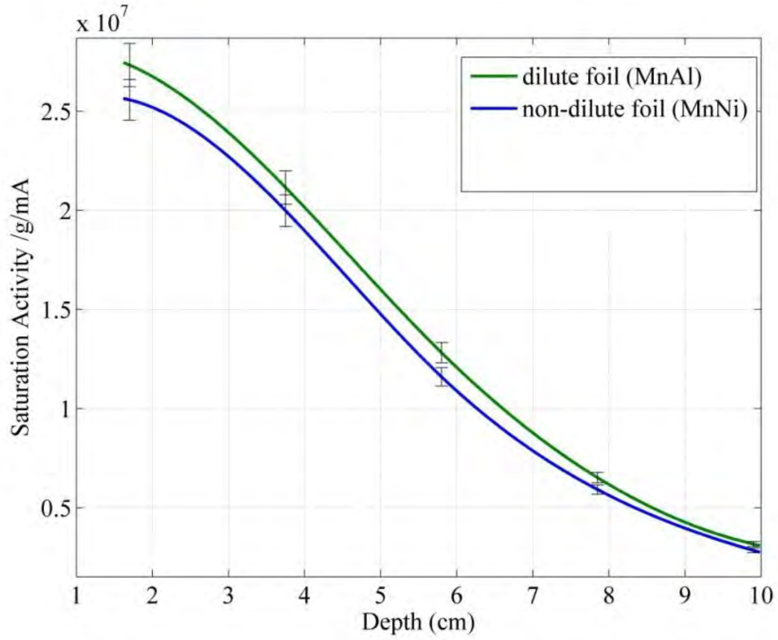

Figure 4.6. Experimental saturation activity per gram/mA in non-dilute (blue line) and dilute Mn foils (green line) as a function of depth.

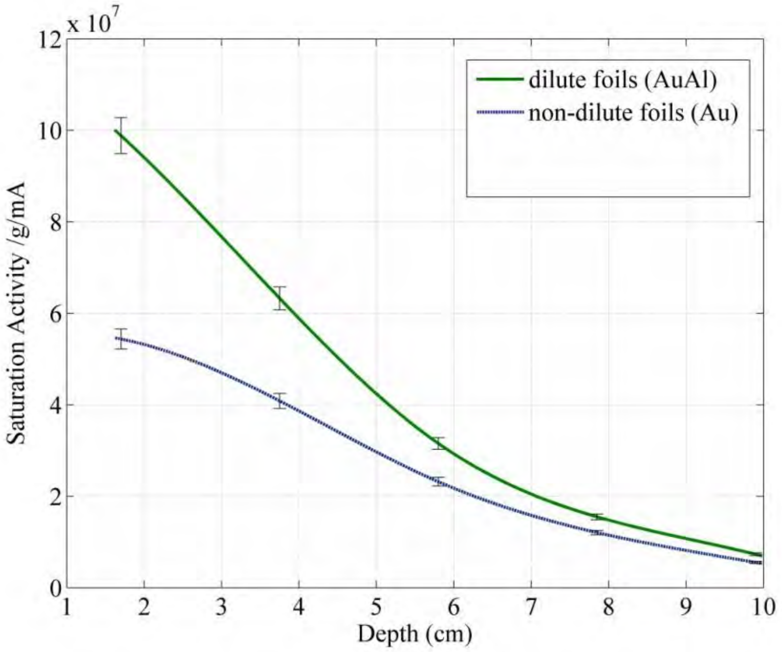

Figure 4.7. Experimental saturation activity per gram/mA in non-dilute (blue line) and dilute Au foils (green line) as a function of depth.

These figures show that flux depression / self-shielding is a factor in both sets of foils, with the dilute foils reaching higher levels of saturation activity per gram when irradiated with an identical neutron fluence to the non-dilute foils.

Figures 4.8 and 4.9 show the experimental and simulated correction factors for Mn (Figure 4.8.) and Au (Figure 4.9.) foils. The experimental uncertainties shown are to 2σ (i.e. a 95% confidence level).

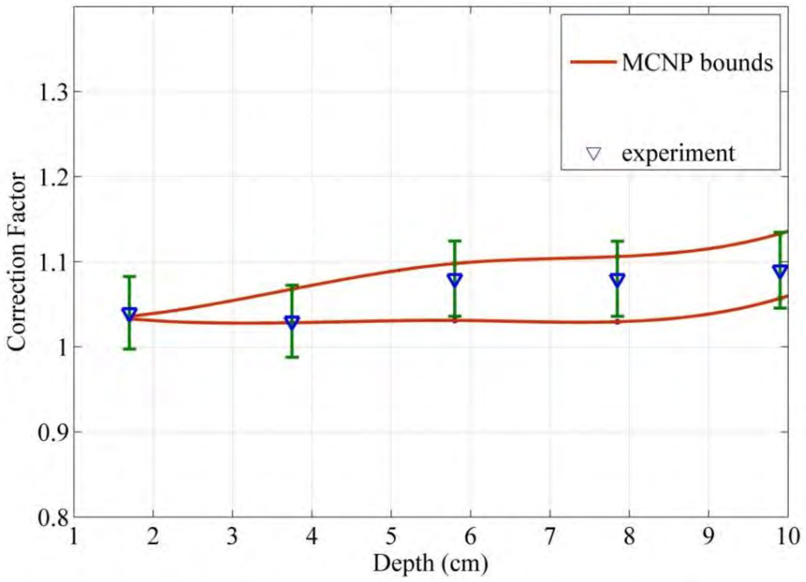

Figure 4.8. manganese foil experimental and simulated self shielding correction factors as a function of depth in LWT [triangular points represent experimental data, red lines represent upper and lower bounds of the MCNP simulation].

The bounds (red lines) shown plotted in Figures 4.8. and 4.9. result from the simulations to assess the impact of the ±1 mm positional uncertainty on the dilute foil. Within this uncertainty bound the experimental and simulations show matching trends with depth for each foil material and similar overall values.

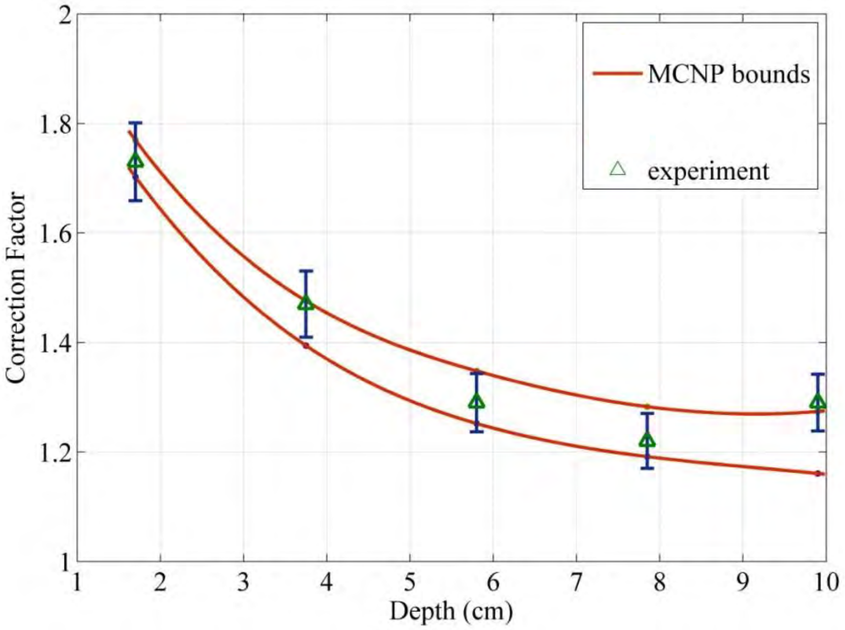

Figure 4.9. Gold foil experimental and simulated self shielding correction factors as a function of depth in LWT [triangular points represent experimental data, red lines represent upper and lower bounds of MCNP simulation].

Further simulations show that the perturbation by the neutron flux for dilute foils is negligible and hence these foils are water equivalent.

Previous work [7] had reported correction factors of 5.5% for non-dilute Mn foils and 17.5% for non-dilute Au foils. This work also suggested that correction factors do not change significantly with depth. These results are now superceded by the current work, where for Mn the correction factor is approximately 6.5% near the beam entrance (up to 4 cm deep) rising to 10% at the brain midline (7 cm). For Au the correction factors are up to 80% at 2 cm deep falling to 30% at the brain midline.

The primary goal of Mn and Au foil activations is the derivation of the boron and nitrogen dose components. Further work is necessary to examine the impact of our findings on the Au/Cd difference method, but analysis has been performed for the method reported by Freudenreich [9].

Figure 4.10. shows the relationship between the perturbation correction factor and kerma for the $^{14}N(n,p)$ reaction determined by the Freudenreich method. For the non dilute Mn foils used in this work, correction factors range from 6% to 10% with depth and require the Nitrogen dose multiplication factor ranging from 1.06 to 1.10 (i.e. the relationship between correction factor and kerma is linear for Mn foils). For the Au foils it was found that even the large correction factors that have been determined at shallow depths have relatively small (approx. 2%) effect on the derived boron and nitrogen kerma when evaluated with the Freudenreich method.

It should be noted that while this work has brought much greater understanding of the neutron flux perturbation in a changing spectrum as a function of depth, previous publications on the dosimetry results for boron and nitrogen kerma [7] are not significantly changed, as uncertainties of ±10% were reported.

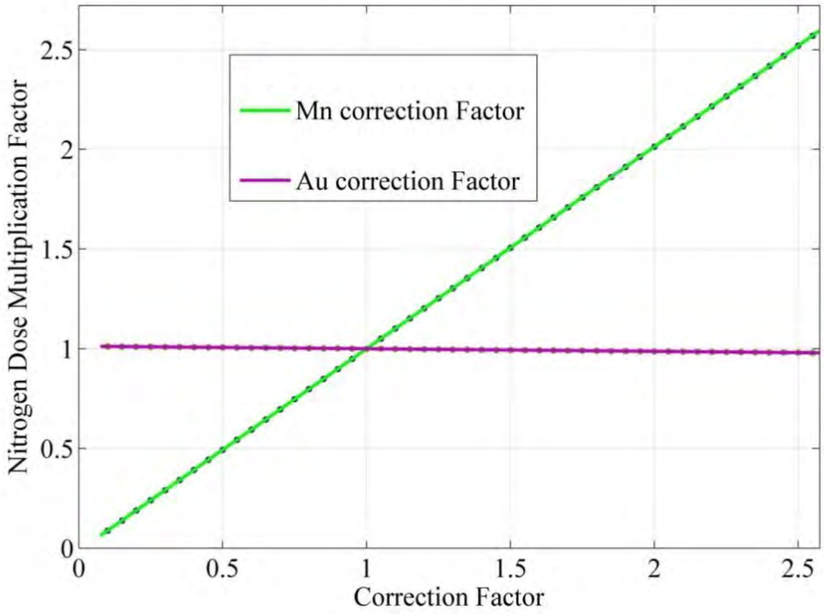

Figure 4.10. Effect of Au (purple line) and Mn (green line) foil correction factors on the derived nitrogen dose. [NB. No covariance is plotted here].

Experimentally determined correction factors for non-dilute foils show extremely good agreement with those simulated. When using such non dilute-paired foils for dosimetry these correction factors cause a small but important correction to the derived nitrogen and boron dose components.

Self shielding correction factors were calculated by computing the neutron (n,gamma) capture reaction rates in the volume equivalent to that of the foil whilst using an unperturbed flux distribution (by the presence of the foil) vs that of the perturbed flux distribution [transport in water vs transport in Mn (or Au)], and multiplying, with a tally multiplier card, by the appropriate continuous energy thermal neutron capture cross section. The ratio of the unperturbed flux calculation to that of the perturbed measurement is a measure of the Self absorption caused by the presence of the foils.

Gold foils required ~2.5% correction for 411keV gamma self-absorption, where as the manganese foils (846keV gamma rays) self absorption was negligible.

The Monte Carlo calculated thermal to epithermal flux ratios measured at various depths in the LWT, are shown in table 4.1, assuming an effective cadmium cut off of 0.55eV. The results show the evident thermalising of an impinging epithermal beam. The resonant self shielding component of the beam spectra therefore varies as a function of depth in phantom and becomes an ever diminishing component of the total self shielding factor (resonant and thermal combined) with the rapidly decreasing epithermal fraction of the beam spectrum.

Depth in Phantom [cm]	Thermal flux [n/cm^2/s] $\leq$ 0.55eV	Epithermal flux [n/cm^2/s] >0.55eV	Thermal to epithermal flux ratio
2.7	3.82E+08	7.86E+07	4.86
3.7	3.26E+08	4.14E+07	7.88
5.2	2.21E+08	1.44E+07	15.34
7.2	1.15E+08	3.31E+06	34.81
9.2	5.47E+07	6.84E+05	79.95

Table 4.1 Variation in neutron flux spectrum as a function of depth in phantom.

Shcherbakov et al. [13] have developed a Pade approximation of the Doppler broadening function to calculate resonance self-shielding factors for use in activation measurements. The authors have shown that this method of calculation is in excellent agreement with experimental measurements and is both fast and accurate (figure 4.11). From figure 4.11, Solid Birmingham foils have a very large resonance self shielding factor of ~0.16, compared to 0.28 for the 5e-3cm thick foils used by MIT. The thickness of the dilute foils is difficult to gauge as target atoms are dispersed in a malleable metal (aluminium) and there regular solid density doesn’t readily translate into a volume or thickness – none the less the small number of atoms present in a thin foil (1% by weight) would suggest a maximum foil thickness resulting in self shielding factors approaching unity in figure 4.11.

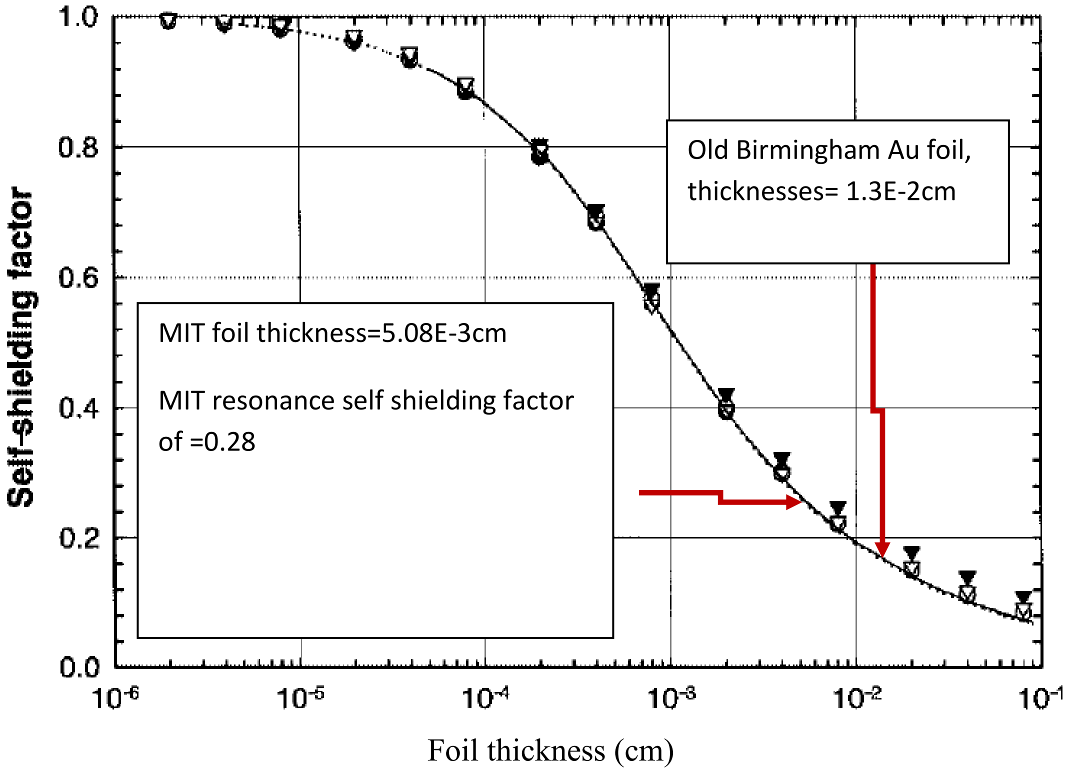

Figure 4.11 Comparison of experimental and calculated values of resonance self-shielding factor <Gepi> for ^{197}Au as a function of foil thickness for istotropic neutron flux. With markers signifying the solid and dilute Birmingham gold foils and the MIT gold foils. [13]

4.4 Thermal Neutron dose calculations from foil activations

Experimentally determined reaction rates of neutron capture in the twin foils can be used using Freudenreich’s spectral indices method [9], which is an empirically calculated relationship, to establish reaction rates in other elements of interest including nitrogen and boron, from which their thermal neutron capture Kinetic Energy Released Per Unit Mass [KERMA] and hence dose can be deduced.

Activating foils via the (n,γ) capture reaction is commonplace in BNCT dosimetry to determine thermal neutron fluxes and doses. Various combinations of foil are commonly used in clinical BNCT facilities: manganese and gold dilute foils in aluminium alloy are used by the clinical facility based at the Fir1 reactor VTT, Finland. These are chosen because of the manganese foil having a nearly 1/v absorption cross-section and the gold foil having a large resonance peak and its resonance integral is large compared to its thermal cross section.

$$R\left({}^{14}N\right)=\left[-5.05\times10^{-4}\times R(Au)/R(Mn)+0.140\right]\times R(Mn)$$

$$KERMA=\frac{R\left({}^{14}N\right)\times E\times F}{M\times M_{AMU}} \qquad (4.7),(4.8)$$

Where,

R is the reaction rate calculated from the empirical relationships

E is the average energy released per reaction i.e.

$$\left(2.31 MeV\ for\ {}^{10}B\ and\ 0.62\ MeV\ for\ {}^{14}N\right)*1.6\times10^{-13}\ J$$

F is the fraction by weight of the isotope which is $1*10^{-6}$ for 1 μg/g ^{10}B, and $1x10^{-2}$ for 1% ^{14}N

M is the atomic mass of the isotope (10 for ^{10}B, and 14 for ^{14}N)

M_{AMU} is the atomic mass unit (=1.666 10^{-27} kg)

With this in mind foil activations were carried out as per European Recommendations. Foil and ionisation chamber measurements were carried out in the Birmingham Large Water Tank, as well as a secondary measure of fluence via the cadmium difference method.

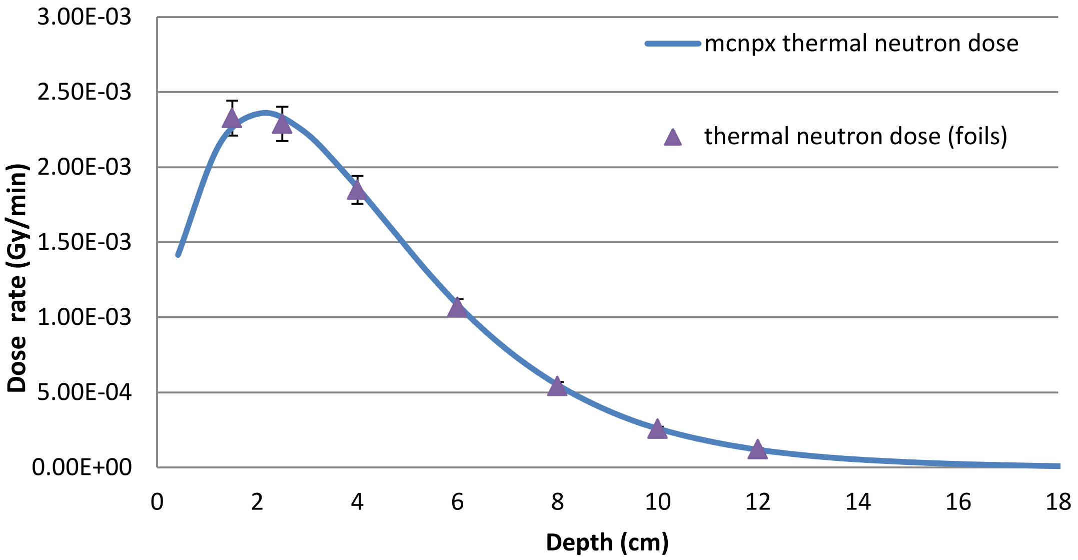

Figure 4.12 Thermal neutron dose [Gy/min] measured with AuAl and MnAl foil pairs (symbols), with MCNPX calculated thermal dose (solid line) as a function of depth in a Large Water Tank.

The thermal neutron dose measured with activation foils as per the spectral indices approach in the Birmingham beam, figure 4.12 shows extremely good normalised depth dose profiles in the Large Water Tank. Normalisation factors vary depending on the neutron yield produced and the degree of leakage current recorded in the copper backing from the collimation problems discussed earlier. In recent years this factor (which normalises calculated, MCNPX, dose rates to measured) has ranged from ~0.6 to 0.83.

The expanded uncertainty in the calibration sources used for the HPGe efficiency calibration are known to be 2% (at 2σ). The uncertainties in the re-weighed mass of the foils is thought to be about 3%. Uncertainties in the counting statistics were resolved to better than a 1% uncertainty.

The uncertainties in the measured saturated activity is thus thought to be ~7% - this being an upper liberal estimate.

MEASURED/CALCULATED QUANTITY	UNCERTAINTY
Foil masses	3%
Calibration source uncertainty (1σ)	1%
HpGe Detector efficiency	2%
Foil position in phantom	±1mm
Counting statistics	<1%
Self shielding	~1% (statistical)
Gamma self absorption	~1% (statistical)

Table 4.2 Uncertainties in foil activation measurements.

In order to minimise the effects of changing beam characteristics between dosimetry measurements and cell irradiations ‘local’ foil dosimetry measurements were carried out in close proximity, often on the same day, as cell irradiations until beam collimation issues can be fixed.

Chapter 5

NEUTRON INTERACTIONS AND DOSE COMPONENTS

The dominant interactions resulting from a broad spectrum of low energy, overwhelmingly thermal neutrons interacting with organic matter (such as human brain tissue) arise primarily in the abundant elements: carbon, hydrogen, nitrogen, oxygen and chlorine, via thermal neutron capture reactions resulting in the release of an even more diverse set of particles including, protons, gamma rays and recoiling carbon ions.

The major sub-components of the dose produced by an epithermal neutron beam impinging on boron loaded tissue consist of:

- Boron Dose to tissue (15 μg/g of ^{10}Boron) $^{10}B(n,\alpha)^{7}Li$

- Hydrogen Dose (Proton recoil) $^{1}H(n,n')^{1}p$. The fast neutron dose or hydrogen dose D_H is mainly due to the proton recoil reactions for high energy neutrons in tissue. Protons, produced by $^{1}H(n,n')p$ reaction, deposit their energy locally. This dose component is highest at the skin surface and decreases rapidly with depth.

- Thermal neutron dose or nitrogen dose D_N is due to the thermal neutron capture by nitrogen nuclei: $^{14}N(n,p)^{14}C$. Dose results from locally deposited energy from the energetic proton (580 keV) and the recoiling ^{14}C nucleus. Thermal neutron capture in nitrogen constitutes 96.4% of the total thermal neutron dose in Brain tissue – thus the terms thermal dose and nitrogen dose are often used interchangeably.

- Photon Dose D_γ, is a combination of the gamma rays accompanying the neutron beam and the gamma rays induced in the tissue/cell volume. The gamma dose in tissue results primarily because hydrogen in tissue absorbs thermal neutrons in ${}^{1}H(n,\gamma)^{2}H$ reaction and emitting 2.2 MeV gamma rays.

The absorbed dose resulting from a known neutron energy spectrum can be readily calculated from tabulated fluence to KERMA factors [14]. Figure 5.3 shows KERMA factors for ICRU Brain, used here in MCNPX to calculate dose to brain tissue/tumour (figure 5.1).

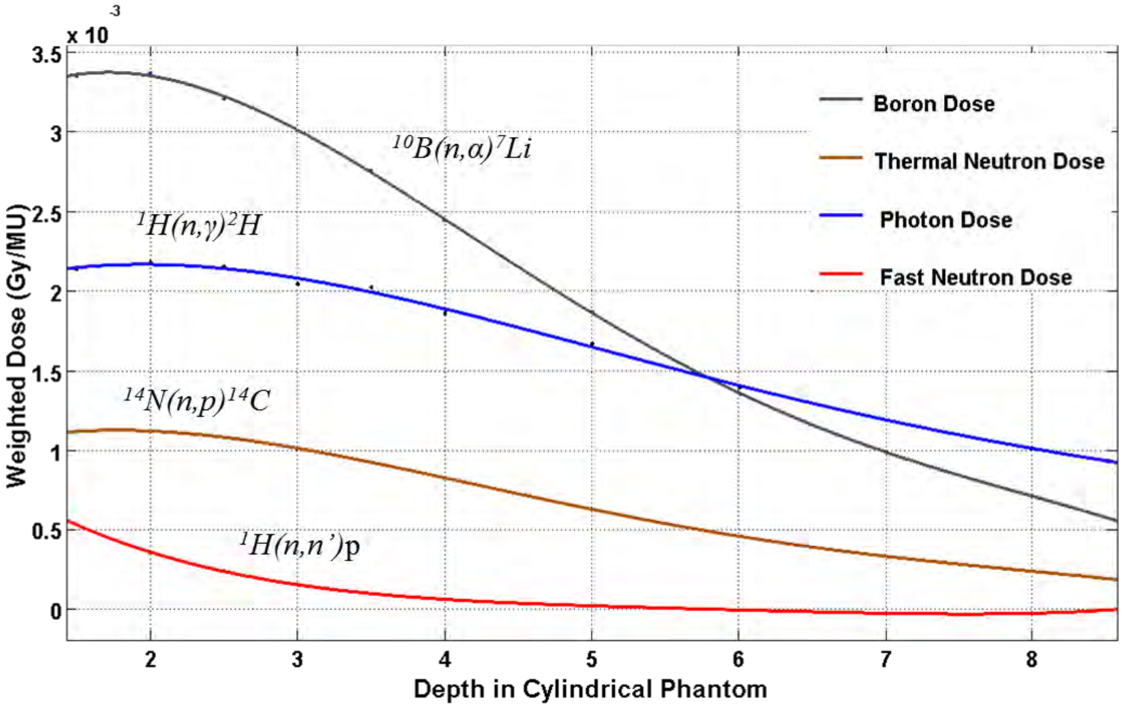

Figure 5.1 Biologically weighted dose components [MCNPX] scaled to experimental data.

Calculated physical dose components for the Birmingham beam are shown in table 5.1.

	thermal flux [cm^{-2} s^{-1}]	Thermal [Gy/min]	Fast [Gy/min]	Photon [Gy/min]	Boron 50ppm [Gy/min]	boron dose fraction	photon fraction
flask 2cm	3.60E+08	3.27E-03	1.04E-03	2.73E-02	8.01E-02	7.17E-01	2.44E-01
flask 5cm	1.86E+08	1.73E-03	9.13E-05	2.16E-02	4.19E-02	6.42E-01	3.30E-01

Table 5.1 Physical macroscopic dose components and their fractions of total dose calculated using MCNPX for the Birmingham beam at 1mA.

5.1 Biologically Weighted Dose

Weighted doses are often calculated by multiplying calculated physical doses with an appropriate Relative Biological Effectiveness (RBE) or Compound Biological Effectiveness (CBE) factor. Which effectively translate the radiation damage caused by a particular type and distribution of radiation to a photon only irradiation resulting in an equivalent biological endpoint. Table 5.2 shows commonly used, radiobiology derived, RBE/CBE factors in BNCT.

Dose Component	**Relative Biological Effectiveness/Compound Biological Effectiveness**
Boron – healthy tissue	1.3
Boron – tumour tissue	3.8
Hydrogen (Proton recoil) $^{1}H(n,n')^{1}H$	3.2
Nitrogen (thermal neutron capture)	3.2
Photon	1

Table 5.2 Commonly used RBE/CBE factors in BNCT for human brain tissue.

The four most significant weighted dose rate components summed give a total tissue or tumour weighted dose rate:

$$\dot{D}_{total,tis} = \dot{D}_B(z)\cdot CBE_{B,tis} + \dot{D}_N(z)\cdot RBE_N + \dot{D}_H(z)\cdot RBE_H + \dot{D}_\gamma$$

Where

$\dot{D}_{total,tis}$ = Biologically weighted Dose rate to Healthy Tissue at that point

$\dot{D}_B(z)$ = Boron Dose rate in tissue at (z)

$CBE_{B,tis}$ = Compound Biological Effectiveness of Boron in tissue.

$\dot{D}_N(z)$ = Nitrogen Dose rate

RBE_N = Relative Biological Effectiveness of Nitrogen

$\dot{D}_H(z)$ = Hydrogen Dose rate

RBE_H = Relative Biological Effectiveness of Hydrogen

$\dot{D}_\gamma$ = Photon Dose rate

$CBE_{B,tum}$ = Compound Biological Effectiveness of Boron in tumour

The summed and weighted biologically relevant doses to brain tumour and healthy tissue are shown plotted in Fig 5.2. The tumour dose being far greater than the tissue dose.

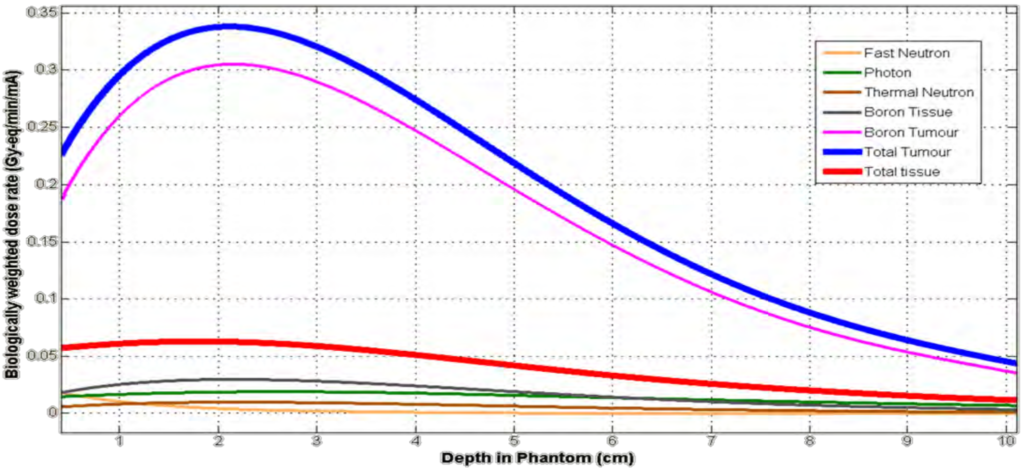

Figure 5.2 Summed Biologically weighted dose components [MCNPX] scaled to experimental data.

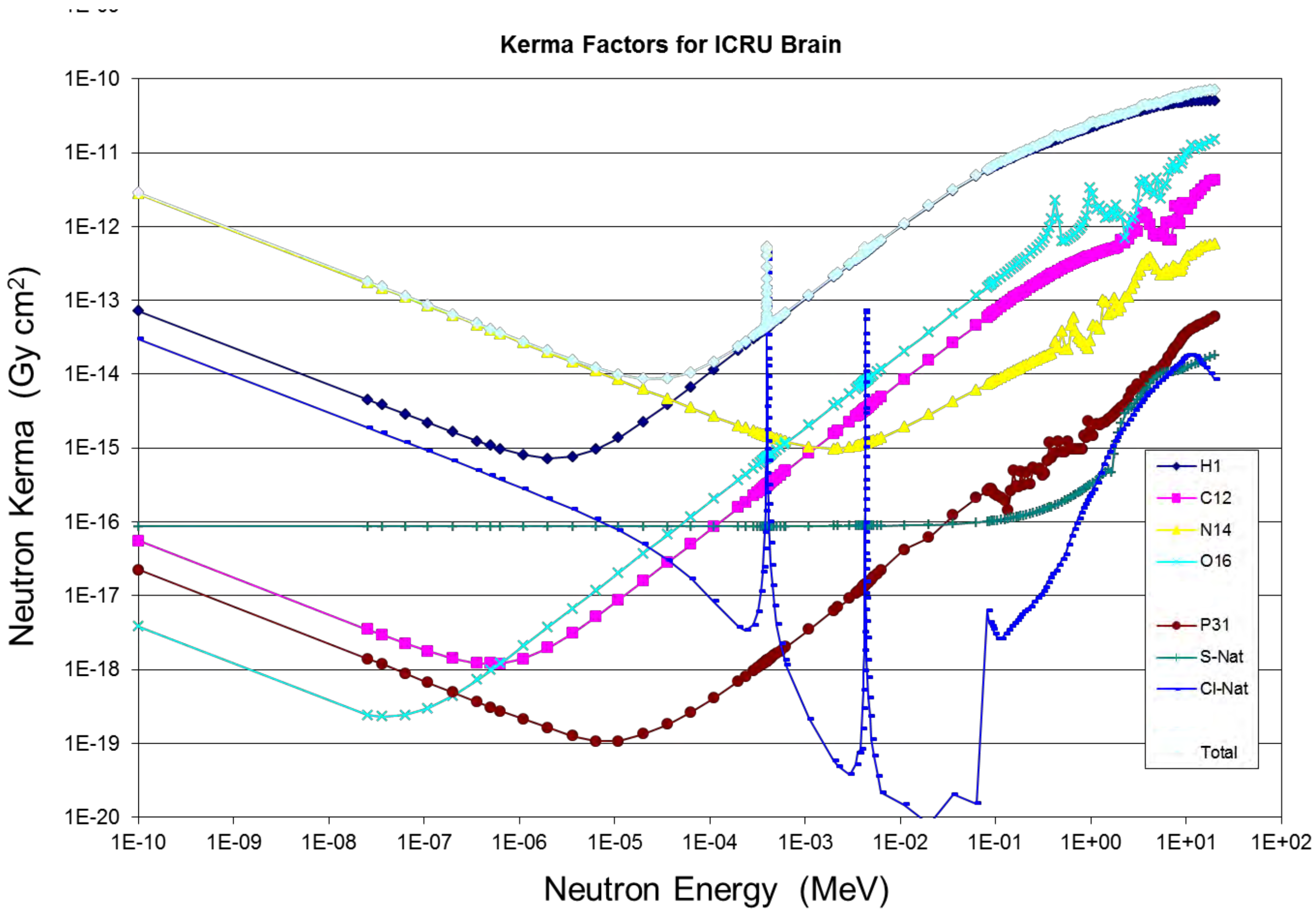

Figure 5.3 Fluence to dose kerma factors for ICRU Brain.

5.2 Tissue Equivalent Proportional counter measurements and analysis

The thermal neutron component of the mixed field BNCT dose is relatively easy to measure with foil activation techniques, as described in Chapter 4, and has uncertainties in the thermal component of the dose ~7%. But BNCT beam dosimetry is complex, standard methods (foils and ionisation chambers) result in assessment of the photon and fast neutron dose components with large uncertainties ~10 and 15% respectively [7].

Supplementary techniques have been used at the University of Birmingham to validate the standard methods. The supplementary methods employed included the use of A150 tissue equivalent proportional counter (TEPC) for the thermal and fast neutron dose components, a boronated TEPC for the boron dose component and Lithium 7 fluoride TLDs for the photon dose component at large depths in phantom (not discussed here).

A Far-West technologies tissue equivalent proportional detector (figure 5.4) & boronated [50μg/g] tissue equivalent detector were filled with propane based tissue equivalent gas to simulate a tissue sphere of 2μm diameter.

The detectors were irradiated at various depths in a 40(W)x40(H)x20(D)cm^3 large water tank in the Birmingham BNCT facility by Prof. S. Green and T. Ibrahimi [15]. Single event spectra were recorded at low beam current the analysis of which was was carried out by the author.

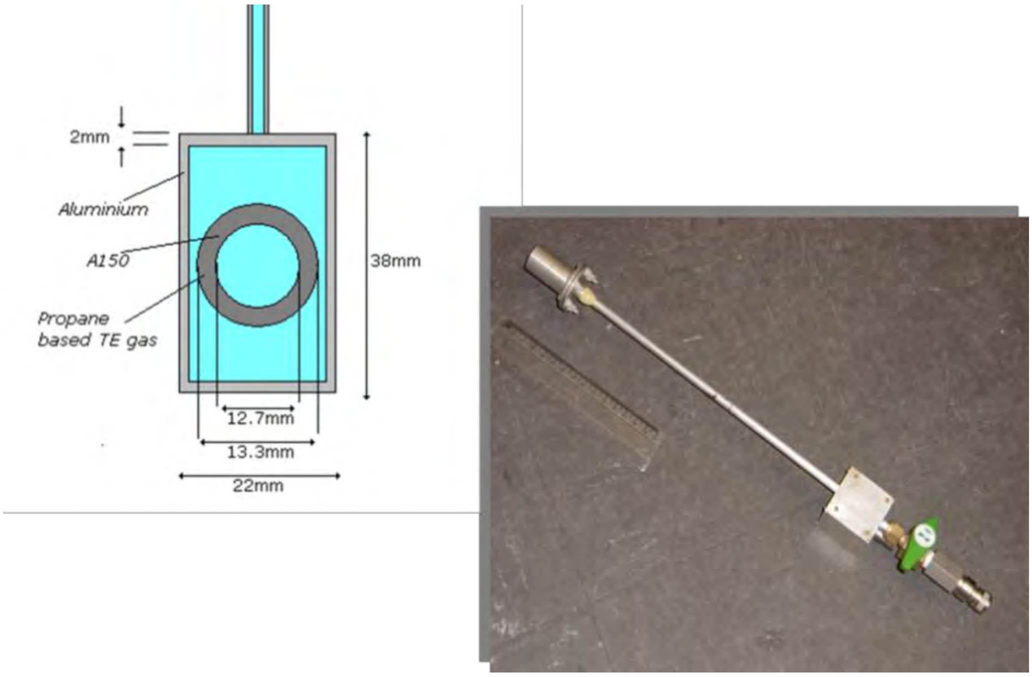

Figure 5.4 Schematic and picture of the Birmingham TEPC.

Benchmarking in-house software is extremely important when the results of such efforts can potentially impact beam shaping design and treatment planning calculations. With this in mind the pulse height distributions from proportinal counter measurements were analysed in Excel with spreadsheets benchmarked against NIST traceable Cf-252 source data measurements made by the US - Pacific Northwest National Laboratory (PNNL).

Results were processed in the Birmingham dosimetry spreadsheet and compared to results from the PNNL TEPC pulse-height analysis software Version 2.00R, using the same proton drop points and neutron start channels. The Birmingham spreadsheets and data processing show excellent agreement with the US national laboratory's derived photon and neutron dose rates, frequency mean and dose mean lineal energies, all derived parameters differing by less than 1%.

Lineal energy calibration is based on a distinct spectral feature, namely the proton edge, which is due to the fact that the maximum energy that any proton can deposit is approximately 95 keV/µm. The use of the proton edge feature provides a calibration, which is independent of any external standards, and as such can provide valuable comparison to the paired ionisation chamber technique [22].

For the Birmingham mixed field, neutron and gamma in phantom measurment, a proton drop point (edge) of 140keV/µm was taken from the PhD work of G. Taylor [16], which showed the stability of the edge at various neutron energies from 1 to 19MeV. For the boronated proportional counter an alpha 'edge' of of 372keV/µm was taken with a drop point at the midpoint of the falling edge due to its lower sensitivity to resolution effects [16].

5.2.1 DOSE SEPARATION AND KERMA CORRECTION

Monte Carlo simulations were carried out to determine the fraction of the total neutron dose, in the absence of boron, which contributes to the total (thermal + fast) neutron dose measured by the proportional counters and to see if it was separable into its component fractions by Monte Carlo calculations.

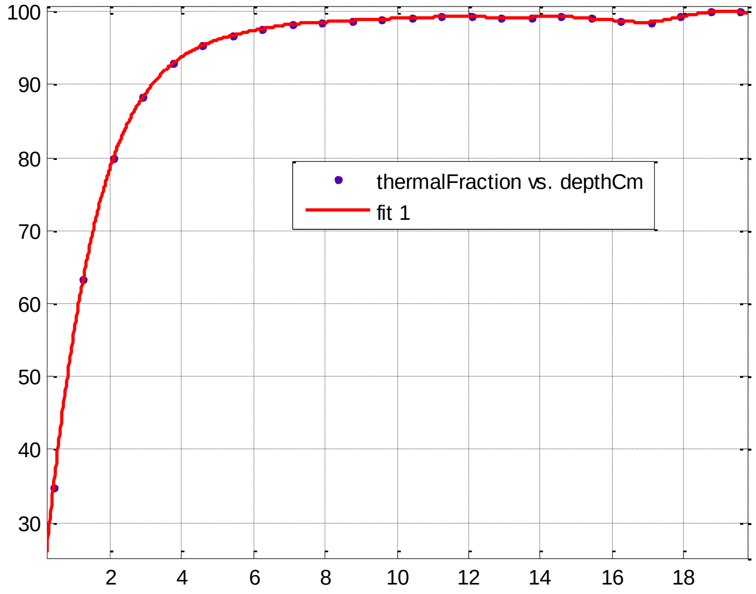

Figure 5.5 Thermal neutron percentage of absorbed dose in A150 tissue equivalent plastic, calculated in MCNPX (blue points) as a function of depth in a Large Water Tank. Interpolated in Matlab using a shape preserving spline (red line).

The TEPC walls are made of A150 tissue equivalent plastic, the filling gas also being tissue equivalent. Simulations were carried out using MCNPX to tally the flux at all depths, on the central axis, of a Large Water Tank exposed to a beam of epithermal neutrons from the Birmingham facility. The calculated fluence is multiplied by a fluence to dose kerma factor determined for A150 plastic calculated from elemental kerma factors [14].

Figure 5.5 shows the results of calculations, showing the fraction of the neutron dose which comes from the thermal neutron component. Results were tallied such that at upto 8cm there was approximately 6% statistical uncertainty in the calculated results and <5% at shallower depths. As is evident from the graph, by 2cm deep in the phantom, 80% of the physical dose (in A150) is from thermal neutrons, primarily being captured in nitrogen and releasing 630keV to the proton and recoil carbon ions. By 3.5cm this reaches a 90% fraction.

A MCNPX mesh dose tally along the axis was interpolated at the depths of the TEPC measurements using a cubic spline interpolant in Matlab. The measured thermal fraction is then corrected by calculated kerma correction factors, which recast the measurement from dose in A150 to dose in brain tissue as a function of depth in phantom [17]. A correction was also applied for the stopping power ratio for protons between detector wall and detector gas materials. Calculated Perurbation factors, by the presence of the TEPC in the field being measured, are less than 2% [17].

With proportional counter mesurements normalised to 1mA beam current and to a yield of 0.005 (i.e. Reference fission monitor chamber/integrated current) as per the foil activations and ion chamber measurements, corrected for brain:A150 kerma and dose fraction, the measured thermal results show excellent agreement with paired foil measurements and normalised MCNP simulations (figure 5.6).

The measured thermal neutron doses showing a maximum difference to that calculated of 15%, with an average difference of 7% from depths of approximately 3cm to 8cm.

The results here showing a primary passive measurement technique (foils activations) showing excellent agreement with a secondary (supplementary) technique (tissue equivalent proportional counter).

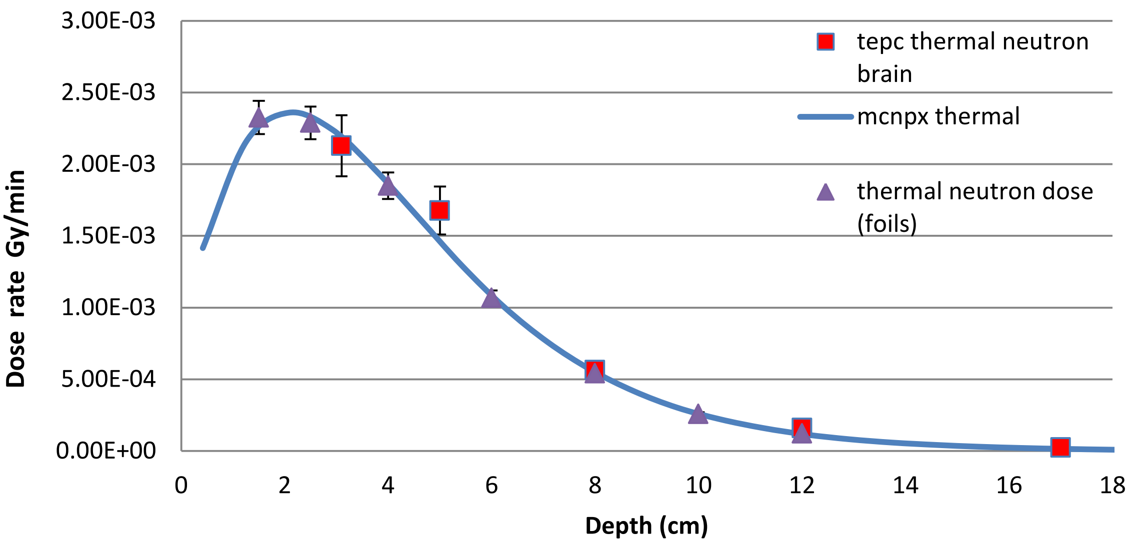

Figure 5.6 Thermal neutron dose [Gy/min] measured with a TEPC (red squares), with MCNPX calculated thermal dose (solid line) as a function of depth in a Large Water Tank. [Doses calculated from foil activation measurements shown as purple triangles].

Fast neutron doses derived from MCNP simulations compared with TEPC measurements from depths of 5cm to 17cm (figure 5.7) show large percentage differences due in part to the very steep dose gradient and positional uncertainty of the detector in phantom (highlighted in figure 5.7 by the horizontal error bars). Despite this relatively large uncertainy the results still showed greater consistency in both depth dose shape and less deviation from monte carlo simulations than did the paired ion chamber measurements over the same time period.

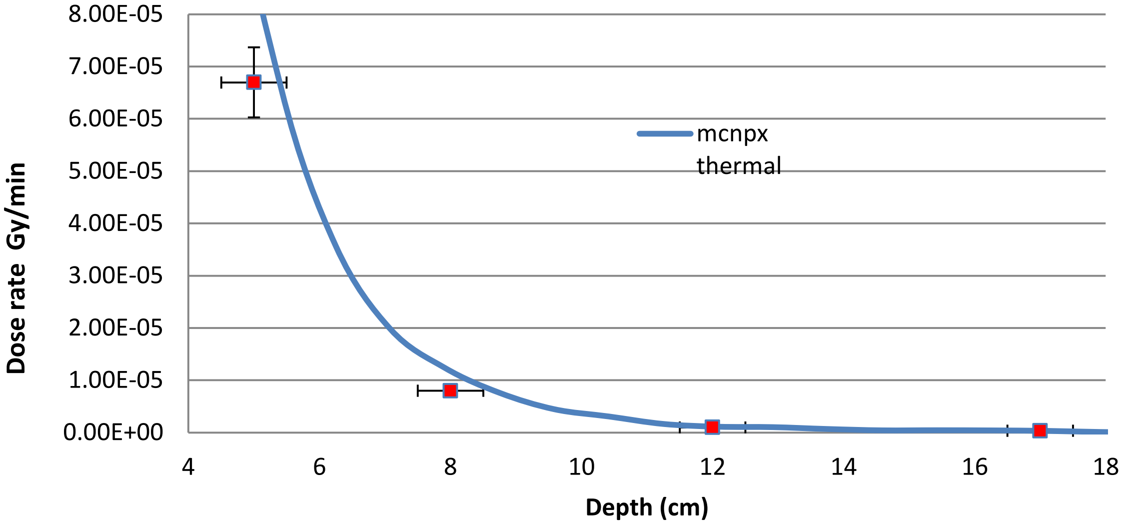

Figure 5.7 Fast neutron dose rate [Gy/min] measured with a TEPC (red squares), with MCNPX calculated fast dose rate (solid line) as a function of depth in a Large Water Tank.

The results of the Boronated TEPC measurements (figure 5.8) show the characteristic underestimate of dose component as has been noted by many BNCT groups around the world [42] and is most likely due to a combination of factors, including boron grain size, surface distribution of the grains in A150 and self shielding effects within the grain.

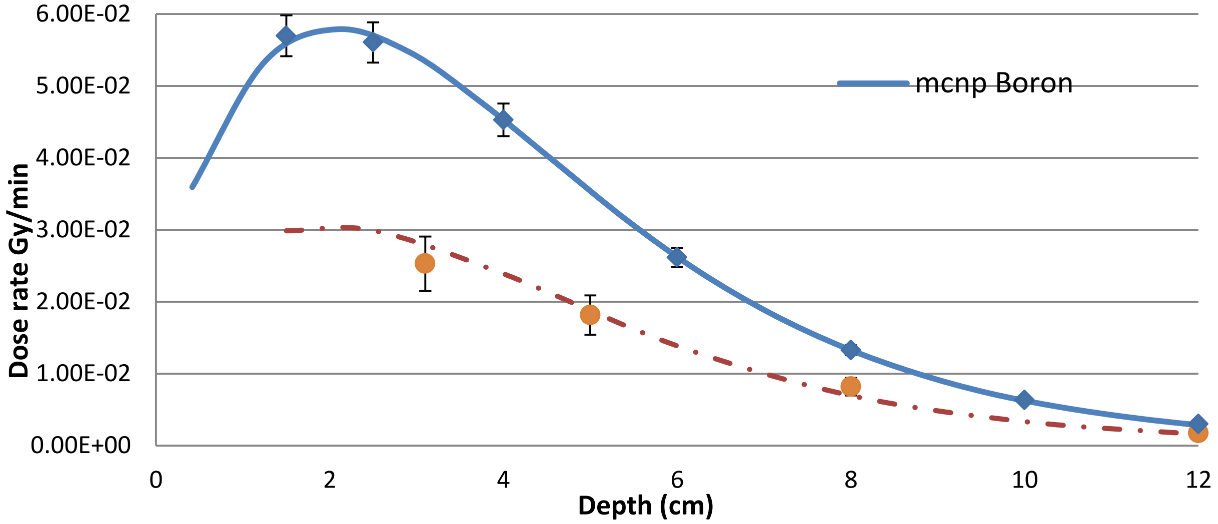

Figure 5.8 Boron dose [Gy/min] measured with a Boronated TEPC (50μg/g) (orange circles), with MCNPX calculated thermal dose (solid line) as a function of depth in a Large Water Tank. [doses calculated from foil activations shown as blue diamonds].

Independent supplementary methods are of very high value in the complex environment of BNCT beams. The TEPC technique outlined combined with MCNP is seen to be a valuable supplementary method for the measurement of thermal and fast neutron dose components.

5.2.2 Monitor Unit (MU)

Neutron beam intensity is monitored at the beam exit port with two U-235 fission chambers (D170, D164), these readings are used to provide a 'measure' of neutrons emitted in any given irradiation, called a Monitor Unit (MU). The D170 chamber, nominated the primary reference chamber, readings are used to measure dose to radiobiology experiments from reference dosimetric calibrations.

5.2.3 Normalisation

Having arrived at a physical Dose per Monitor Unit from the foil activations (for the nitrogen component), which is by far our most ‘certain’ measure, the other dose components for cell radiobiology work were deduced based on MCNP calculations. The normalisation process involved scaling the MCNP calculated nitrogen dose to that measured experimentally – the MCNP measurement requiring normalising to units of Gy/MU/s neutron and correcting for yield ‘anomalies’.

MCNP data was fitted to a ‘smooth’ fitted curve (4th order polynomial) by method of weighted least squares. The resulting fit was used to interpolate nitrogen dose to those depths measured experimentally. The experimental data was then scaled against the interpolated data points by a multiplying factor to arrive at a Chi squared (minimised) normalisation factor.

This calculated best fit is then used to scale the remaining MCNP dose components (by the same normalisation factor) thus providing physical doses in terms of beam MU for cell survival experiments.

Chapter 6

DOSIMETRY FOR CELL IRRADIATIONS AT MIT

6.1 The MIT Beam

Numerous radiobiology experiments have been carried out over the decades in the field of targeted ion therapy, using protons, carbon ions, alpha particles and other more exotic ion species. The University of Birmingham's BNCT group have focussed their radiobiology work on mixed field work (alphas and gamma rays) and dose/dose rate experiments in the fullest mixed field context of a clinically viable facility.

There is currently an inability of accelerator based neutron therapy facilities to match the magnitude of neutron flux generated from a reactor based neutron capture therapy facility. The consequence of which are lower dose rates and longer treatment times. A series of radiobiology experiments were conducted in the Fission Converter Beam, part of the MITR-II research reactor (figures 6.1, 6.2), to determine whether or not a dose rate effect exists in the delivery of Boron Neutron Capture Therapy and cell survival.

The MITR-II reactor was an ideal location for the testing of this possible dose rate effect. It is regarded as being one of the best therapeutic beams of its kind in the world and has the ability to control the dose rate being delivered by virtue of a converter control shutter (CCS) which has been shown to deliver a prescribed dose with beam profiles almost identical at high and low dose rate [18].

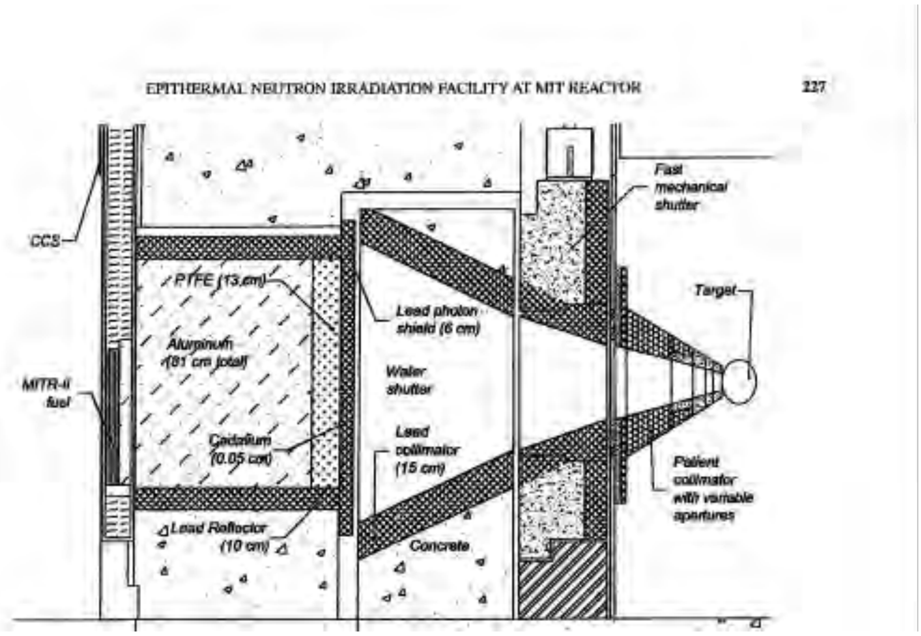

Figure 6.1 A schematic of the MIT Fission Converter Beam (FCB) beam shaping assembly.

With this in mind, a series of cell survival measurements were carried out using V79 Chinese hamster lung fibroblast cells at ~37ºC, irradiated at high and low dose rates. Several repeat measurements were carried out at each dose rate to improve the validity of the results [19].

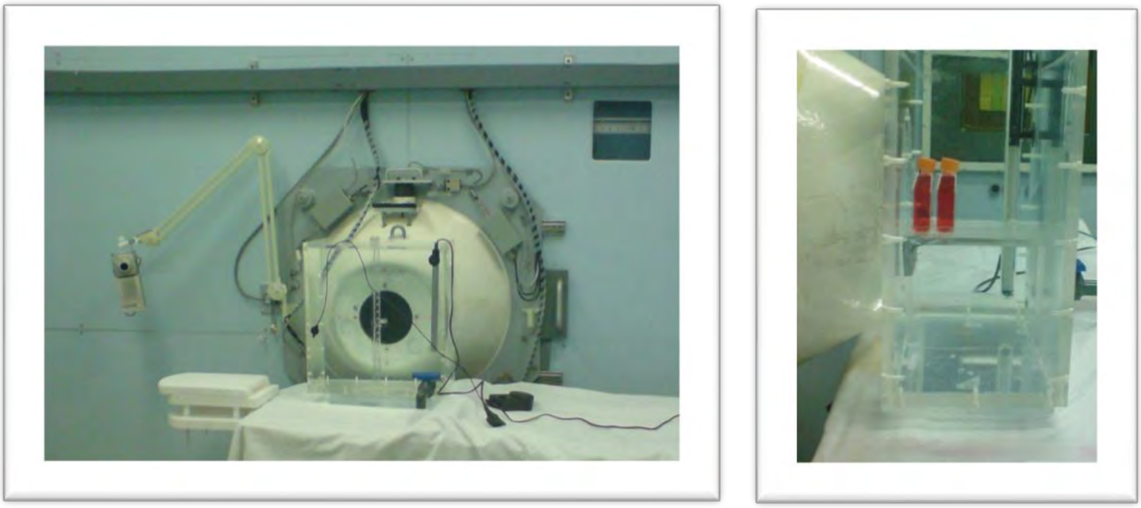

Figure 6.2 Images showing the Birmingham cell irradiation setup and geometry carried out at MIT.

Dilute manganese and gold foils (1% by weight) were activated via the (n,γ) capture reaction in the MIT epithermal beam at various depths in the University of Birmingham's reference phantom, a large Water Tank of 40x40x20cm^3. Irradiations and measurements were also carried out in the University of Birmingham's dynamitron accelerator beam line to help translate dose rate data measured in a reactor beam to one produced from an accelerator and be the benchmark for low dose rate epithermal irradiations.

In the Birmingham facility, foil activations, ion chamber and proportional counter measurements were used to quantify the thermal, photon and fast neutron dose components. At the MITR-II Foil activation measurements were carried out to determine the thermal neutron dose component from which the boron, fast neutron and photon dose components were to be inferred from existing reference measurements published by the MIT team [20] i.e. by interpolation and scaling.

6.2 Dosimetry via the cadmium difference method

Prior to irradiations the beam was calibrated and showed a count rate in fission channel 1 of 1826 cps at approximately 3.5MW, FC Power Monitor (ch. 2) read 23.7 to 24.1.

AuAl / MnAl foils were irradiated prior to the first cell irradiations at low flux to determine the subsequent dose and dose rate delivered to cells experiments, the paired foils were irradiated back to back in a foil pack at several depths in a standard large water tank (LWT) of 40x40x20cm^3. Due to the dilute nature of the foils the irradiation required extensive beam time to allow for the build up of enough activity in the foils to count with good statistics on a HpGe detector.

Further foil activations were carried out at high dose rate using AuAl/MnAl foil pairs, the opportunity also arose to carry out an alternative set of activations using a Cd covered set of dilute Au foils allowing the comparison of the Cd difference method, favoured by the MIT group [12], vs the Mn/Au foil pair technique favoured by Petten and other institutions.

All foils were counted on a HpGe detector, calibrated with a standard NIST calibration source [SRM 4275C] and counted to more than 10,000 counts in the photo-peak of interest (i.e. to better than 1% counting statistics). The photo-peak efficiency at the (nominal) reference foil detector distance of 22.5cm and its functional fit were provided by the MIT NAA laboratory was used to derive the gold and manganese photo-peak efficiencies.

Derived efficiencies and counts were used to calculate saturation activities and doses as per European Dosimetry Protocol [22].

Saturated activities per gram were calculated for all the foils irradiated. For the AuAl/MnAl foil pairs the Freudenreich method was used to derive the thermal neutron dose to nitrogen (3.4%) and for the cadmium difference foils the Rogus formalism [12] was followed to derive the same quantity, by first measuring the reaction rates in bare and cadmium covered foils and then calculating the 2200ms^{-1} flux as per equations 6.1 and 6.2. Calculated fluxes are then multiplied by fluence to dose kerma factors [12] for the nitrogen and boron reactions.

The dilute foils were 1% by weight active element, AuAl foils being ~62mg and MnAl foils ~57mg. The Cd covers used were ~1mm thick a F_{Cd} of 1.0 was assumed [22].

$$(R_{Au})_{Cd} = F_{Cd} \cdot \varphi_{epi} \cdot I_{Au} \tag{6.1}$$

$$\varphi_0 = [R_{Au} - F_{Cd}(R_{Au})_{Cd}]/\sigma_{0,Au} \tag{6.2}$$

Where,

$(R_{Au})_{Cd}$: Reaction rate measured in the cadmium covered gold foil.

F_{Cd}: Cadmium correction factor for absorption below the cut-off

φ_{epi}: Epithermal neutron fluence

I_{Au} : Gold foil Resonance Integral

φ_0 : 2200ms^{-1} fluence

R_{Au} : Reaction rate measured in the bare gold foil

$\sigma_{0,Au}$: 2200 ms^{-1} capture cross-section

6.3 Beam Linearity and scalability

Cell survival curves require a range of doses to be delivered i.e. given at the same dose rate but over varying lengths of time. With the ability to only irradiate two flasks at a time in the large water tank (i.e. two depths) without overly perturbing the flux and hence dose rate, a series of irradiations were carried out, delivering varying degrees of dose in order to build up a survival curve with repeat measurements being made at each stage to reduce cell survival uncertainties.

Figures 6.3. shows the reproducibility and linearity in achieving the ‘same’ dose rate between various experimental runs at the MIT-FCB. All points lie in extremely good proximity, (better than 2%) to the average fluence rate (measured by fission chambers) (fitted line) in figure 6.3. The saturated foil activities as measured in the high and low flux dosimetry runs between cell irradiations, figure 6.4, also show the excellent scalability of the MIT neutron flux as a function of depth for two foils of differing neutron spectral sensitivity. Hence demonstrating the reproducibility of the neutron spectrum and dose mix at high and low dose rates.

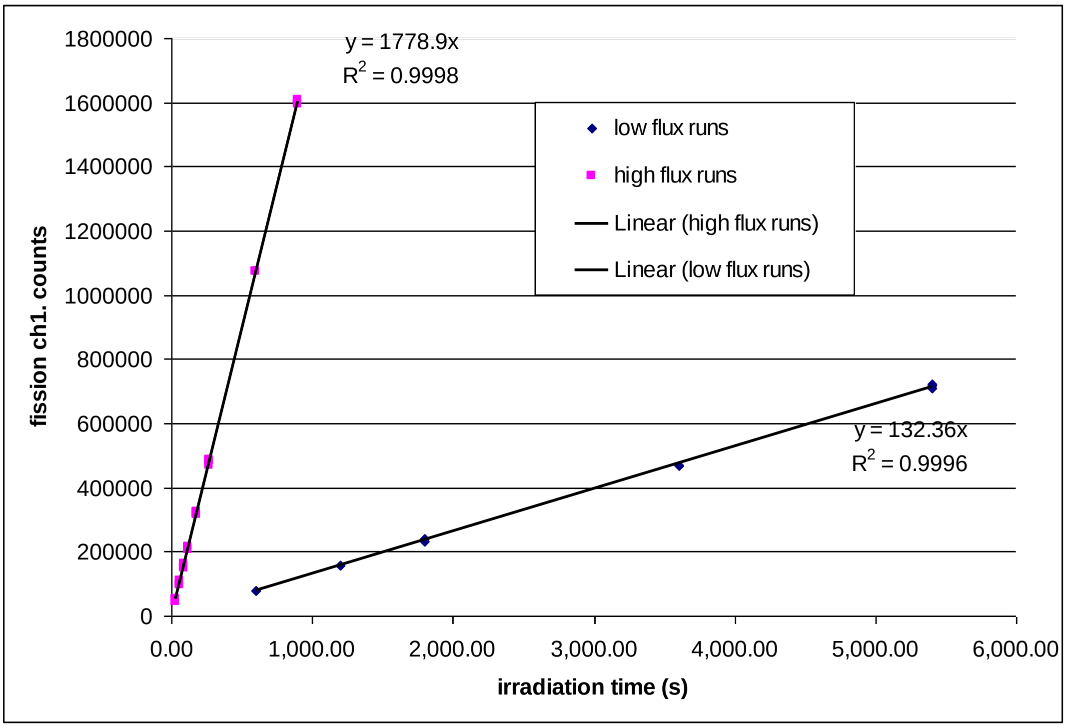

Figure 6.3. Showing linearity of low and high dose rates for cell and foil measurements over various dose end points. NB Fission chamber/channel 1 was taken as the primary beam monitor.

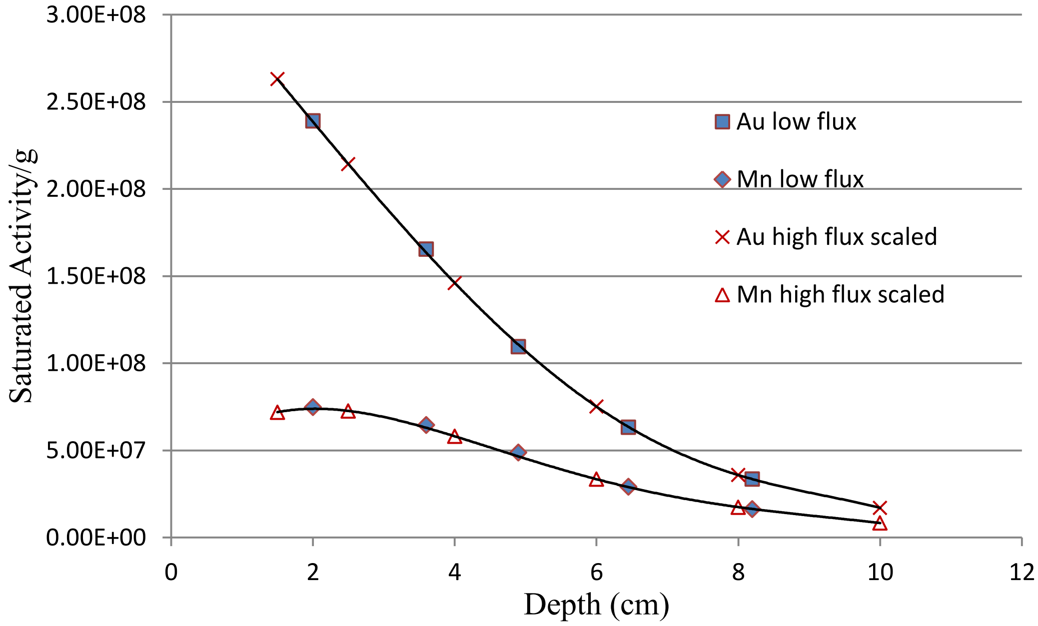

Figure 6.4 Measured saturated activites in gold and manganese foils at low and high dose rate dosimetry runs. [red lines represent high dose rate run, black lines represent low dose rate runs].

A total of 38 irradiations were carried out at the MIT research reactor. Four of these being conventional dosimetry runs measuring depth dose curves using foil activations, with:

1. Six AuAl/MnAl foil pairs at low dose rate.

2. Six AuAl foils at high dose rate.

3. Six MnAl foils at high dose rate.

4. Five Cd covered AuAl foils at high dose rate.

Two sets of measurements were carried out to assess the effects of boronated medium in the flasks and to what extent it perturbs the dose to the second of the irradiated flasks:

1. Four dilute foil pairs, attached to the front and back of each flask, with Boronated medium.

2. Four dilute foil pairs, attached to the front and back of each flask, without Boronated medium.

The remainder of the irradiations were used for cell survival experiments to build survival curves at high and low dose rate. MIT reference measurements were provided for comparison and scaling [20]. These were conducted in a large water tank, 40x40x45cm^3 (inner dimensions), which is deeper than the phantom used in the current measurements and of greater wall thickness (1cm wall thickness as opposed to our 0.5cm entrance window).

6.4 Measured dose comparison

The measured thermal neutron dose to 3.4% nitrogen [as per MIT's reference dosimetry report] in the beam using both the Freudenreich method and the Cd difference method can be seen in figure 6.5. The two methods share common measured data for the AuAl (dilute foil) in combination with the necessary measurement of Saturated Activity for the MnAl foil irradiation and Cd covered AuAl foil irradiation. The Cd covered foils were given a minimal of 2cm separation as suggested by Rogus [12], with no FCd correction applied (i.e. F_{Cd}=1.0) as opposed to the 1.02 factor applied by MIT for their thinner Cd covers (0.5mm thick).

For the Cd difference method a kerma factor of 7.86E-14 Gy cm^2/n was used [12] and for the Freudenreich Spectral indices method [9] the parameters as per the EU protocol [22] were used. The measurements were done at high dose rate, with both the Cd difference method and the Freudenreich method showing excellent agreement, well within the uncertainty bounds associated with the measurement (Figure 6.5).

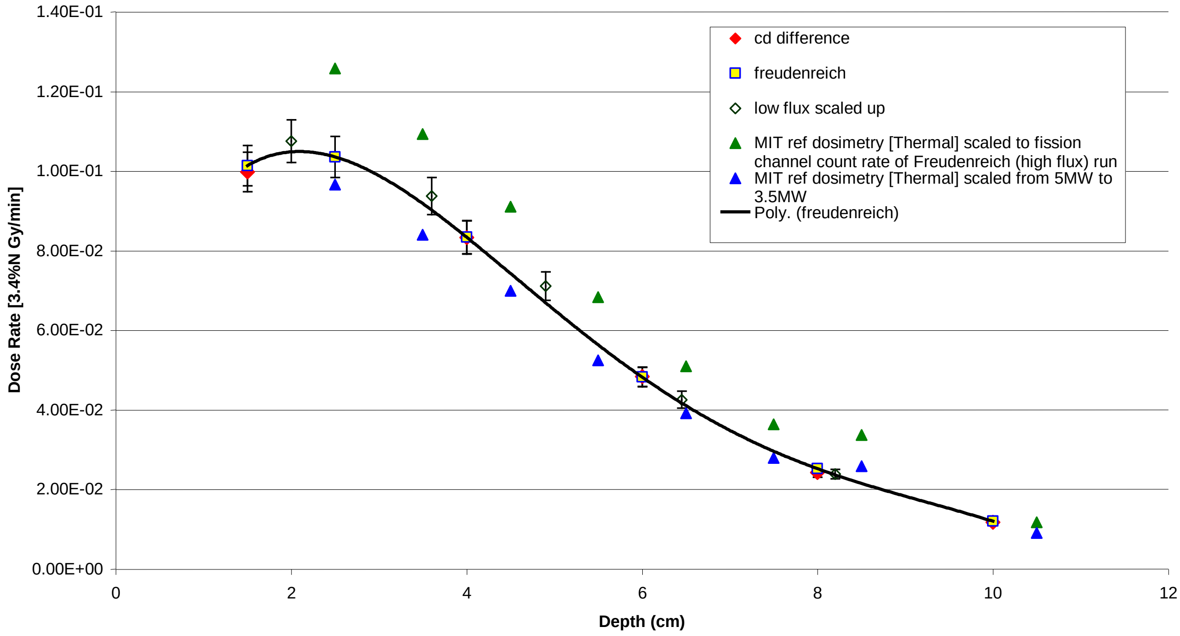

Figure 6.5 Summary of measured thermal dose to 3.4% nitrogen carried out in the MIT beam using the AuAl/MnAl foil pairs at high and low dose rate, along with the Cd difference method at high dose rate only. The MIT reference data is shown normalized to 3.5MW and to 18000cps.

The low flux to high flux dosimetric measurements are scaled by the ratio of the fission chamber count rate [channel 1] between the high and low flux runs. Two forms of normalisation have been applied to the MIT reference data shown,

- The MIT data was scaled from the 5MW reactor power they were quoted at to 3.5MW power at which the Cell and foil measurements were done.
- The MIT data was scaled to the fission chamber count rate (channel 1) at which the current foil measurements were carried out, i.e. 1778 cps from the 5MW to 1951 cps of the reference measurements.

As can be seen from Figure 6.5, the measured data falls between two alternative scaling methods. This was explained by the MIT group to be most likely due to a change in the beam line since their reference measurements were carried out.

The low flux boron dose rate compares well with the boron depth dose curve simulated for University of Birmingham based accelerator facility and compares to a ~2mA proton beam onto a natural lithium target (figure 6.6).

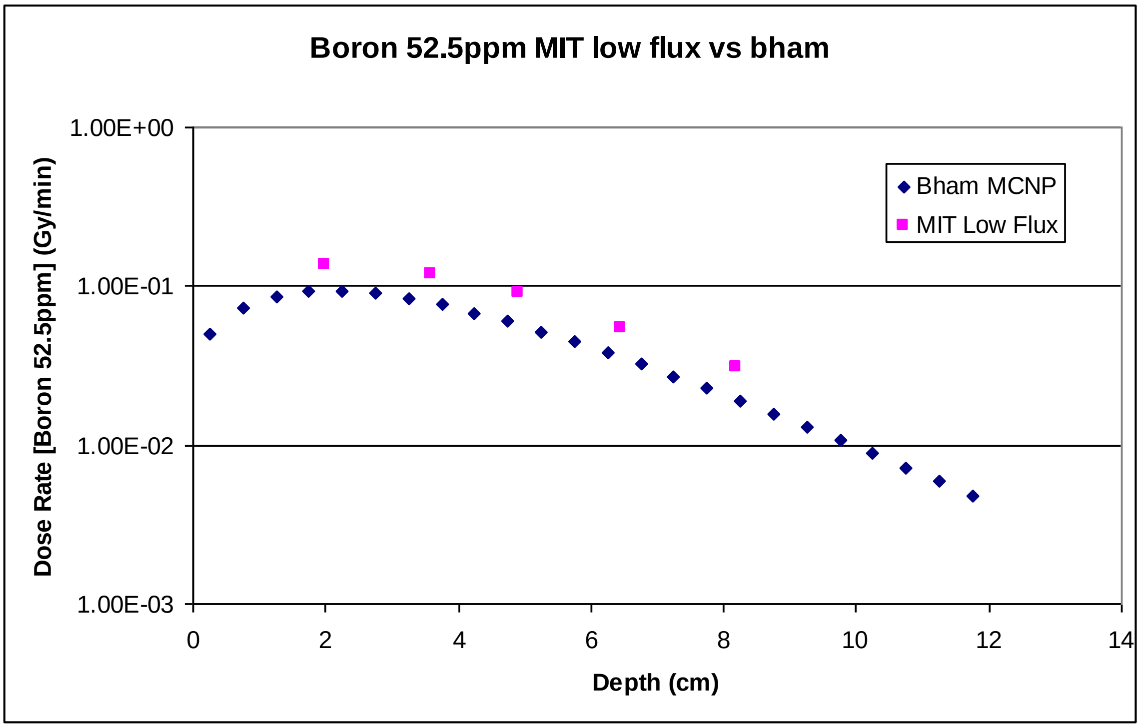

Figure 6.6 Comparison of the boron low dose rate boron measurement at MIT with MCNP calculations of maximum dose rate in the Birmingham beam i.e. at 1mA beam current.

6.5. Flask dose corrections

The flasks in which the V79 cells were irradiated occupy a finite profile in the beam. This necessitates a correction for the drop off in the dose components across the beam central axis and hence the flask, which changes with depth for each dose component. These dose correction factors are loosely termed off-axis correction factors. MCNPX was used to calculate these off-axis correction factors for the Birmingham beam, a planar section at the two irradiation depths can be seen in figures 6.7 and 6.8 showing the fall off in neutron flux perpendicular to the beam exit direction; a flask area (rectangle) is superimposed over the mesh tallies in Figure 6.7 illustrating the profile of a typical flask and the cells grown in it.
As well as off-axis dose corrections, the flasks also perturb the flux that passes through them by virtue of the medium being loaded with 50µg/g of boron.

Perturbation factors were calculated for the Birmingham beam using MCNPX. Figure 6.9 shows the perturbation calculated for the flask monolayer, 1mm deep under the front face of the flask (where the cells are fixed), at the two depths at which irradiations were carried out. The second flask is evidently much more perturbed than the first, with thermal neutron perturbations reaching upto 15% at the centre of the front surface of the flask.

MNCP input decks were not available for the MIT Fission Converter Beam and off-axis correction factors were calculated from interpolated off-axis foil and ion chamber measurements for the fast, thermal neutron and photon components of the beam. Matlab was used to interpolate the dose components, assuming they have off-axis rotational symmetry, and then numerically evaluate the double integral over the planar region occupied by the flasks. Dose corrections for the off-axis profiles for thermal, fast and photon components were, 0.97, 0.98 and 1.18 respectively. Flux perturbation factors were applied as per the Birmingham beam.

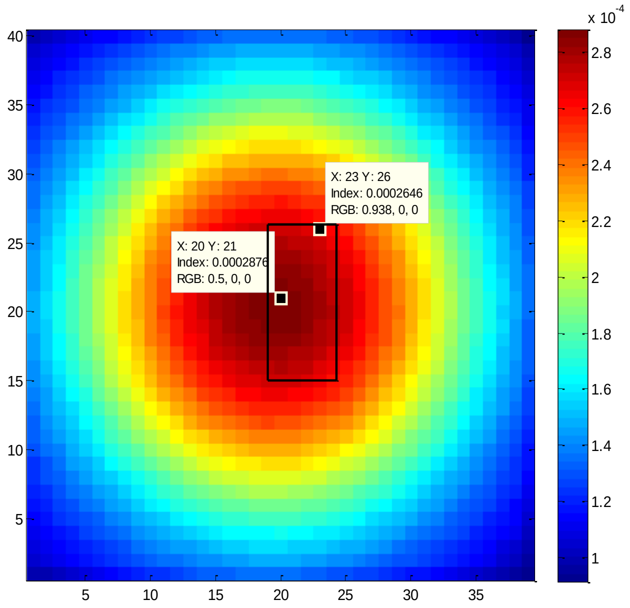

Figure 6.7 Surface plot of the off-axis thermal flux in large water tank in the absense of flask, Dose profile across flask surface

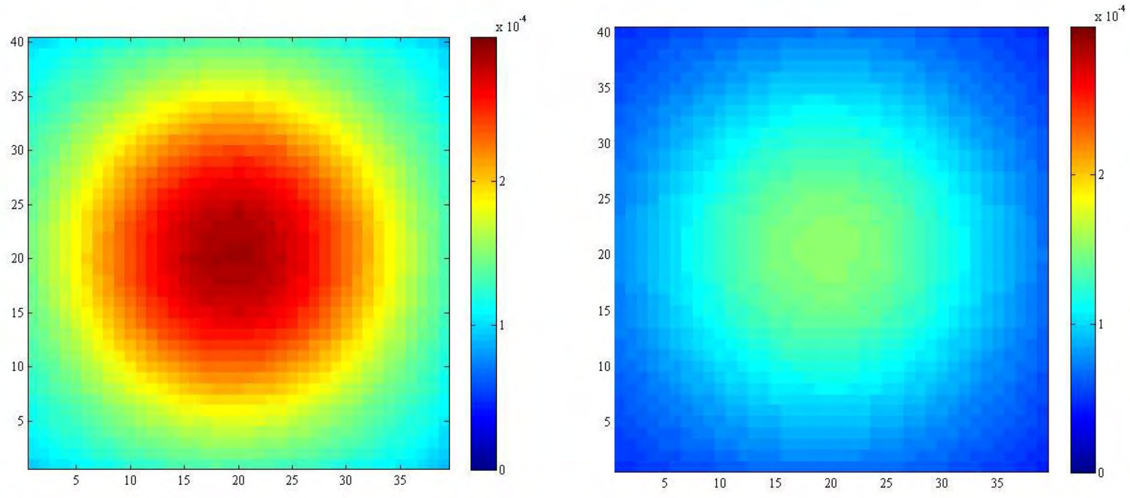

Figure 6.8 Thermal neutron flux at 2.25cm (left) and 5.25cm (right) [axes are in units of voxels, 0.5mm x 0.5mm x 0.5mm]

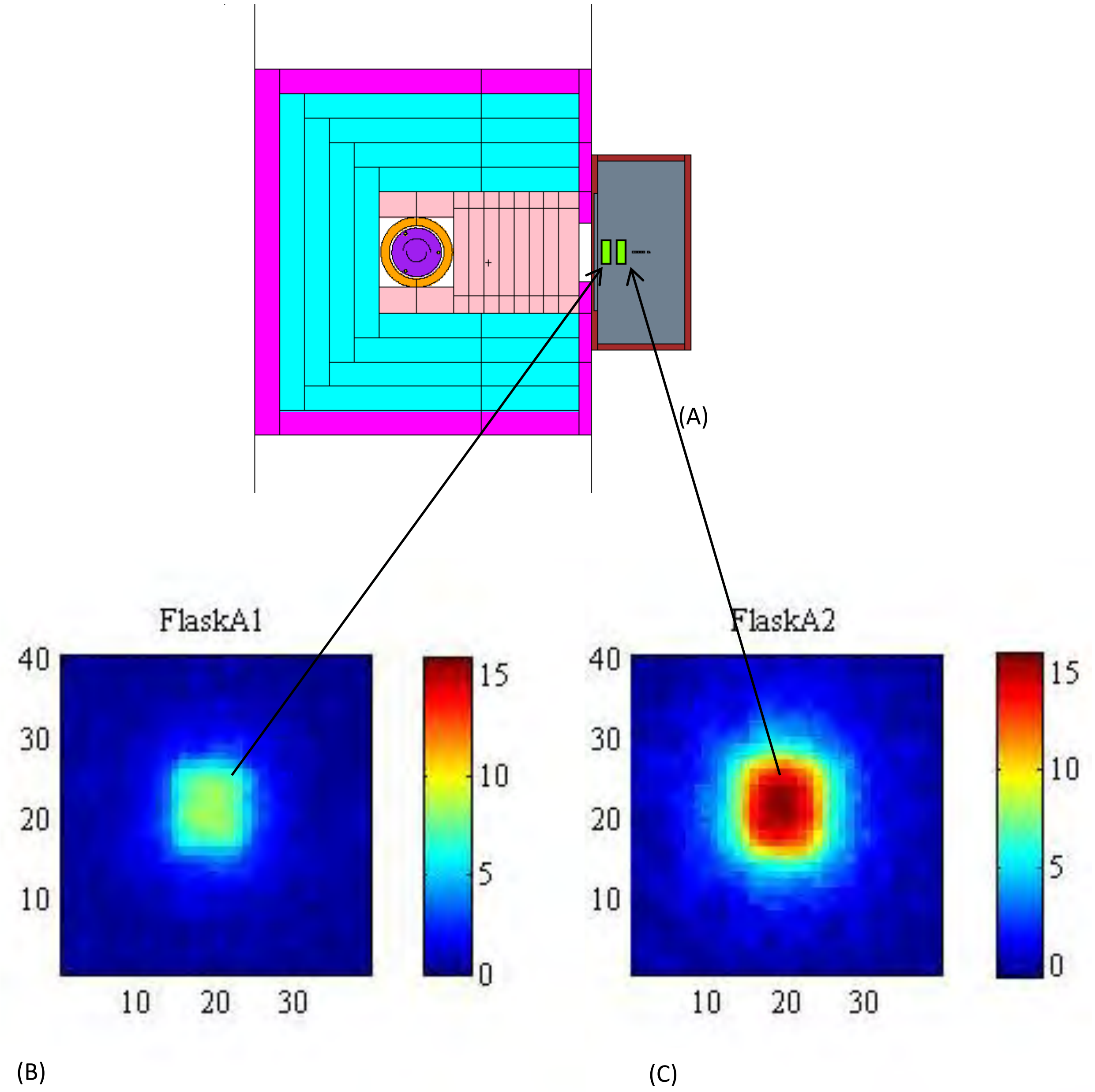

Figure 6.9 The xis for the cells in the geometry show er Tank (grey) and flasks (green). Percentage Perturbation factors for the shallow flask (B) and flask at depth (C).

Table 6.1 shows the calculated combined off-axis perturbation correction factors for the flasks at 2cm and 5cm deep in phantom. The 'flaskn' heading refers to the dose in an unperturbed medium i.e. in the absence of the flasks and 'flaska' refers to the dose in the presence of the flasks. Corrections range from -6% in the case of photons to 15% in the case of thermal neutrons.

	Boron [Gy/min]	rel. uncert.	Thermal [Gy/min]	rel. uncert.	Fast [Gy/min]	rel. uncert.	Photon [Gy/min]	rel. uncert.
flaska 2cm	8.01E-02	0.0006	3.27E-03	0.0006	1.04E-03	0.0019	2.73E-02	0.0006
flaskn 2cm	8.57E-02	0.0006	3.50E-03	0.0006	1.10E-03	0.0018	2.57E-02	0.0006
ratio	**1.07**		**1.07**		**1.05**		**0.94**	
flaska 5cm	4.19E-02	0.0008	1.73E-03	0.0008	9.13E-05	0.0059	2.16E-02	0.0006
flaskn 5cm	4.82E-02	0.0007	1.99E-03	0.0007	1.02E-04	0.0056	2.09E-02	0.0006
ratio	**1.15**		**1.15**		**1.12**		**0.97**	

Table 6.1 perturbation corrections for the Birmingham beam.

Chapter 7

MICRODOSIMETRIC CONSIDERATIONS IN APPLYING BNCT TO CELL RADIOBIOLOGY

7.1. Overview

The following chapters quantify and expound upon the difference in physical boron dose absorbed by V79 Chinese hamster lung fibroblast cells when incubated in boric acid and irradiated in different clustering models. Two configurations were investigated, (i) cells grown as monolayers directly onto mylar [figure 7.1(a)] (ii) cells grown and irradiated in suspension [figure 7.1(b)]. In the case of monolayers, the boron loading of the medium surrounding the cells is limited to a 3-D half plane of uniform distribution centred/bounded on the cell mylar interface, whereas in the case of a cell suspension the boron loading is much more uniform, surrounding each and every cell.

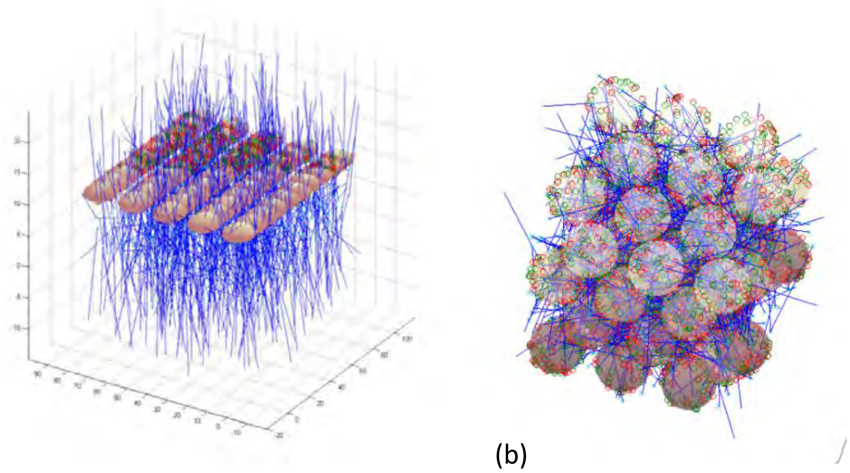

(a) (b)

Figure 7.1. Plot showing particle track simulations in a cell monolayer (a) and cell suspension (b) for oblate ellipsoids and spheroids, respectively.

Monte Carlo methods were employed to simulate lithium ions and alpha particle tracks in semi-stochastic geometries representative of cell monolayer and suspension irradiations, incubated in a medium with 50µg/g boric acid.

Monolayers of cells were generated with realistic morphologies. Cell nuclear sizes were randomly sampled from frequency/area spread functions from confocal imaging work. Cell suspensions were simulated such that cell bodies were taken to be spheres tightly packed in a hexagonal cubic centred array with spherical nuclei of 4µm radius.

Particle tracks were simulated as line segments with variable Linear Energy Transfer (LET) representative of the physical ions. Using the calculated chord lengths and track averaged LETs of the particle, for any given traversal of the cell nucleus, the equivalent „specific lethal dose‟ [23] was found from track segment irradiations. This was then used to calculate the probability of the cell surviving any given passage. The product of all cell passages allow the probability of single cell survival to be calculated and averaging over the population allows population survival curves to be determined.

Calculations were carried out for both monolayers and suspensions over a range of doses leading to markedly different survival curves. For the same given macroscopic fluence of alpha particles and lithium ions, monolayer cells see a reduction in dose compared to the identical cell line grown in suspension. This is due to two main factors, one being the inhomogeneity caused by growing the cells on the medium boundary (the mylar base/wall) – which has no boron beyond it, the other being the observable difference in cell morphology between suspended and monolayer cells and their nuclei.

Experiments were carried out to confirm these findings; monolayer cells were grown on modified dishes to deliver a more uniform boron distribution. The results of irradiating cells, in this homogeneous field resulted in a reduction of cell survival for the same irradiating fluence, corresponding to a reduction of cell survival for the predictable dose increase.

This microscopic dose effect needs to be carefully considered when extrapolating radiobiology data, derived from idealistic monolayer irradiations, to realistic in vivo scenarios.

7.1.1 Stochastic events

The primary intended dose, the basis of neutron capture therapy, is stochastic in nature, discrete capture of neutrons by the high thermal neutron capture cross section isotope Boron-10. The Li ion and alpha particle liberated in the decay of Boron-10 have a combined range of 13-15µm in medium, calculated using the radiation transport code SRIM [5]. These light ions have an average LET of ~200keV/um [43].

In a bulk medium loaded with boron, irradiated with a thermal neutron beam, the greatest part of the dose deposited, 86% - 89.8% is formed by the alpha decay of Boron-11 following neutron capture. This „boron‟ dose is unlike the photon field carried from the source or emitted in the interactions of neutrons with hydrogen by neutron capture reactions, it is observed to be „stochastic‟ following a random (Poisson) distribution [figure 7.2] in any microscopic volume. Whereas, the photon field, liberating many hundreds of electrons per Gray [24] on the cell scale of events, is much more uniformly distributed.

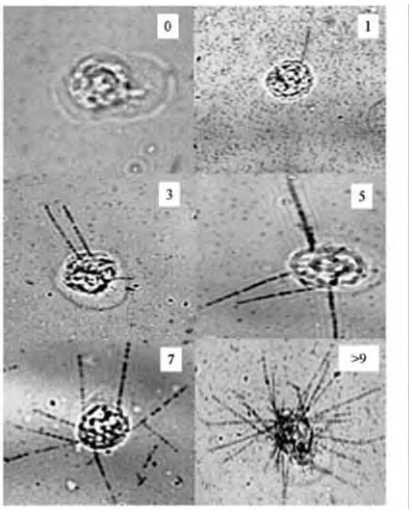

Figure 7.2 Autoradiographs, demonstrating stochastic event distributions seen in cells incubated in 210Po-citrate alpha-emitter [25].

In a typical treatment, for example at the MIT fission converter beam, a patient is treated with a maximal weighted dose of 12.5Gy to healthy tissue would see a fluence of ~10^{12} neutrons, with such a fluence and assuming a boron loading of ~10^{9} atoms per cell, we would have ~3 reactions per cell. A cell population exposed to such a fluence would only see a Poisson distribution of these collective events with a mean of 3 events per cell. With such a random distribution 42.3% of cells on average see less than 3 events per cell and 4.98% of cells see no events at all.

There are numerous factors which complicate the calculation of dose in small, cell like, volumes including, the thermalisation of the impinging epithermal beam and its subsequent spectral shift and the fall off in fluence with depth i.e a fluence/dose rate shift. This results in a non-uniform distribution of neutron fluence and spectra across the cell monolayer and even more so in cell suspension as the monolayer is always perpendicular to the beam and only a few microns thick, although in off-axis terms it sees a greater fall in fluence than cell suspensions, which are often irradiated in small vials.

7.1.2 NON charged particle equilibrium

To compound the changing fluence and spectra, there are numerous neutron interactions of the incident beam in its journey to the patient/target of interest, generating a cascade of light ions, gamma rays and secondary charged particles which are liberated in human tissue as a result of the nuclear interactions of neutrons with matter, leading to a directionally sensitive release/deposition of kinetic energy, mediated by light ions, electrons and delta rays. The resulting dis-equilibrium between dose and kerma warrants great caution when calculating dose to cell monolayers and a simple kerma approximation will not do. Figure 7.3 illustrates this lack of charge particle equillibrium as seen by two spherical nuclei in an inhomogeneous distribution of alpha particles.

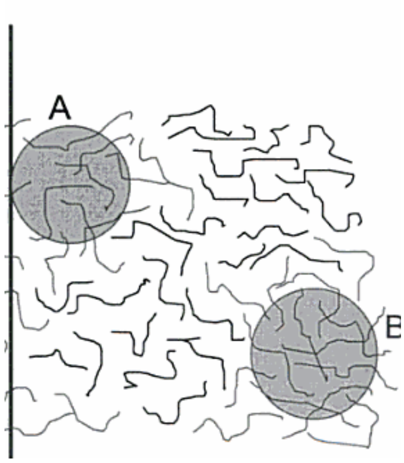

Figure 7.3 Graphic illustrating the absence of charged particle equillibrium, of alpha particles, as a cell nucleus approaches a boundary.

Due to the complex nature of the mixed field fundamental calculations must be carried out before any attempt is made to convolute doses from the various reactions which contribute to the total dose, the resulting particulate radiations of which have very different track structures and ranges in matter.

Also, of great importance is the case in which monolayer cells are grown on flask surfaces, immersed in boronated medium and irradiated from a collimated beam in a fixed, reproducible geometry.

The two major dose inhomogeneities seen in the mixed field of a BNCT beam when applied to boron loaded cell monolayers as opposed to cell clusters/spheroids/suspensions are the boron dose and the thermal neutron dose resulting from the interaction with the high cross section common elements in the body, nitrogen and hydrogen.

Cells are typically grown on a thin Mylar film on the polyethylene flask wall and on the other interface is medium containing in our case boric acid [19]. Using tabulated elemental kerma factors one can calculate the relative kerma factors for each material of interest and when multiplied by measured (neutron) particle fluences can yield macroscopic estimates of dose. But these kerma factors alone are not sufficient to calculate the dose distribution seen by the cells in inhomogeneous target material distributions.

The primary cause for the dose inhomogeneity and the non-charged particle equilibrium is the non-uniform distribution of these elements across the cell monolayer and its two adjoining interfaces. The remainder of this chapter will discuss the boron dose in more detail and chapter 8 the nitrogen dose.

7.1.3 The boron dose

Of critical importance in calculating localised dose delivery and cell death, is the loci of boron atoms and as to whether there is a predictable/measureable bio distribution of the boron carrying pharmaceutical between nuclear, cellular and extra cellular biological compartments.

Capala et al. [4] employed an oil filtration method to rapidly and reliably determine the boron concentration ratio between cells (intracellular) and their growth medium in a variety of boron loaded drugs and cells so as to distinguish promising pharmaceutical drugs in vitro. They found that GS-9L rat gliosarcoma cells incubated in boric acid had a linear (proportional) relationship between boron concentration in medium and boron concentration in cells, and was in fact equal (unity) over the entire range of boric acid concentrations used, [10 to 75µg/g]. Thus allowing the authors to ascertain intracellular and extracellular boron levels based on the gradient of the curve. Ratios of 0.96±0.8 and 1.5±0.11 were observed for U-343MGa human malignant glioma and B16 mouse melanoma respectively, i.e. a ratio of 1.8±0.16. The same tumorigenic Cell lines acquired BPA in very different uptake ratios primarily due to active transport of the essential amino acid, phenylalanine, as opposed to the passive diffusion in the case of boric acid. Accumulation ratios (relative to boric acid uptake) were 3.2±0.39, 1.3±0.07 and 1.6± 0.22 respectively.

Chung [26], developed an in vitro assay to determine the radiobiological effectiveness of novel pharmaceutical for the delivery of boron to tumour cells of interest. Thus developing a method for „compound screening", which allowed a model, which by virtue of cell survival/CBE, can be used to differentiate those compounds which have promising intracellular uptake ratios from those that have not. Squamous cell carcinoma, Murine SCCVII, cells (murine models of head and neck cancer) were incubated with porphyrins (BOPP) and liposomal boron carriers but neither showed any, in vitro, therapeutic advantage over BPA.

The experimental radiobiological methods employed by Chung. are similar to the irradiations carried out at MIT and Birmingham by Phoenix [19], but using a different cell line. Briefly, SCCVII mouse squamous cell carcinoma cells, are irradiated in a „shielded box" at the end of the MITR-II 5MW research reactor, which can produce a peak thermal neutron flux of 5x10^9 n/cm^2s^{-1}. For clonogenic assays, cells are grown (cultured) on the bottom of T12.5 cell culture flasks, the flasks are surrounded by neutron scattering materials (acrylic) to maximise flux to cells. Flasks are irradiated in pairs. Macroscopic dosimetry is carried out using gold foils, (bare and cadmium-covered) and reference paired ionisation chamber technique. Foils were placed at several positions along the bottom of the flask and the measurements averaged to garner the true flux. This allows for the determination of the thermal neutron, boron (from foils and kerma factors), fast and photon dose components were measured using ion chambers placed near the bottom of the flasks (closest to the cell layer). A schematic of the MIT thermal irradiation setup can be seen in figure 7.4.

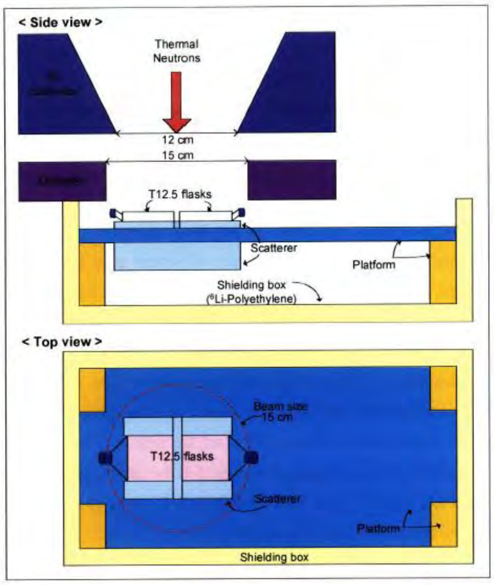

Figure 7.4 Schematic view of the set-up for cell irradiations carried out at the MITR-II reactor by Chung [26].

The thermal beam line in the reactor is of vertical geometry and cells were positioned such that the attached cell layer on the flasks was on the surface furthest from the beam, and minimal growth medium and thus pharmaceutical was required to incubate/nourish the cells (1ml of medium).

Fission counters are used to monitor the beam during any given cell irradiation, these monitors allowed dose to be delivered to the irradiation facility with a precision of 1% with dosimetric uncertainties of 5% for thermal neutrons and photons and 7% for boron.

A comprehensive uncertainty analysis was conducted by Chung, leading to an uncertainty in CBE of 10-20%. The reported methodology does not however fully account for the dose inhomogeneity at the cell/flask interface, which must have led to large systematic uncertainties in dose quantification – specifically relating to the Boron dose component, which inevitably puts a greater uncertainty in the CBE factors if they are not explicitly calculated.

Davis et al [43] addressed the problematic dosimetry and derived RBEs from earlier, pre 1970s, works which failed to address the concept of absorbed fraction and inhomogeneity in boron distribution. His work, carried out on the MITR beam, specifically addressed the calculation of accurate absorbed doses in HeLa cells grown in monolayers. HeLa cells were grown in Falcon plastic flasks, incubated with various concentrations of boron and irradiated in the MITR reactor. Colony assays were grown and survival calculated.

Work was carried out to determine boron uptake (from boric acid). Before irradiations, the medium containing the boron was removed from the flasks, for only the period of irradiation, and was then returned to the flasks to complete the survival assay. The removal of medium thus allowed the authors to confine the dose to the cells and cell nucleus from the component due to boron that was contained in the medium surrounding every cell.

Reference dosimetric methods used to quantify the macroscopic dose components were gold foils, tissue equivalent ion chambers, TLD-700 lithium fluoride thermoluminescent powder and silicon diode.

The concept of absorbed dose fraction from work with internal emitters was extrapolated to calculate absorbed doses from the ^{10}B reaction. In the work of Davis et al. [43], the absorbed dose fraction for boron distributed intracellularly was calculated to be 0.5 i.e. a nominal figure between the 0.611, calculated for spheres, and 0.35 calculated for cylindrical discs. This allowed the author to separate the ^{10}B dose from the other components and hence calculate RBE values for the densely ionising lithium / alpha reaction, being 3.7+-0.2. The author did not try to calculate the absorbed dose fraction for uniform distributions.

Boron distribution inhomogeneities in BNCT are often accounted for by radiobiological weighting factors, called the Compound Biological Effectiveness (CBE). The CBE is a product of the boron Relative Biological Effectiveness (RBE) and a factor which accounts for the boron micro-distribution. For boric acid the distribution is uniform, thus the CBE often used in presenting weighted doses is 2.3 [27]. This quantity doesn"t convey any information about the geometrical inhomogeneities encountered in monolayer irradiations.

Calculating the correct physical dose is absolutely essential in assessing damage to critical biological structures and their survival probabilities during cell irradiations. It is the only meaningful way that data can be used to make inference to human studies. It is also the essence of the fundamental radiobiology work, underpinning translational studies in introducing this novel treatment modality into clinical radiotherapy.

Thus, much effort has been expended in this thesis to studying dose distributions in the presence of inhomogeneous boundary conditions in cell culture irradiations. In doing so, the methodology of Davis has been adopted in using the quantitiy „absorbed dose fraction‟ and defining absorbed dose in the current work as the fraction of energy per unit mass emitted from the source region that is absorbed in the target region per unit mass.

Though it seems that the quantity absorbed dose fraction is erroneous in calculating doses to globular tumour cells from incident neutron beams, where the absorbed fraction might seem to be unity, its importance is extremely meaningful when addressing non uniform particle/ion distributions such as in the case of neutron capture events in boron.

7.2 A Monte Carlo simulation

The work undertaken here is a precursor or a first endeavour into unravelling the nature of neutron beams in amongst complex fields and their cell killing effects on viable, resilient, cultured animal cells with varying morphologies similar to human tissue.

Approximations have been made in order to attempt to answer the monolayer/suspension problem, specifically with respect to V79 cells incubated in boric acid:

(1) Boron – neutron capture and decay, leads to a lithium ion and alpha particles, this occurs uniformly throughout the medium. No attempt is made at having a perturbed neutron flux through „layers‟ of cells/dish/medium.

(2) Boric acid mediated irradiations have uniform boron distributions, intracellular and extracellular. No attempt was made at modelling variable uptake of boron, but non uniform distribution of nitrogen were considered for the $^{14}N(n, p)^{14}C$ reaction.

(3) The lithium and alpha particles are emitted back to back, ignoring the energy deposited by the emitted gamma ray in 94% of cases.

(4) Cells are treated as ellipsoids or spheres, which act as tally volumes. No cell kinetics/dynamics is considered.

(5) Particle tracks are straight lines (with correct variable LET). Tracks neither detour nor have variable ranges/trajectories.

(6) The lithium ion is taken to have the same LET to specific lethal dose relationship identical to alpha particles. This assumption can be broadly justified based on the work of SØRENSEN et al. [28] which shows a strong correlation between the LET and RBE of lithium ions and helium ions.

With these simplifying approximations, Monte Carlo methods were employed to simulate particle tracks in semi-stochastic cell geometries – sampled from distributions generated from confocal microscopy [24]. More complex models of random packing of arrays of cells can and have been used in our work but are beyond the remit of the thesis at hand, which only requires a solution for the microscopic dose from a uniform boron distribution but with a boundary in place limiting its scope. The code is written and optimised in such a way that randomly packed lattices can be used for dose estimation and calculation of survival in more realistic human tumour cell morphologies and packing densities.

To make use of absorbed doses to cells and to calculate survival probabilities [discussed in chapter 9] for cells of varying morphologies and radiation distributions, it becomes necessary to accurately model a realistic cell target or a critical region – susceptible to damage and/or death.

V79 cells grown on monolayers take very different cell and nucleus shapes to those left to grow freely in suspension. On monolayers, these cells often resemble fried eggs with an ellipsoidal nucleus (figure 7.6), covering over 90% of the visible area, whereas in suspension they are spherical and tightly packed.

The morphology of V79 cells has been studied by a number of authors and the distribution of cell sizes in monolayers are readily available from confocal microscopic imaging work. Experimental Nuclear size distributions can be seen in fig. 7.5, from the work of Hill et al [24]. For monolayers, cell nuclei are taken to have a mean nuclear thickness to cell height ratio of 0.8 (figure 7.6). This was subsequently used for stochastic, single cell, monolayer tally volumes for the track segment simulations.

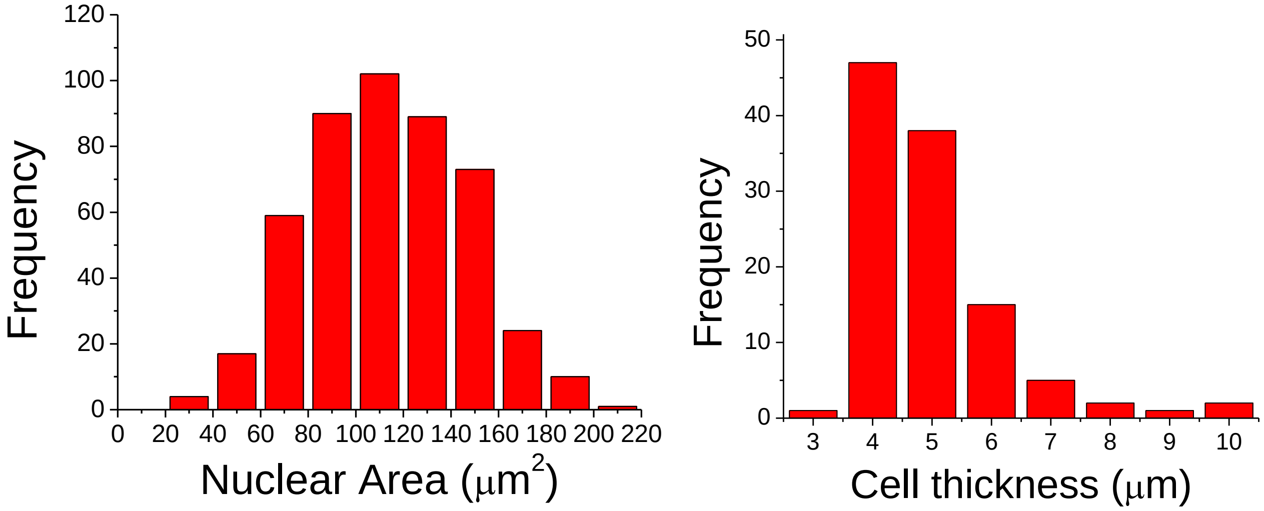

Figure 7.5 Area and cell thickness distributions from confocal image analysis (method described in [24]).

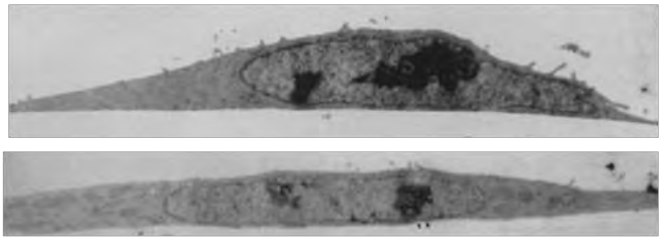

Figure 7.6 Typical EM section of attached V79-4 cells, with a mean nuclear to cell thickness ratio of 0.8.

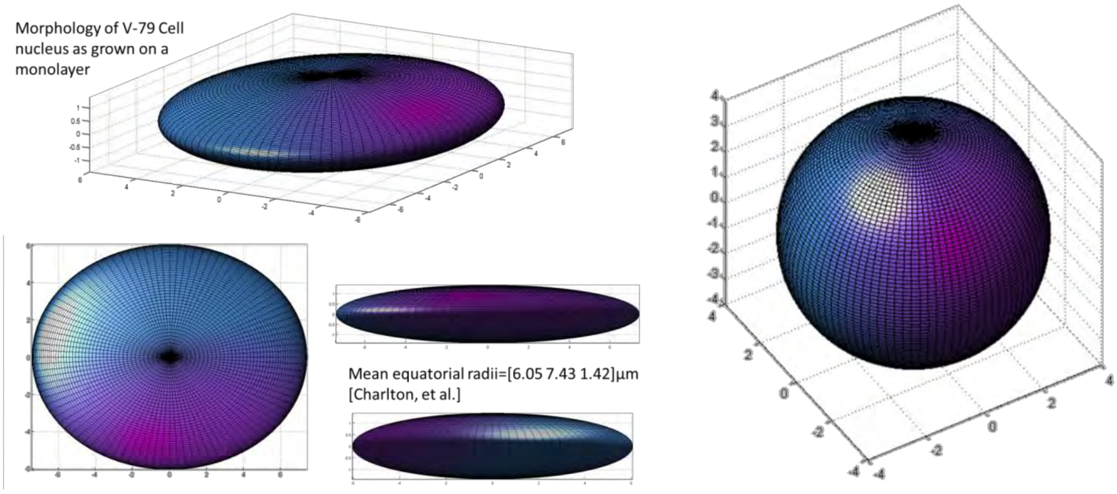

Figure 7.7 Matlab rendition of an ellipsoid and Sphere, simulating a V79 nucleus, of mean equatorial radii = [6.05 7.43 1.42]µm and radii = [4 4 4] µm respectively.

Cell nuclear areas and Cell thicknesses were randomly sampled using Marsaglia‟s table look up method [22], from the two empirical distributions shown (figure 7.5). The nuclear area was assumed to be circular, such that the two axes of the ellipse which form the cross sectional area were equal.

Mathematically these ellipsoidal „nuclei‟ can be described in vector notation and solved for line intersection within a matrix algebra environment such as Matlab™.

The equation of an ellipse in vector notation can be written as:

$$(X - x_0)^T * H * (X - x_0) = 1$$

Where (x_0) is the location of the centre of the ellipse and H is a positive definite symmetric matrix and $X - x_0$ a vector. The eigenvectors of H define the principal directions of the ellipsoid and the inverse of the square root of the eigenvalues are the corresponding equatorial radii. i.e.

- $H = \begin{bmatrix} 0.0273 & 0 & 0 \\ 0 & 0.0181 & 0 \\ 0 & 0 & 0.4959 \end{bmatrix}$

- MATLAB >> 1./sqrt(eig(H)) = [6.05 7.43 1.42] i.e. the equatorial radii from Charlton et al.

Thermal neutron capture in boron leads to alpha decay with the emission of two densely ionising particles, a lithium ion and an alpha particle, in one of two modes of decay observed. This reaction has a Q value of 2.79MeV, shared between the decay products, which in 94% of decays occur from an excited state from which the disintegration is accompanied by a 478keV gamma ray, which can be used for imaging in a therapeutic, BNCT radiotherapy setting (see Appendix A [Minsky et al.]).

As the cross-section of boron peaks at very low (thermal) neutron energies, ~<0.5eV, the initial neutron energy contributes very little to the final kinematic makeup of the emitted ions which carry a combined kinetic energy of 2.79MeV or 2.31MeV in its two decay modes (figure 7.8). Thus both particles can be considered to be „emitted" back to back with this shared kinetic energy inversely proportional to their masses.

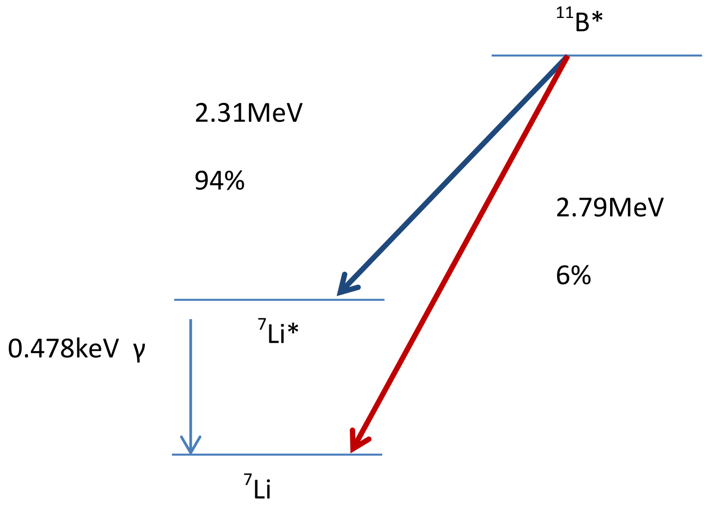

Figure 7.8 Alpha decay of boron, showing both modes of decay and particle energies.

The Monte Carlo transport code SRIM [5] was used to calculate the range and LET of these light ions in biologically equivalent tissue/medium (figure 7.9). These simulated back to back tracks can, for the purpose of simplicity, be considered a single track with a varying LET along its length, see figure 7.9, which is identical to the two individual tracks placed back to back.

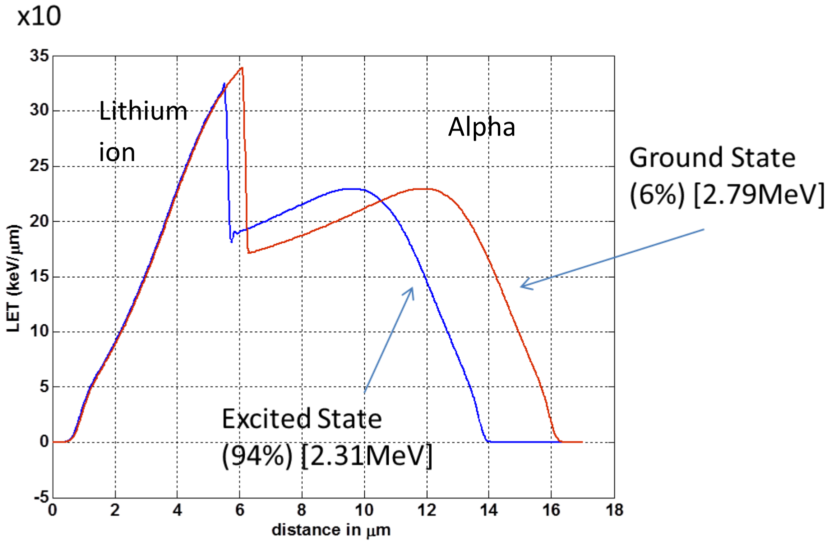

Figure 7.9 Back to back particle LETs as a function of distance, for lithium ions and alpha particles calculated using SRIM.

Hence, for any given decay, only the intersection of a line, representing the track segment, defined by a vector equation, need be solved for its intersection with any of our given cell nuclei.

The Equation of a line starting at (0,0,0) in vector notation is given by:

$$X = dI$$

Where, d= distance along line from starting point, and I= unit vector in direction of line.

Solving for d yields the points of intersection of the line with any number of spheres or ellipsoids in its path.

The solution of the line ellipsoid intersection is limited to the combined track lengths of our two particles ~14µm. The particle track is checked against each and every cell in the geometry for intersection and a list of all events per cell is recorded along with the starting and end points of the track crossing.

The Chord length distributions within the tally cell are calculated from the vector normal of the point of track intersection on entry and exit from the cell. In the case of events which originate in the cell nucleus or start outside but stop inside the cell (i.e. Starters and Stoppers), fixed track start points and end points are applied.

In Euclidean three-space, the distance between points x and y is given by

$$d = |\boldsymbol{x} - \boldsymbol{y}| = \sqrt{\sum_{i=1}^{n} |x_i - y_i|^2}$$

An integral lookup up function is used to rapidly ascertain energy deposited in any cell traversal. The lookup function consists of the integral of the LET/stopping power distribution of the two particles over their combined range. The difference between the entrance and exit „lookup" is equal to the energy deposited.

From the energy deposited the specific energy (imparted) can be calculated:

$$z = \frac{\varepsilon}{m}$$

Where ε is the energy deposited and m the mass of the sampled nucleus

Another parameter recorded during a particle traversal of the nucleus is the average LET i.e. the lineal energy (y), of the traversal, which is taken to be the energy deposited (ε) divided by the track length of the event (l) and not the average chord length as per conventional microdosimetric measurements.

$$y = \frac{\varepsilon}{l}$$

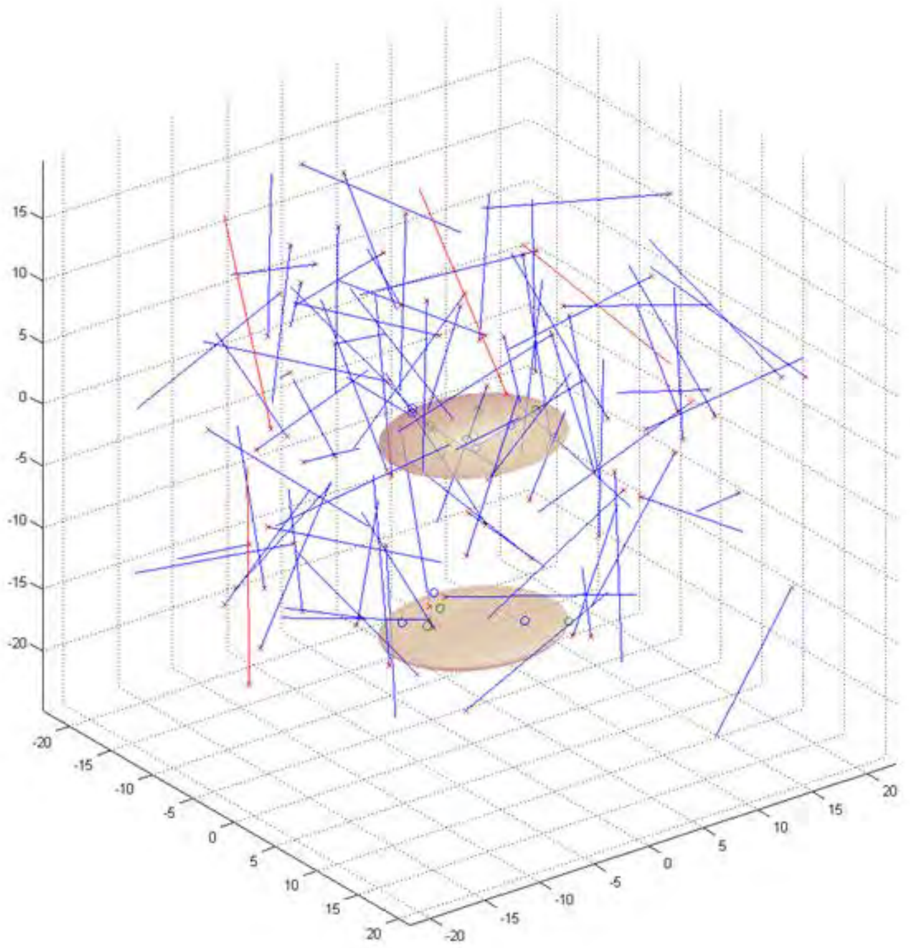

Figure 7.10 Particle track simulation (of varying LET) representing a medium containing boron irradiated in a uniform isotropic neutron field. Cell nuclei can be seen as oblate spheroids and the two decay modes of boron (94% in blue and 6% in red).

For any given source / target geometry microscopic absorbed doses are calculated by sampling the required macroscopic dose from a Poisson distribution of events and that number of tracks is simulated. Multiple repeat samples are carried out at each dose point to improve statistics and obtain survival curves (Chapter 9). Figure 7.10 shows an example of such a dose simulation with tracks representing the Li/alpha ions and ellipsoids representing cell nucleii in homogeneous and inhomogeneous fields.

7.2.1 Code Tracking Validation

A useful analytic check of the tracking/intersection algorithm is to randomly sample tracks (lines) from a uniform isotropic distribution about a single cell. i.e. checking for μ-randomness (mean free path randomness).

Mean free path randomness is defined as: “A chord of a convex body is defined by a point in Euclidian space and a direction. The point and the direction are from independent uniform distributions. This randomness results if the convex body is exposed to a uniform isotropic field of straight infinite tracks.” [29]

The probability density function for chord length distributions sampled in a sphere under conditions of μ-randomness i.e. such that the field of lines is isotropic and its intensity is independent of direction, is given by:

$$f_\mu(x) = \frac{2x}{d^2}$$

Where, x, is a chord length and d the diameter of the sphere. The mean value of the chord lengths in the sphere is given by:

$$\langle x \rangle_\mu = \frac{2}{3}d$$

In order to generate these uniform isotropic field lines and check the tracking algorithms in the source code, a sphere of unit radius is created at the origin. On the surface of the sphere a singular point is chosen from which all test rays originate. A single test point suffices as our convex surface is spherically symmetrical. Randomly sampling many points over its surface is a redundant and unnecessary action.

Tracks are generated about this point relative to the surface normal, such that events are uniformly and isotropically distributed in μ-randomness [30].

The direction cosines (u,v,w) of these tracks to the surface normal are given by:

$$u = \xi^{1/2}\,\frac{{x_1}^2 - {x_2}^2}{{x_1}^2 + {x_2}^2}$$

$$v = \xi^{1/2}\,2\frac{x_1 x_2}{{x_1}^2 + {x_2}^2}$$

$$w = (1 - \xi)^{1/2}$$

Where ξ is a random number between 0,1

and $x_1 = 2\xi_1 - 1,\ x_2 = \xi_2$

This is done by choosing a line segment whose origin is randomly distributed in space from a normal distribution and creating a random direction vector to project that line both forward and backwards from the point of origin of the line.

The vector equations of the line segment and the sphere are then solved to yield intersection points. The traversals lead to chord lengths, whose collection over many such events results in a chord length distribution. Figure 7.11 (B) shows the computed chord length distributions for a sphere of radius 10, which within statistical uncertainty fits in excellent agreement with the analytic distribution (figure 7.11(A)). The mean chord length of the computed distribution equalled 6.67 which is again in agreement with the analytic 2/3d i.e. 6 2/3.

Kellerer [31] derived mathematical proof that the chord length distributions in an oblate spheroid are given by the analytical functions:

$$2s\frac{2s}{c_1 d^2}[c_2+\frac{\sqrt{1-e^2}}{4(e^{-2}-1)}\left\{\sqrt{\left|\frac{d^2}{s^2}-1\right|\left(\frac{d^3}{s^3}+\frac{3d}{2s}\right)+\frac{3}{2}ci\left(\frac{d}{s}\right)}\right\}$$

$$ci(x)=\begin{cases} cos^{-1}(x), & 0\leq x\leq 1\\ cosh^{-1}(x), & x>1\end{cases}$$

$$c_1=\frac{1}{2}+\frac{e^2}{2\sqrt{1-e^2}}ci\left(\frac{1}{e}\right)$$

$$c_2=\frac{1}{4e^2}+\frac{3}{4}c_1$$

Where d= diameter, e=elongation

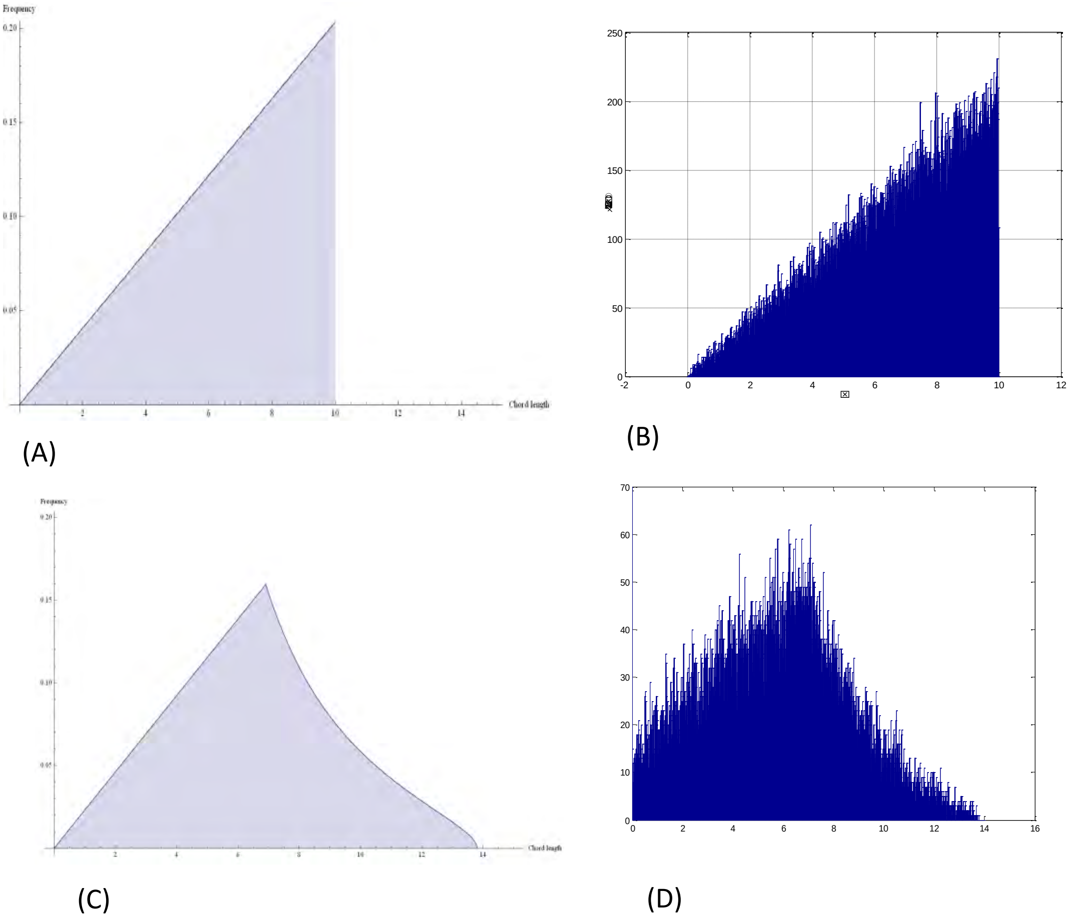

(A)

(B)

(C)

(D)

Figure 7.11 Comparison of Chord length distributions simulated in a spheroid (B) and oblate spheroid (D) plotted along with analytical calculations of chord length distributions (A), (C). Sphere radius =10, oblate spheroid of diameter d=13.8, elongation e=0.5.

Figure 7.11(D) Show the calculated chord length distribution for an oblate spheroid with an elongation of 0.5 and diameter 13.8, again the results are in good agreement with the analytic calculations shown in figure 7.11(C).

Having established and analytically checked the fundamentals of the working code, namely the sampling distribution and the chord length distribution are in agreement with analytic calculations. It becomes relatively easy to translate from line intersections and chord lengths to single event microscopic doses.

7.2.2 Modified Sampling/variance reduction

The non analogue sampling of the lower probability branch of the ^{11}B decay can drastically improve the variance reduction and statistical uncertainty of the final dose thus minimising computational time and increasing the Figure Of Merit (FOM), often defined in Monte Carlo codes as being inverseley proportional to the time and inverseley proportional to the square of the relative error.

This has been implemented by increasing the frequency of the 6% decay mode to 50% of events and assigning these particles an adjusted weight, equal to the ratio of the analogue to non-analogue biased event frequencies. The final tally contributions from particles is then adjusted by their weights, which compensates for the bias and keeps the tally „fair" i.e. gives a correct particle density in any region of phase space.

7.2.3 Results

Simulations were carried out for a cell irradiated at the centre of a homogeneous distribution of boron capture events and simultaneously for one irradiated on the boundary of the same distribution. The boundary was such that the cell nuclei sits with its surface at a distance equal to 10% of the cell height from the boundary i.e. as is observed from confocal images, which is ~0.3μm.

Figure 7.12 shows an example of the results of the microscopic absorbed dose seen in the two situations as a function of the number of histories. It is evident that the tallies reach much more stable results as more events are sampled and that the tally approaches its mean in a random manner thus passing one of the known tests of Monte Carlo convergence.

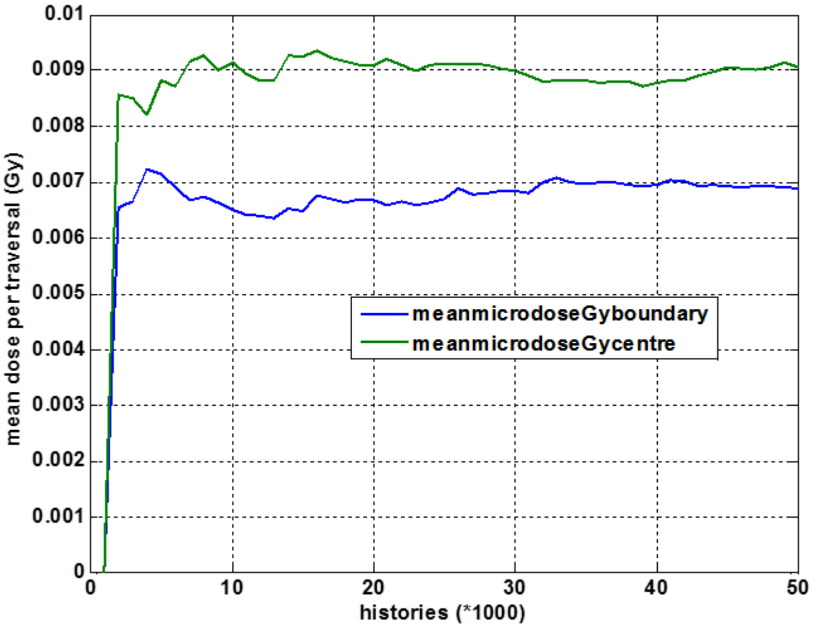

Figure 7.12 Tally results for mean energy deposition per source particle for a cell irradiated homogeneously (green)/inhomogeneously (blue), as a function of particle histories.

As is well known in Monte Carlo methods, the process is statistical and false convergence is possible. To address the statistical validity of our results, we have adopted some of the widely known checks for statistical certainty.

Defining the standard deviation of the mean as:

$$\sigma = \sqrt{\frac{\sum_{j=1}^{N} x_j^2 - \bar{x}}{(\mathrm{N} - 1)}}$$

and the relative error as:

$$Relative\ error = \frac{\sigma_{\bar{x}}}{\bar{x}}$$

The calculated standard deviations and relative errors for the two data sets shown in figure 7.12 are given in figures 7.13 and 7.14 respectively. The relative error is seen to decrease as a function of history [number of source particles simulated (nps)] and falls of at a rate equivalent to 1/sqrt(nps). As is evident from the graphs, the relative error converges to less than 0.10%, considered the upper limit on reliable statistics and is of the order of 3-4% after 50,000 histories.

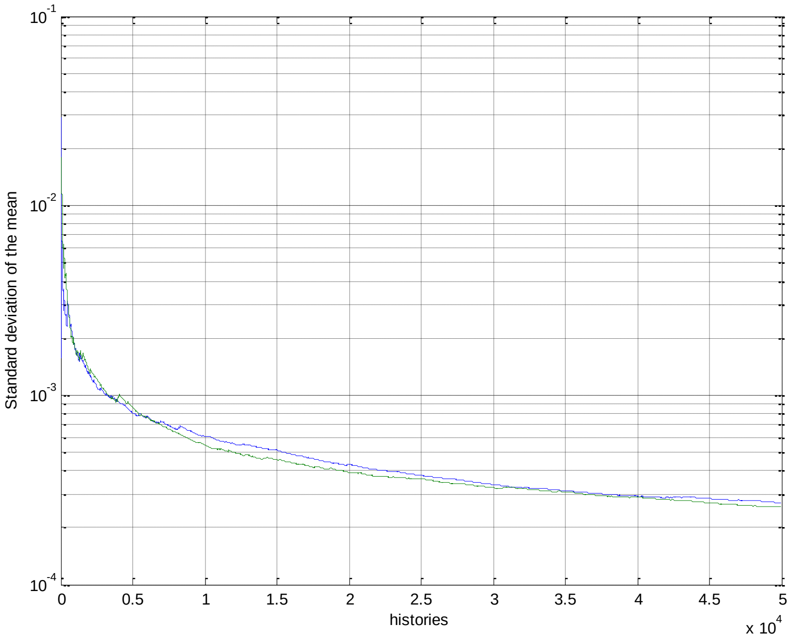

Figure 7.13 Statistical check I for convergence, standard deviation of the mean as a function of histories per source particle.

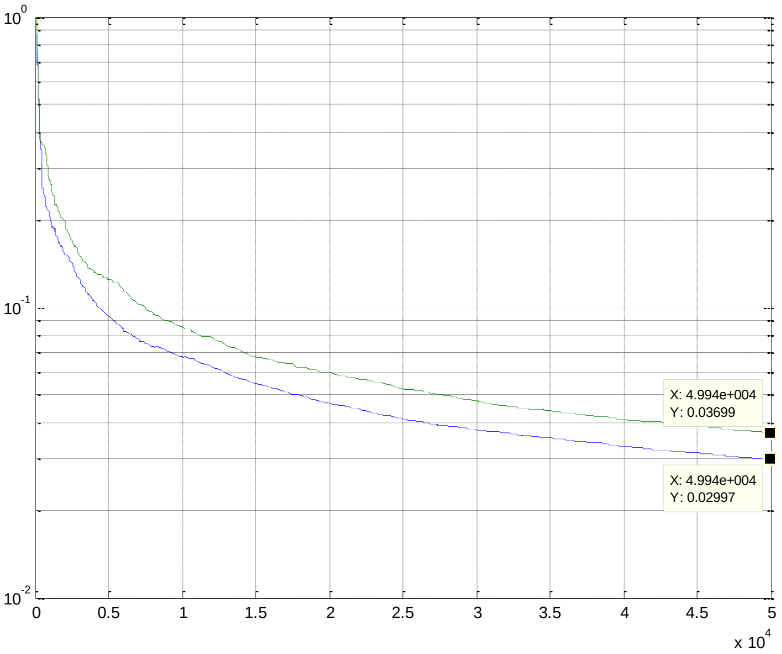

Figure 7.14 Statistical check II for convergence, relative error as a function of histories per source particle.

Figure 7.15 shows a particle simulation of an extension to the previous calculation with numerous tally volumes, representing cell nucleii approaching a boundary. The results of the simulations, shown in figure 7.16, show that the inhomogeneity tends to cause cells at boundaries to have a lesser absorbed fraction than those uniformly irradiated. In the case of the boundary, the cells would receive only 0.77±0.05 of the absorbed dose calculated in the macroscopic sense. Note that the points have been calculated with ~5% relative error, thus the fluctuations around the absorbed fraction of 1 for cells in uniform dose distributions.

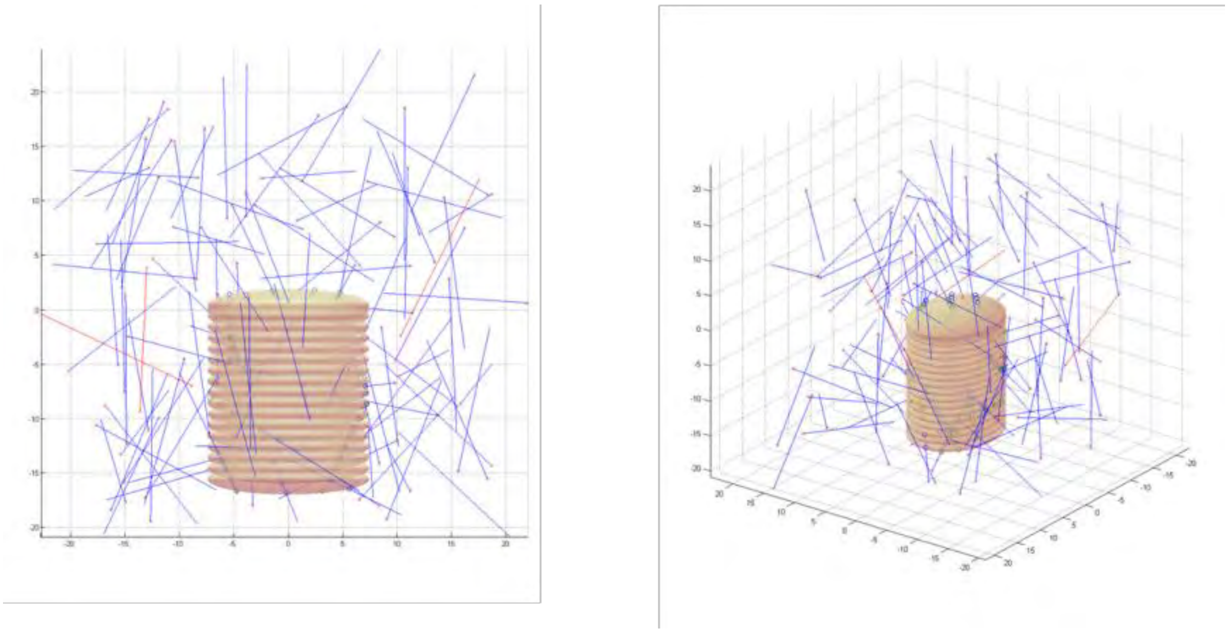

Figure 7.15 Simulations of cells approaching an inhomogeneity in an otherwise uniform field.

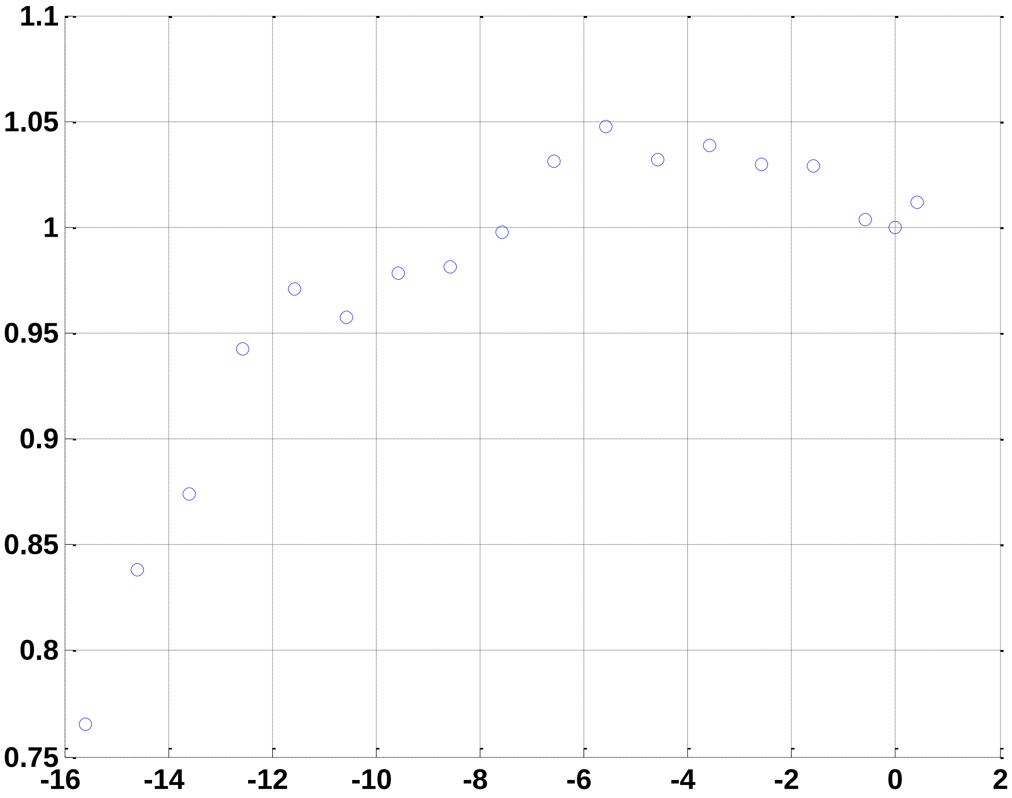

Figure 7.16 Absorbed dose fraction as cell nucleus approaches inhomogeneity in an otherwise uniform field. Units on the x-axis are in microns, y-axis is the absorbed fraction.

7.3. Experimental validation

Phoenix et al [19]. carried out work at the Birmingham BNCT facility to validate absorbed dose fractions to cells irradiated in monolayers exposed to a non-uniform distribution of boron in the surrounding medium. Glass dishes, commonly known as „jelly fish" dishes, were paired facing each other with cells grown on a layer of mylar sandwiched between the two dishes and the sides sealed, see figure 7.17.

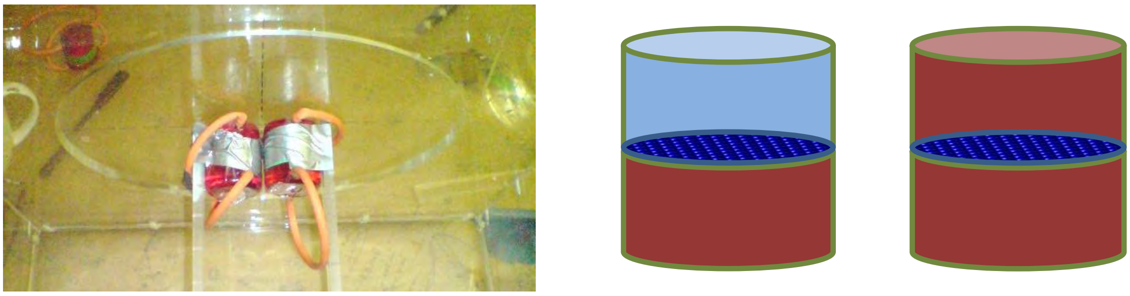

Figure 7.17 Two, paired, jelly fish dishes in a Large Water Tank, pre-irradiation, schematic showing boron loading in the two dishes, red indicating boronated medium and blue indicating medium free of boron.

The two sets, of paired dishes, were irradiated in parallel, one with boric acid distributed uniformly in both sides of the dish and the other pair with boric acid in only one side of the glass dish (as per the Birmingham and MIT radiobiology experiments). The irradiation of two pairs of flasks therefore alleviates the need to correct independent runs for beam inhomogeneity in flux delivered and yield variations during long irradiations (described previously).

	Single sided calculated dose (Gy)	**Double sided calculated dose (Gy)**	**Ratio**
30 minutes	0.80	1.08	0.74
45 minutes	0.87	1.19	0.73

Table 7.1 Calculated doses to cells based on survival assays and the corresponding absorbed dose fraction (Ratio).

Surviving fractions allowed for an estimation of dose delivered to each of the two dishes by unfolding the mixed field of irradiation and thus leaving the boron component of the dose, thus enabling the calculation of calculated absorbed fractions from the shift in the boron survival curves, Table 7.1. Results show an experimental absorbed fraction of 0.73-0.74 with large uncertainties. Note that the 1µm thick mylar substrate onto which the cells are grown degrades the passage of lithium and alpha particles in the double sided irradiations and thus measurements are not of a truly uniform boron distribution.

7.4 Conclusion

Boron doses calculated in inhomogeneously boron loaded cell irradiations, carried out at the Birmingham and MIT BNCT facilites, requires correction for dose absorbed fraction, a microdosimetric quantity related to the local boron distribution in and around the cells. Detailed calculations show an absorbed fraction of 0.77±0.05. Experimental attempts at proving this by applying a more uniform boron distribution show absorbed fractions of 0.73 – 0.74. Cell experiments have in themselves large systemic uncertainties – for which no repeat measurements were carried out.

Inherent uncertainties in the simulations are few and reasonably well known.

(i) The boron cross section is only known to ~ 5% confidence. This, however, would not affect the absorbed dose fraction.

(ii) SRIM ion transport, cross section and physics models have an uncertainty estimated to be 10%.

(iii) Ion detour is not modelled [it was assumed that ions travel in straight lines]

(iv) Ions transported in medium and cells have the same stopping powers.

(v) Neutron fluence across the cell population was treated as uniform and in reality will vary across the flask surface.

(vi) Boron uniformity in cell nucleus and cytoplasm has not been proven.

Chapter 9 uses the results of these simulations to create survival curves from LET distributions recorded in the simulations carried out in determining absorbed fraction.

Chapter 8

THERMAL NEUTRON DOSE

The „thermal neutron" dose is one of the four major components of dose in BNCT, the others being the Boron, Fast neutron and Photon. The thermal component in itself refers to any particulate dose resulting from the capture of thermal neutrons in matter. Nitrogen has a relatively high natural abundance amongst elements in the human body; it is 3.3% by weight in muscle tissue and 2.2% by weight in brain.

Gabel et al. [27] in trying to determine the RBE of V79 Chinese Hamster Cells to capture reactions in boron and nitrogen has accurately measured the nitrogen content of V79 cells by counting the number of cells grown in suspension. The cells were then centrifuged and the supernatant fraction removed by suction. The dried and weighed sediment was analysed and his results show that V79 cells have 1.7% by weight nitrogen in wet cells.

The capture of thermal neutrons in nitrogen, $^{14}N(n,p)^{14}C$, has a reaction Q-value of 625.87keV (±0.004)[2] and results in a recoil proton carrying 580keV of the energy, the carbon ion carrying 42keV. The recoil proton and carbon ion have ranges in water of ~10µm and 0.23 µm respectively, the proton range being comparable to the lithium/alpha range but with wider lateral straggling.

Gabel et al. [27] further estimated the true nitrogen dose deposited in cells irradiated in single cell suspensions at the cold neutron source at Institute Laue_Langevin (ILL) and the Medical

Research Reactor at Brookhaven National Laboratory (BNL) to be **85% and 65%** respectively, with nitrogen content in the cell growth medium differing between the two experimental set ups, being 0.9% and 0% by weight respectively. From the absorbed doses and survival measurements, RBE"s of 2.3 and 1.9 were calculated for $^{10}B(n,\alpha)^{7}Li$ and $^{14}N(n,p)^{14}C$ respectively.

White [32] has grossly approximated the decrease in the thermal dose component of the MITRII Epithermal beam, in the absence of boron, for a Chinese Hamster Ovary [CHO] cell line grown as a monolayer in T25 flasks to be 50% due the difference in nitrogen component of the medium, flask and cell line as well as including geometrical factors. Arriving at this value, she assumed nitrogen content of CHO to be the same as that of tissue, the content of nitrogen in medium to be 0.014% by mass and none in the T-25 flasks. (I) The protons from the thermal capture in nitrogen, originating in a cell, were thought to leave any cells before depositing most of their energy. (II) Capture in the flask walls would be dominated by hydrogen and carbon, both of which emit gamma rays – measured by ion chamber dosimetry. (III) the dose components from thermal neutron capture were approximated by kerma factors, 8.54e-13cGy/cm2 in medium, and 3.3E-13cGy/cm2 in the flask walls compared to 1.79E-11 cGy/cm2 for ICRU 46 adult whole brain. This led to an estimate of a CHO cell kerma factor of half that of brain i.e. 50% absorbed fraction [in this particular radiation geometry and absence of boron].

Mason et al.[33], has carried out a detailed comparison and analysis of the beam quality, in terms of high and low LET dose components at various depths, for two European NCT facilites, the Birmingham accelerator based, pre-clinical, facility and the Studsvik nuclear reactor based, fully clinical, facility. Their relative effectiveness on clonogenic assays of V79 cell kill was determined in the absence of cell repair mechanisms by maintaining the cells at low temperature (4 degrees C). The cells were irradiated in vials as opposed to flasks and were thus in „suspension‟. She, like the previous authors, also estimated the absorbed dose fraction, as the microdosimetric analysis was beyond the scope of her study. She reports a nitrogen content, in Dulbecco‟s Modified Eagles Medium (DMEM) and 10% foetal calf serum with 1% Glutamine and 1% penicillin of 0.3%, and uses the 1.7% determined by Gabel et al. [27] as the V79 cell nitrogen content. In calculating her true absorbed nitrogen dose she averages down the 1.7% N in cells to 1.1% by weight i.e. an **absorbed fraction of 65%**.

In the case of the present study, to quantify the dose, both macroscopic and microscopic, to cells irradiated in a monolayer at both the MITRII Fission Converter Beam (FCB) and at the University of Birmingham‟s 2.8MeV Dynamitron particle accelerator: The V79 cells were grown as monolayers and incubated in a medium containing boric (H_3BO_3) acid. Boric acid contains no nitrogen, neither the Mylar film onto which the V79 cells attach nor the polyethylene T25 flasks, on which the cells are plated and irradiated contain any nitrogen.

The medium in which the cells are irradiated, in the presence of 50ppm boric acid, contains 0.012% by weight nitrogen, the added 10% by weight bovine foetal calf serum – contains approximately 1% by weight nitrogen [39]. Thus the only major nitrogen component of the nitrogen-thermal neutron dose is the cells themselves (1.7% by weight nitrogen) and the aggregate medium, ~0.11% by weight nitrogen.

8.1 METHOD

V79 cells have an atomic composition which is very similar to that of human spleen [6][7]. In the calculations presented, spleen has been used as a substitute for V79 cells in the ion transport code SRIM, it has been taken to have a density of 1.08 g/cm^3[6][7]. From SRIM calculations, the longitudinal range, for 580keV protons, varies depending on the target material of choice. For soft tissue, spleen and water, the range varies from 9µm, 10.2µm and 11µm respectively [See figure 8.2]. The lateral range projection of protons in spleen is ~2452Å and 2738 Å in water. Straggling of this order is thought to have very little effect on the calculated microdosimetric parameters for small nuclei [34]: "the results also shows that for nuclei of less than 5µm in size, both lateral and range straggling effects of the charged particles on at least one of the microdosimetric parameters evaluated would appear to be inconsequentially small."

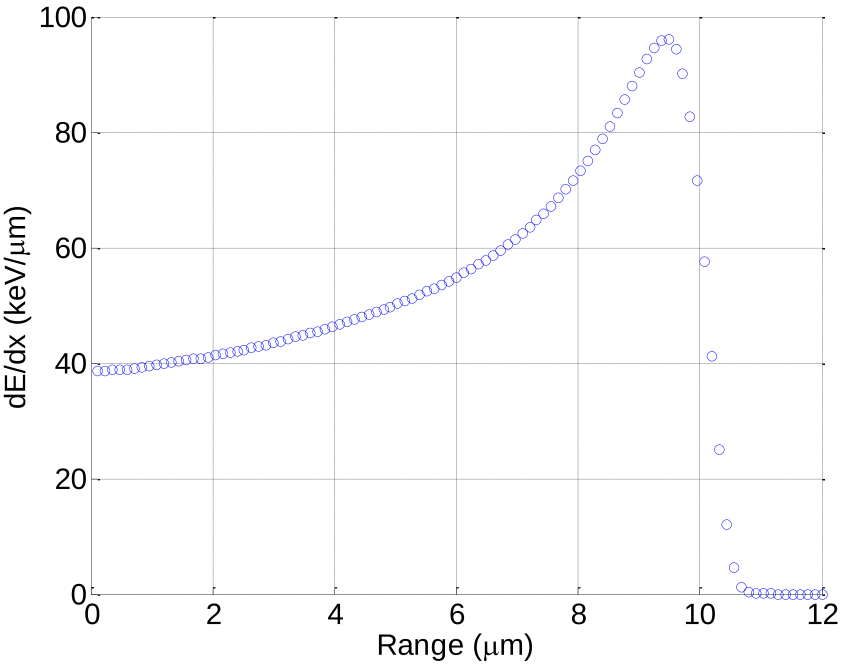

Figure 8.0 SRIM stopper power calculation of 580keV protons into human spleen (density =1.08g.cm^{-3}) - the range ~10.2µm .

With the assumptions and estimates of the previous authors/researches born in mind, simulations were carried out to definitively calculate the absorbed fraction of dose scored in nuclear volumes of V79 cells grown and irradiated in monolayer geometries. Transport calculations were carried out as as per the boron simulation problem [Chapter 7]. But as the ion tracks are now no longer homogeneously distributed, extra care must be taken to adequately sample event distributions and subsequent tracks that a real physical cell would see.

The 580keV proton emitted following the capture and decay of nitrogen in V79/spleen cells has a stopping power distribution shown in figure 8.0. The Bragg peak being much more clearly defined than in the lithium and alpha tracks. Its general shape supports White‟s [32] argument that much of the particle‟s energy is deposited towards the end of its range and with events confined to initiate only within the cell, most of the energy will be deposited outside of the cell.

Yam and Zamenhof [34], have simulated rigid 3D cubic arrays of cells for radiation transport simulations to account for all possible tracks that might enter a cell occupying a central location away from boundary effects. This array consisted of 27 cell nuclei (3 x 3 x 3) with the central nucleus being the dose target. For the present simulations, cells are grown as monolayers and thus only a single planar array of monolayer cells is needed, i.e. 3 x 3, to consider all possible track events originating from within the cell or the neighbouring cells which can impact on our target volume.

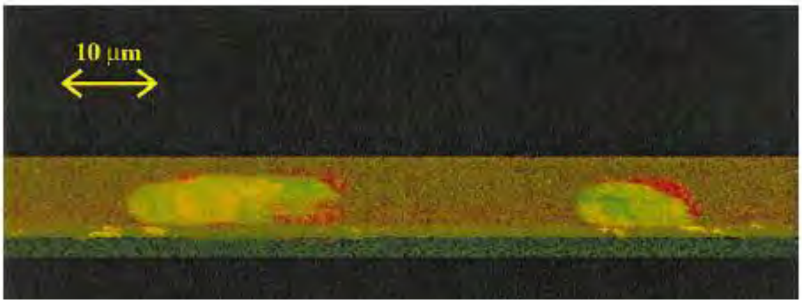

Figure 8.1 Vertical section of a confocal image through V79 cells plated on Mylar. Cell nuclei were stained with Hoechst (green signal) and the cytoplasm with Rhodamine (red signal), [40].

Representative confluent cells grown in monolayers by Phoenix et al, for this and monolayer radiobiology work done at the Medical Research Council (MRC), have been analysed at the MRC by Hill et al, using a Nikon Diaphot confocal laser scanning microscope with a Nikon Plan_Apochromat 63XNa1.4 oil-immersion objective lens and an ion argon laser operating at 488nm wavelength. The medium was stained with Fluorescein isothiocyanate dextran to cause the medium to fluoresce, thus making the cells distinguishable. Cell thicknesses were measured with a resolution of ~0.5µm (Hill et al. [24]). As has been previously stated, cell nuclear sizes and heights were sampled from these confocal image distributions to accurately account for the large variations in cell sizes seen in radiobiology experiments.

Cell sizes are sampled from the Marsaglia look up table of size/frequecy distributions and placed at a vertice of a 2D lattice array, each cell thus has a realistic (variable) size, which is always of the form of an oblate spheroid as only cell areas and heights are measured in the confocal imaging work. The two major axes are thus made to be equal and provide the correct cross sectional area.

Cell cytoplasms are simulated to be also centred on the array vertices and are of a height equal to 1/0.8 * nuclear height [24], and are given a major radius 6μm more than that of the nucleus.

The proximity of the cells in the array is allowed to vary by a parameter called the packing density, which draws the lattice locations of the cells closer or further apart. For the purpose of this work the cells are thought to have a packing fraction (confluence) (in terms of area covered) of greater than 90% and lesser packing densities are not studied.

The oblate spheroid representing the nucleus is then allowed a further two degrees of freedom anywhere in the direction of the monolayer plane and bound by the rigid cytoplasm (spheroid) it is considered to be within, this again is more realistic of the true morphology for cells grown in monolayers.

The medium surrounding the cells is such that it occupies all interstitial space between the cells and extending from the mylar film (the base onto which the cells are grown) and directly above throughout the whole flask. Thus the nitrogen external to the cell can be thought of as being uniformly distributed.

Nitrogen capture and decay events i.e. proton tracks, are sampled from within the cell monolayer volume, such that events that occur outside of the volume of any of the given cells in the array are partially rejected i.e. partial sampling by rejection, but in a manner that allows a fixed ratio of events to occur between cells and the volume (medium) external to the cells. This allows for the factoring in of inhomogeneous distributions between the cells and the surrounding medium. Figure 8.2 shows an example of sampled starting points for 580keV protons from within the cell cytoplasm, with no events occuring in medium, note how the points draw out the sampled cell nucleus and cytoplasm.

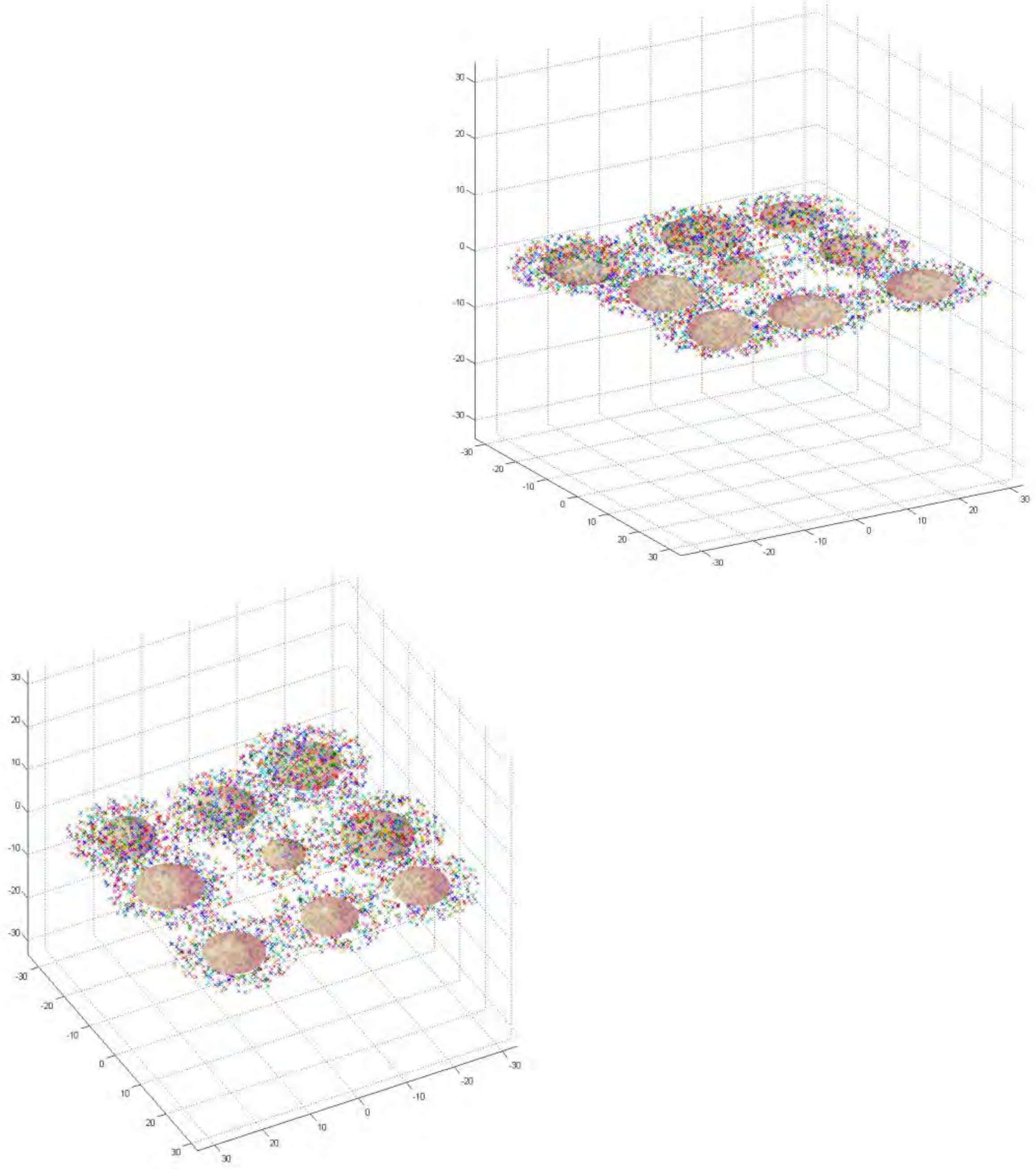

Figure 8.2 Example of randomly sampled starting points for 580keV protons, nuclei are shown as oblate spheroids. Note how the points highlight the area of cytoplasm and nucleus sampled.

Particle tracks are then generated isotropically (figure 8.3) and any scoring contribution to the central cell and nucleus (i.e. the target cell) is recorded. The procedure is repeated many times for any given geometry and repeated for different (stochastic) cell size distributions i.e. stochastic volume sampling from the frequency area and height distributions.

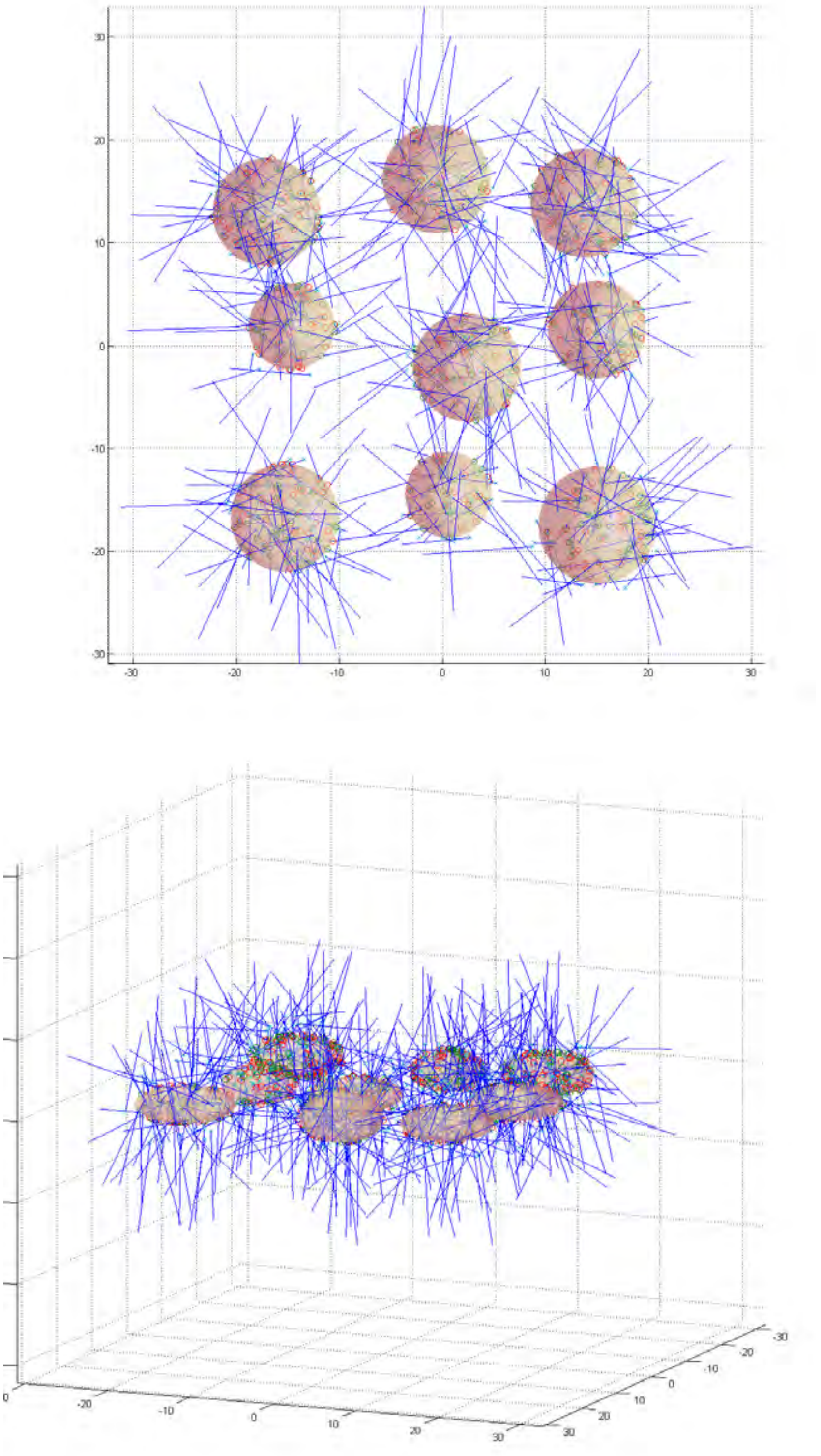

Figure 8.3 typical simulation of stochastic nuclear sizes and distributions, with proton tracks of 10.2μm range seen in blue.

8. 2 Simulation Results $^{14}N(n, p)^{14}C$

Figure 8.4 shows the changing absorbed fraction as a function of stochastic geometry. Depending on the nuclear size, cell height and statistics, differing amounts of dose are absorbed in the nuclei from tracks emitted in the nucleus itself and its nearest neighbours and the surrounding medium. The mean of the stochastic absorbed dose fraction = 0.479, for this particular intra/extra cellular Nitrogen distribution. Note the early history, where the calculated absorbed fraction is greater than 1! This is most certainly due to the overwhelming dose from neighbouring cells which left a greater dose in the cell than were the number of events generated in the cytoplasm itself i.e. a greater dose entering the cell than was released by it.

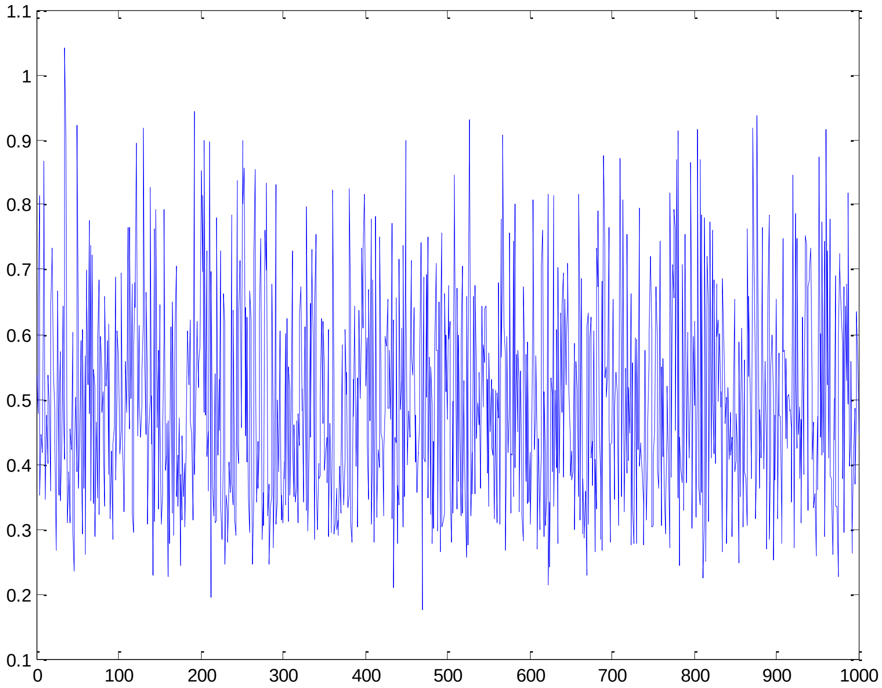

Figure 8.4 Absorbed dose fraction as a function of stochastic geometry, each stochastic geometry consisted of 1000 particles, ran recurrently over 1000 stochastic geometries.

Defining the frequency mean (y_F) lineal energy and the dose mean (y_D) lineal energy as the first moment and the ratio of the 2nd and 1st moment of the lineal energy distribution respectively, we have:

$$y_F = \int_0^\infty y f(y) dy \tag{8.1}$$

$$y_D = \frac{\int_0^\infty y^2 f(y) dy}{\int_0^\infty y f(y) dy} \tag{8.2}$$

Where y is the lineal energy and f(y)d(y) is the probability that an event is in the interval [y,y+dy].

The frequency mean and dose mean for cellular nitrogen capture events i.e. inhomogeneous distribution, 1.7% intracellular, 0% extracellular, as seen in figure 8.4 are:

y_F = 52.47keV/µm

y_D= 54.89keV/µm

for a homogeneous nitrogen distribution, (above the mylar only), the calculated frequency mean and dose means are:

y_F = 59.80keV/µm

y_D= 63.5keV/µm

Very few events, more than two orders of magnitude below the mean, are seen below 40keV/µm (figure 8.5), due to the fact that LET‟s of less than 40keV/µm are only possible at the very end of a particles range (see figure 8.2), the probability that only the end of a track intercepting and scoring in the nucleus is very, very small.

The average chord length in the non-homogeneous field is ~3.85μm, with a frequency mean of 52keV/μm.

Figures 8.6 and 8.7 show the distributions in LET and energy seen by the central target nucleus summed over many stochastic geometries. The inhomogeneous dose distribution has a very clearly more pronounced high energy portion to the spectrum and narrower low LET portion relative to the homogeneous distribution.

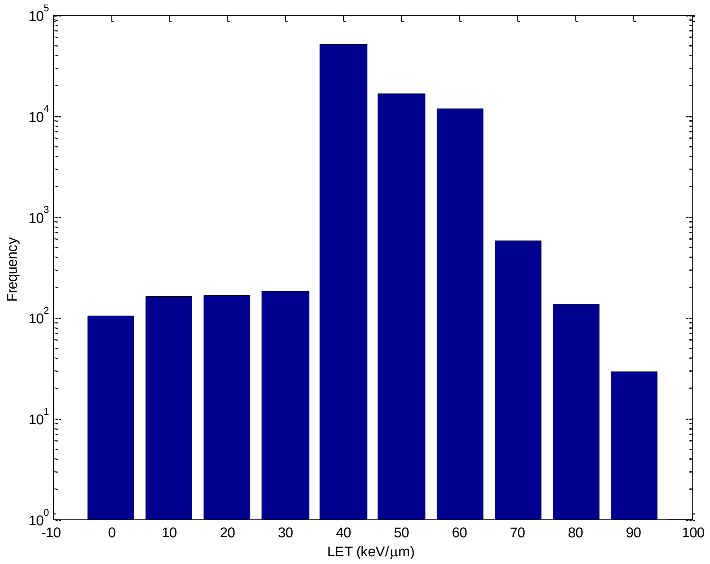

Figure 8.5 LET distribution of cell nuclear events, summed over 1000 stochastic geometries, 1000 events simulated per geometry.

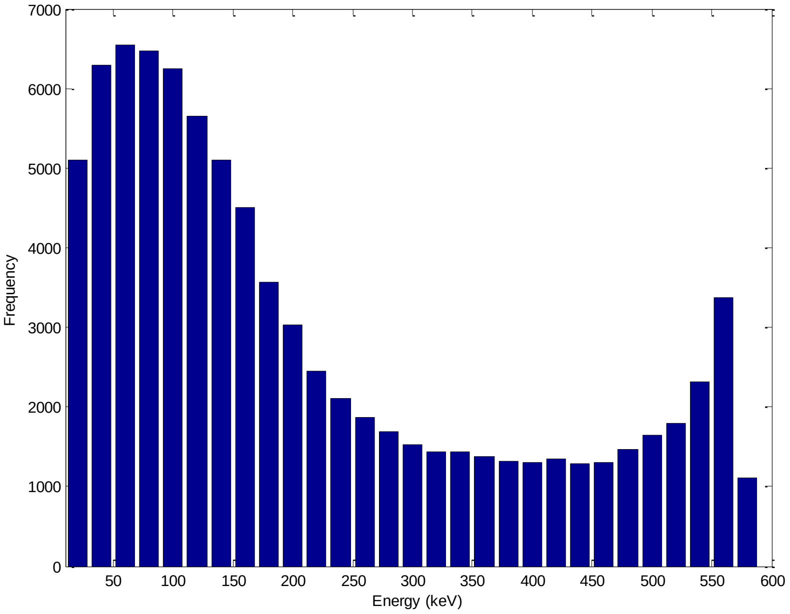

Figure 8.6 Distribution of single event energy depositions in nucleus for an inhomogeneous irradiation.

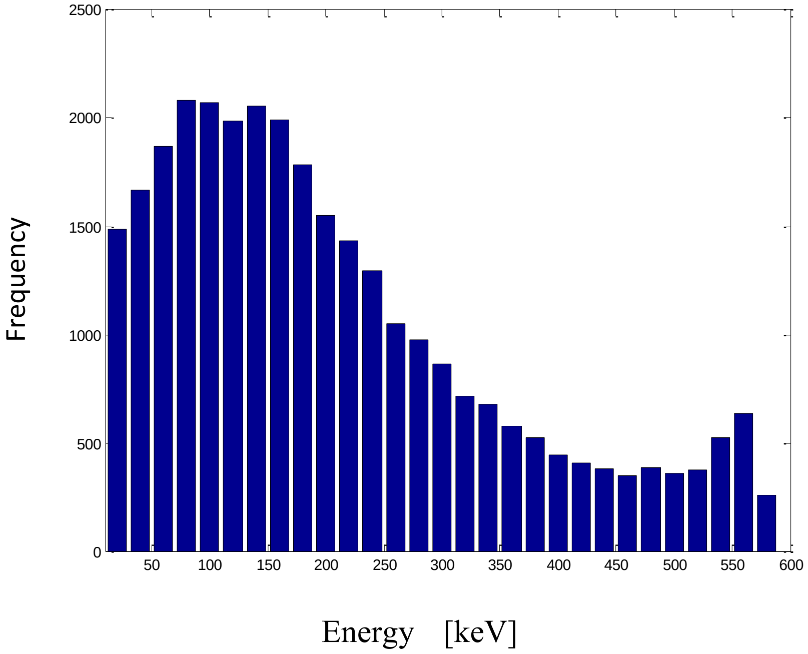

Figure 8.7 Distribution of single event energy depositions in nucleus for a homogeneous irradiation.

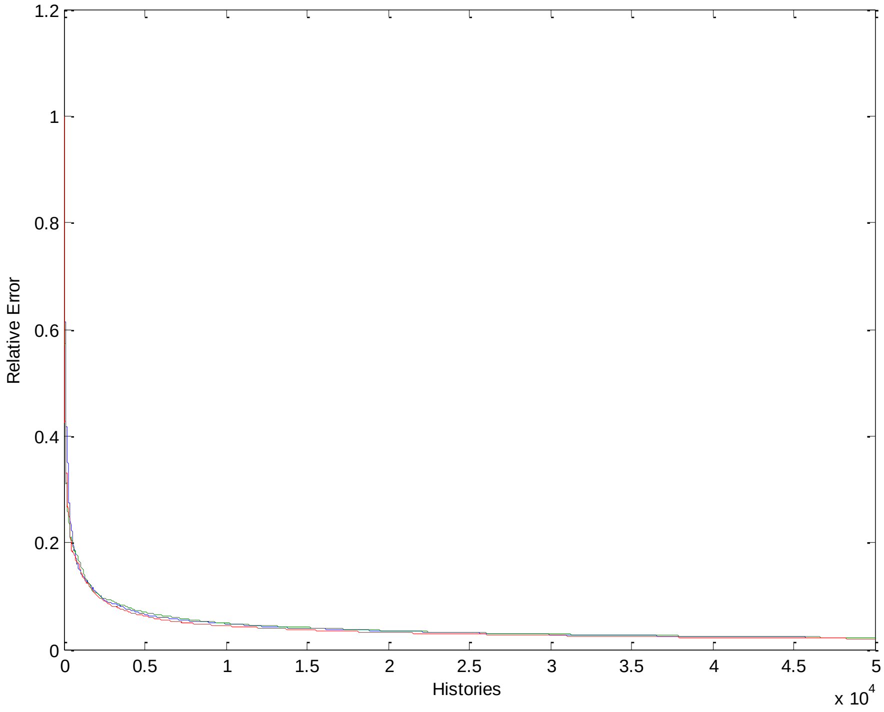

Figure 8.8 Summary of stochastic volume statistics for numerous samples from a population distribution.

Standard population statistics were applied in arriving at the estimated standard deviation of the population:

Population average result:

$$\overline{\overline{X}}_J = \frac{\sum_{j=1}^{N_{stoch}} x_j}{N_{stoch}} \tag{8.3}$$

Where $\overline{\overline{X}}_J$ is the population average of the sample average results (x_j) and N_{stoch} is the size of the population being sampled, i.e. the number of independent stochastic geometries sampled, Standard deviation of the population:

$$S_{x_J} = \left(\frac{\sum_{j=1}^{N_{stoch}} x_j{}^2}{N_{stoch}} - \bar{\bar{X}}_J{}^2\right)^{1/2} \qquad (8.4)$$

Estimated standard deviation of the population average:

$$S_{\bar{\bar{x}}_J}{}^2 = \frac{S_{x_J}{}^2}{N_{stoch}} \qquad (8.5)$$

8.3 Conclusion

Microdosimetric quantities calculated from the transport of 580keV protons resulting from the thermal capture of neutrons in nitrogen are given in table 8.1.

Nitrogen distribution, [% by Wt. Intracellular : extracellular]	Frequency mean LET, y_F,	Dose mean LET, y_D	Mean Chord Length	Population Average absorbed fraction $[\boldsymbol{\bar{\bar{X}}_J}]$	$\boldsymbol{S_{\bar{\bar{x}}_J}{}^2}$
1.7 : 0%	52.47	54.89	3.85	0.479	0.02

Table 8.1 Summary of calculated $^{14}N(n,p)^{14}C$ microdosimetric results.

The stochastic cell population simulations show that for an inhomogeneous nitrogen dose distribution (1.7 intracellular : 0 extracellular) the absorbed fraction is 0.48±0.02. This confirms the guess-estimate by White et al. [32] for similar monolayer experiments at MIT (in the absence of boron), who based their dosimetry on an absorbed fraction of 0.5.

These results don‟t readily apply to the absorbed fraction estimated by Mason et al. [33], as no cell suspension simulations were carried out for this dose component.

The absorbed fractions as calculated in Chapters 8 and 9, combined with the macroscopic dosimetry measurements and MCNP calculations (normalised to measurements) now correctly feed into the cell radiobiology work carried out by the Birmingham group for all the mixed field dose components aforementioned. The results of which can be seen in the following chapter.

Chapter 9

CELL SURVIVAL

9.1 Birmingham Cell Survival Results

An extensive radiobiological programme has been conducted by the University of Birmingham BNCT group and collaborating institutions. One of the prime objectives of this collective work remained the production of a validated protocol for the pre-clinical biological characterisation of the University of Birmingham BNCT facility and for this to be established internationally and utilised at all BNCT facilities.

The aim of this study was to quantify the doses, both macroscopic and microscopic, observed during the irradiations of cell monolayers at the University of Birmingham's 2.8MeV Dynamitron particle accelerator and at the MIT research reactor. V79 cells, incubated in 50ppm boric acid were irradiated at 2 depths in the LWT at 37˚C using standard radiobiology methods. Cell dosimetry was carried out using paired (dilute) gold and manganese foils along with Mg/Ar and TE ion chambers to calculate boron, thermal neutron, fast neutron and photon doses, at several depths in a standard large water tank (LWT). In the case of the Birmingham facility the Monte Carlo code MCNPX was used to calculate off-axis correction factors to the central depth dose curve for the Birmingham beam and perturbation factors caused by the presence of the boronated medium.

The combined outcome of cell survival experiments and the dosimetry methods, along with correction factors previously described, result in the survival curve, shown in figure 9.1, for the complete mixed field of the Birmingham epithermal beam. The cell survival data shown here being in excellent agreement with that modelled and predicted from the combined biological effectiveness of the separate beam components from the work of Gabel et al. [27], shown as green and blue lines on the plot. The relatively large spread in survival data is due to the large uncertainties in experimental data, the best fit of which is the black line overlayed by the green model of Gabel et al.

The work of Gabel et al. was not carried out in T-25 flasks nor as cell monolayers but in small cell vials with very different dosimetric requirements. There was neither boron inhomogeneity nor off-axis and perturbation corrections to calculate. Thus validating the dosimetry calculations for the present flask irradiations by their cell survival agreement with the cell vial irradiations.

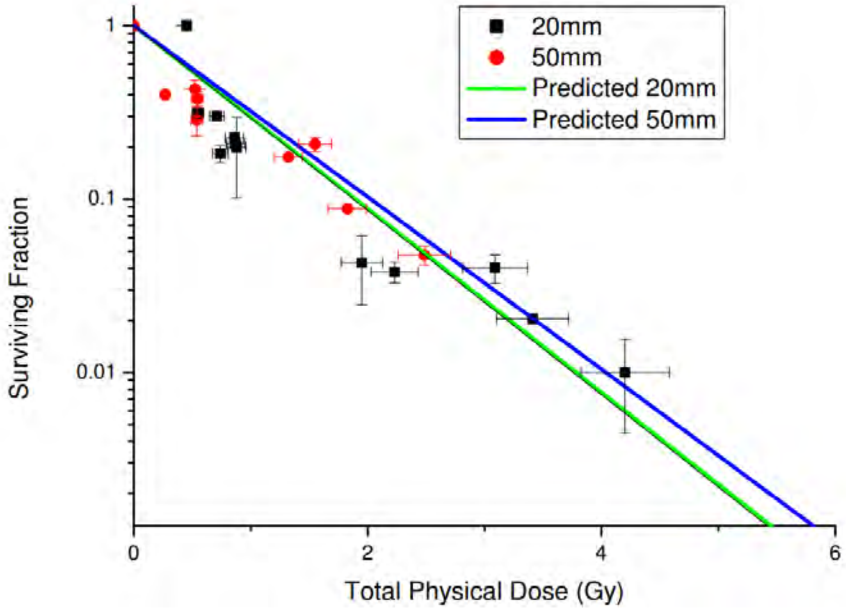

Figure 9.1 Calculated survival curves for uniform and non-uniform Li/alpha irradiations (from the PhD thesis of Phoenix[19]).

9.2 Modelling Cell Survival

Charlton et al. [23] have put forward a very useful foundation on which to embark on calculating the effects of inhomogeneities in more complex irradiation fields and compute survival curves on the basis of track segment irradiations to cell monolayers. This novel method allowed Charlton to accurately predict survival curves for the irradiation of V79 monolayers and suspensions from a uniform distribution of bizmuth-212 (an alpha particle emitter).

He introduces a parameter, specific lethal dose (D_0), which functions as a measure of cell kill. The fraction of cells surviving traversal by ionising particles of given LET is exp(-D/D_0), where D is the dose deposited, by rearranging for D_0 we have:

$$D_0 = -\frac{d}{\ln(1-\frac{d}{D_{37}})} \qquad (9.1)$$

Where,

D_{37} is the mean lethal dose for monolayer irradiations (track segment geometries) and d is the average dose deposited in the track segment irradiation of the cell per passage.

The previous Monte Carlo methods described in Chapter 8 were employed to simulate lithium ions and alpha particle tracks in semi-stochastic geometries representative of cell monolayers and suspension irradiations, incubated in a medium with 50µg/g boric acid. The microdosimetric single event results have been used to feed into Charlton's model and calculate survival curves.

Using the calculated chord lengths and track averaged LETs of the particles from simulations, for any given traversal of the cell nucleus, the equivalent specific lethal dose

(D_0) was found from track segment irradiations. This was then used to calculate the probability of the cell surviving any given passage. The product of all cell passages allow the probability of single cell survival to be calculated and averaging over the population allows population survival curves to be determined.

Calculations were carried out for both monolayers and suspensions over a range of doses leading to markedly different survival curves. The results of the simulations can be seen in figure 9.2, where the blue and dark red lines show survival data calculated from track simulations, the black symbols show Birmingham mixed field experimental data (where the majority of the dose is delivered by the boron reaction) and the lighter red line a best fit to the experimental data.

For the same given macroscopic neutron fluence, monolayer cells see a reduction in boron dose compared to the identical cell line grown in suspension. This is due to two main factors, one being the inhomogeneity caused by growing the cells on the medium boundary (the mylar base/wall) – which has no boron beyond it, the other being the observable difference in cell morphology between suspended and monolayer cells and their nuclei. This observed survival discrepancy being the primary reason for introducing the absorbed fraction correction factor of previous chapters.

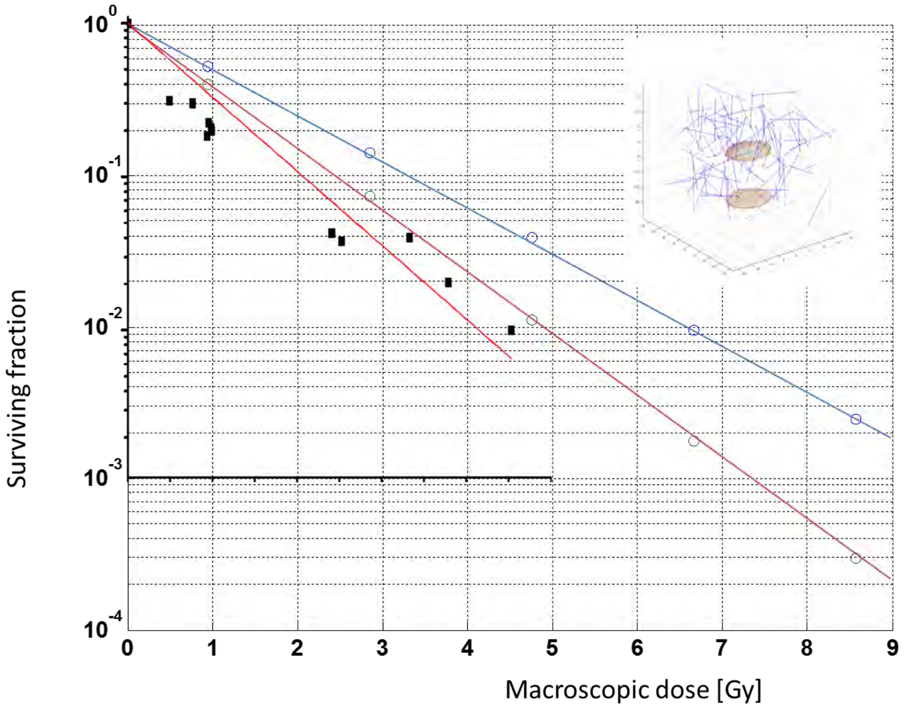

Figure 9.1 Calculated survival curves for cell suspension (dark red) and cell monolayer (blue) Li/alpha irradiations.

That said, a systematic under prediction of calculated survival is observed when compared to measured survival. It is plausible that this underestimate stems from the assumptions used in these survival calculations that lithium particles would behave and have the same cell killing effect as alpha particles for which specific lethal doses are known. This is readily seen in figure 9.3, where it has been shown [28] that lithium RBEs are most likely higher than those of alpha particles and were our lithium particles treated with higher cell kill effects the survival curves would indeed be much steeper.

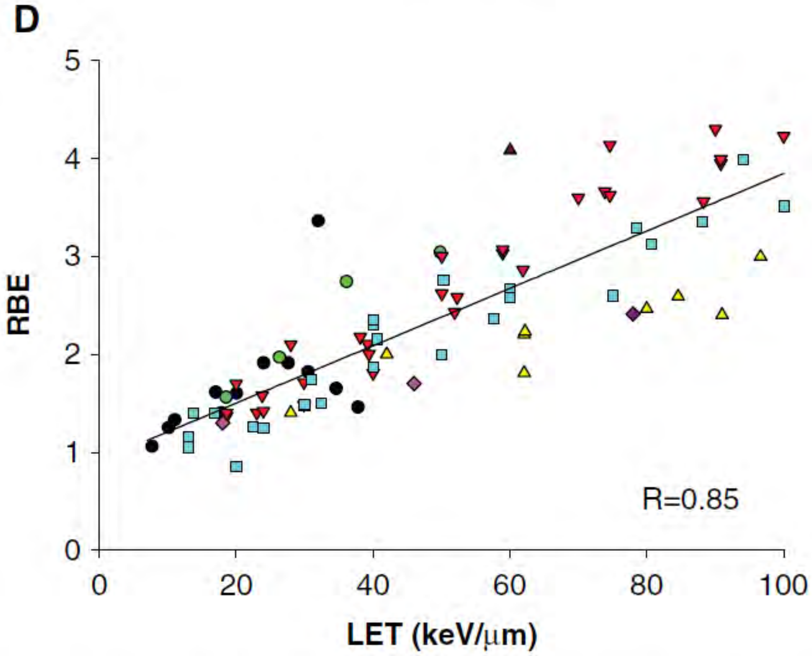

Figure 9.3 comparison of RBE values for V79 cells from different incident particle beams as a function of LET. [The upward point red triangle being a lithium ion RBE].

This remains a matter for future work and is an aside to the main subject matter of the thesis.

Chapter 10

SUMMARY AND CONCLUSION

The aims of the current study were to carry out fundamental reference dosimetric measurements and calculate macroscopic and microscopic correction factors for cell survival experiments in order to aid the development of a cell-based radiobiology protocol to provide essential data on the safety and efficacy of epithermal neutron beams for BNCT in advance of clinical trials.

In order to achieve stable and reproduceable beam measurements and delivery, work was carried out at the University of Birminghams BNCT facility to relocate two neutron monitor chambers (^{235}U fission chambers - Centronic Ltd.). The revised monitor positions were chosen following detailed consideration of sensitivity to backscattered radiation and detector count-rate. Detailed design calculations were reported utilising MCNPX and experimental validation of final detector count rates and neutronic coupling presented.

The original monitor chamber position was separated from the patient/phantom by 20 mm of Li-polyethylene, as chambers were located in the back of the 25 mm Li-polyethylene beam delimiter, adjacent to the graphite neutron reflector. Experimental coupling with the chambers in this position was measured to be 2.3 ± 0.2% with the LWT, and the corresponding MCNPX simulated prediction being 2.6 ± 1%.

Changing the monitor position to be centered within the Li-polyethylene delimiter, separated from the patient/phantom by 12 mm Li-polyethylene (instead of 20 mm) was predicted by MCNPX to reduce the count-rate by a factor of 2.5 ± 0.1. This was verified experimentally to be a factor of 2.4 ± 0.1, producing typical detector count-rates at 1 mA proton current of approximately 4000 cps. This change of position was predicted to increase the phantom coupling to 3.9%, which has been verified experimentally to be less than 4%.

With stabilished beam monitors, good historic data and a regular calibration procedure much more confidence can be placed in the nominal intensity and spectra of the beam for both experimental and clinical work conducted.

10.1 Foil self shielding correction factors

Self-shielding correction factors for metal foils used to determine boron and nitrogen kerma by activation analysis have been evaluated by simulation in MCNPX. Correction factors were calculated for two types of foil, one set being non-dilute (solid/metallic) foils of Au and Mn/Ni, the other being dilute foils of 1% Mn or Au in Al. The non-dilute gold foils exhibit the largest flux depression, perturbing the flux by as much as 80% at shallow depths and 30% at depths approaching 10 cm. The non-dilute Mn/Ni foils cause a 5-10% perturbation at various depths along the central axis of the phantom. Experimental data is presented to validate these simulation results. Further simulations show that the dilute foils, both MnAl and AuAl, perturb the field by less than 1%.

Previous work (Culbertson et al. [7]) had reported correction factors of 5.5% for non-dilute Mn foils and 17.5% for non-dilute Au foils. This work also suggested that correction factors do not change significantly with depth. These results are now superceded by the current work, where for Mn the correction factor is approximately 6.5% near the beam entrance (up to 4 cm deep) rising to 10% at the brain midline (7 cm). For Au the correction factors are up to 80% at 2 cm deep falling to 30% at the brain midline. Experimentally determined correction factors for non-dilute foils show extremely good agreement with those simulated. When using such non-dilute paired foils for dosimetry these correction factors cause a small but important correction to the derived nitrogen and boron dose components. Further simulations show that the perturbation by the neutron flux for dilute foils is negligible and hence these foils are water equivalent.

Dilute foils containing 1% by mass of gold and manganese in aluminium were used to derive boron and nitrogen dose components on the central axis beam of a Large Water Tank (LWT). following the spectral indices method [9].

A normalisation factor of 0.83 is used to scale calculations to measurements and is applied to all calculated dose components. Paired magnesium and A150 tissue equivalent ionisation chambers (Exradin M2 and T2) were used with argon and methane-based tissue equivalent gas respectively to determine fast neutron and photon dose components.

BNCT beam dosimetry is complex and standard methods (foils and ionisation chambers) lead to assessment of photon and fast neutron dose components with large uncertainties. In such situations it is essential to use supplementary techniques to validate the standard methods.

The chosen supplementary method applied was the A150 tissue equivalent proportional counter (TEPC), for the thermal and fast neutron components. The thermal neutron doses derived from the Freudenreich spectral indices method were compared with those derived from the TEPC from depths of approximately 3cm to 8cm. The maximum difference measured was 15%, with an average difference of 7%.

10.2 Cell Dosimetry

Cell radiobiology experiments have been carried out to perform dose response studies over a range of doses, ^{10}B concentrations, dose rates and depths found in clinical practice in both accelerator and reactor driven systems.

An extensive radiobiological programme has been conducted by the University of Birmingham BNCT group and collaborating institutions. One of the prime objectives of this collective work remains the production of a validated protocol for the pre-clinical biological characterisation of BNCT facilities and for this to be established internationally and utilised at all BNCT facilities.

The aim of this study was to quantify the doses, both macroscopic and microscopic, observed during the irradiations of cell monolayers at the University of Birmingham's 2.8MeV Dynamitron particle accelerator and at the MIT research reactor.

Calculating the correct physical dose is absolutely essential in assessing damage to critical biological structures and their survival probabilities during cell irradiations. It is the core of the fundamental radiobiology work and underpins translational studies in differing beams.

Cells are typically grown as densely packed monolayers on the beam facing wall of a T-25 Falcon (polyethylene) flask, covering an area equal to 6cm by 5cm, perpendicular to the beam direction and at depths of 2cm and 5cm. The flasks contain a cell growth medium in addition to 50µg/g of ^{10}B (in the form of boric acid).

There are numerous factors which complicate the calculation of dose in small, cell like, volumes including, the thermalisation of the impinging epithermal beam and its subsequent spectral and dose rate shift. This results in a non-uniform distribution of neutron fluence and spectra across the cell monolayer.

Two sets of major corrections need to be applied to dose calculations based on beam specific, on-axis depth dose curves (derived from fluence to dose kerma factors):

1. Macroscopic Corrections

    - The flasks in which the V79 cells are irradiated occupy a finite profile in the phantom. This necessitates the correction for the drop off in the dose components perpendicular to the beam central axis. These dose correction factors are loosely termed off-axis correction factors.

    - Perturbation of neutron flux by the presence of the boronated medium.

2. Microscopic Corrections

    Two large micro-dose corrections are needed in the mixed field of a BNCT beam impinging on boron loaded cell monolayers. These are:

- The boron dose

- The thermal neutron dose – due to neutron capture in nitrogen.

The primary cause for these microscopic inhomogeneities and the resultant non-charged particle equilibrium is the non-uniform distribution of these elements across the cell monolayer and its neighbouring environment.

These correction factors have been calculated for the Birmingham beam and applied to the Birmingham dose rate experiments carried out at MIT, which serve as a dosimetric methodology for future radiobiology work in other beams.

Paired (dilute) gold and manganese foils along with Mg/Ar and TE ion chambers measurements have been used to calculate boron, thermal neutron, fast neutron and photon doses, at several depths in a standard large water tank (LWT). In the case of the Birmingham facility the Monte Carlo code MCNPX was used to calculate off-axis correction factors to the central depth dose curve for the Birmingham beam. Integrating the dose (normalised to experimental measurements) over the flask area and dividing by the central axis depth dose serves as an off-axis dose correction at the two depths. The maximum off-axis correction is for the thermal and boron dose components at 2cm and is calculated to be 3.5%.

As well as off-axis dose corrections, the flasks also perturb the flux that passes through them by virtue of the medium being loaded with 50µg/g of boron. Perturbation factors were calculated for the Birmingham beam using MCNPX. The perturbation calculated for the flask monolayer, 1mm deep under the front face of the flask (where the cells are fixed), at the two depths at which irradiations were carried out. The second flask is evidently much more perturbed than the first, with thermal neutron perturbations reaching up to 15% at the centre of the front surface of the flask.

The location and micro-distribution of the boron atoms and their decay is of critical importance in assessing local dose delivered to the cell nucleus. In the case of the present study using boric acid mediated cell irradiations, the boron is believed to be uniformly distributed throughout the cells and the medium in which they are grown i.e. within the flasks. However, as the cells are grown on the flask wall the cells see a large local inhomogeneity in source distribution at one face of the monolayer plane.

Cells grown in monolayers take on a very different morphology to cells grown in suspension and take the form of closely packed oblate spheroids. In order to factor in this known cell morphology coupled with an inhomogeneous boron source distribution Monte Carlo methods were employed to simulate particle tracks in semi-stochastic cell geometries – sampled from distributions generated from confocal microscopy images. The Monte Carlo transport code

SRIM was used to calculate the range and LET of these light ions in biologically equivalent tissue/medium. These simulated back to back tracks can, for the purpose of simplicity, be considered a single track with a varying LET along its length, which is identical to the two individual tracks placed back to back.

Mathematically these ellipsoidal ‘nuclei’ were described in vector notation and solved for line intersection using Matlab™ - in a vectorised matrix algebra environment.

Results of simulations show boron doses calculated in inhomogeneously boron loaded cell irradiations, carried out at MIT and Birmingham BNCT facilities, require corrections for dose absorbed fraction, a microdosimetric quantity related to the local boron distribution in and around the cells. Detailed calculations show an absorbed fraction of 0.77±0.05.

Work was carried out at the Birmingham BNCT facility to validate the absorbed dose fractions to cells irradiated in monolayers and exposed to a non-uniform distribution of boron in the surrounding medium. Glass dishes, commonly known as ‘jelly fish’ dishes, were paired back to back with cells grown on a layer of mylar sandwiched between the two dishes and the sides sealed. Experiments show absorbed fractions of 0.73 – 0.74. Cell experiments have in themselves large systematic uncertainties – and in this case no repeat measurements were carried out.

The capture of thermal neutrons in nitrogen, $^{14}N(n,p)^{14}C$, results in a recoil proton carrying 580keV of the energy and a carbon ion carrying 42keV. The recoil proton and carbon ion have ranges in water of ~10µm and 0.23µm respectively, the proton range being comparable to the lithium/alpha range but with wider lateral straggling.

In the case of the present study, boric acid contains no nitrogen, neither the polyethylene T25 flasks, on which the cells are plated and irradiated contain any nitrogen. The medium in which the cells are irradiated, in the presence of 50ppm boric acid, contains 0.012% by weight nitrogen, the added 10% by weight bovine foetal calf serum – contains approximately 1% by weight nitrogen. Thus the only major nitrogen component of the nitrogen-thermal neutron dose is the cells themselves (1.7% by weight nitrogen) and the aggregate medium, ~0.11% by weight nitrogen.

A 3 x 3 cell monolayer array was used to simulate observed nitrogen distributions in the V79 cells and extracellular space. Cells sizes are sampled as in the boron case, but have additional degrees of freedom factoring in the packing density between cells and lateral freedom taking into account the variable location of the nucleus within the cell.

The results of stochastic cell simulations show that for an inhomogeneous nitrogen dose distribution the population absorbed fraction to the nucleus is 0.48±0.02.

As a final point, a dosimetric procedure is described in order to aid the development of a cell-based radiobiology protocol to provide essential data on the safety and efficacy of epithermal neutron beams for BNCT in advance of clinical trials.

For the same given macroscopic fluence, monolayer cells see a reduction by a factor of 0.77±0.05 in boron dose compared to the identical cell line grown in suspension. The thermal neutron nitrogen dose is reduced by a factor of 0.48± 0.02 compared to a uniform nitrogen distribution.

Survival curves plotted with all the dose correction factors applied show excellent agreement with the biological effect models reported in the literature.

References

[1] Durisi, E., Zanini, A., Manfredotti, C., et al. (2007) Design of an epithermal column for BNCT based on D-D fusion neutron facility. *Nuclear Instruments and Methods in Physics Research Section A: Accelerators, Spectrometers, Detectors and Associated Equipment,* 574: (2): 363-369.

[2] Allen, D.A. and Beynon, T.D. (1995) A design study for an accelerator-based epithermal neutron beam for BNCT. *Physics in Medicine and Biology,* 40: (5): 807.

[3] D. A. Allen and T. D. Beynon, „What is the best proton energy for accelerator-based BNCT using the ^{7}Li(*p,n*)^{7}Be reaction?‟, *Medical Physics*, 2000, Vol. **27**, No. 5.

[4] C. L. Lee and X.-L. Zhou, „A Monte Carlo dosimetry-based evaluation of the ^{7}Li.p,n.^{7}Be reaction near threshold for accelerator boron neutron capture therapy‟, *Med. Phys*., January 2000, vol. **27**, Issue 1.

[5] J. F. Ziegler. SRIM-2003. *Nuclear Instruments and Methods in Physics Research Section B*: Beam Interactions with Materials and Atoms, 219-220:1027-1036, 2004. doi: DOI: 10.1016/j.nimb.2004.01.208.

[6] M. V. Bokhovko, W. T. Chu, I. A. Gulidov, O. E. Kononov, V. N. Kononov, V. V. Korobeynikov, D. W. Nigg, A. N. Soloviev and A. S. Sysoev, „Optimization of an accelerator-based epithermal neutron source for neutron capture therapy‟, *Applied radiation and isotopes*, 2004, **61**, p.1009-1013.

[7] Culbertson, C. N., Green, S., Mason, A. J., Picton, D., Baugh, G., Hugtenburg, R. P., Yin, Z., Scott, M. C., and Nelson, J. M., In-phantom characterisation studies at the Birmingham Accelerator-Generated epithermal Neutron Source (BAGINS) BNCT facility, *Applied radiation and isotopes*, 2004, 61, p.733-738.

[8] Campbell J and Scott M. C., Scientific and Industrial Applications of Small Accelerators, 4th Conf., Denton,TX, 1976

[9] Freudenreich, W.E., Empirical relations between reaction rates of monitors activated in BNCT beams, *NRG report* 21425/03.55288, Petten, 2003.

[11] Negoita, CC, 2004, “Measurement of Neutron Flux Spectra in a Tungsten Benchmark by Neutron Foil Activation Method”, PhD thesis, Universität Dresden.

[12] Rogus, R. D., O. K. Harling, et al. (1994). "Mixed field dosimetry of epithermal neutron beams for boron neutron capture therapy at the MITR-II research reactor." *Medical Physics,* 21(10): 1611-25.

[13] Shcherbakov, O. and Harada, H. (2002) Resonance Self-Shielding Corrections for Activation Cross Section Measurements. *Journal of Nuclear Science and Technology,* 39: (5): 548-553.

[14] Goorley, J.T., Kiger Iii, W.S. and Zamenhof, R.G. (2002) Reference dosimetry calculations for neutron capture therapy with comparison of analytical and voxel models. *Medical Physics,* 29: (2): 145-156.

[15] Turki Ibrahimi, MSc University of Birmingham, Microdosimetry in a BNCT Beam, 2012.

[16] Taylor, GC, 1990, “The Prediction and Measurements of Microdosimetric Spectra relating to Neutron Cancer Therapy”, PhD thesis, University of Birmingham.

[17] Helen Howard, MSc University of Birmingham, Microdosimetry in BNCT, 2003.

[18] K.J. Riley, P.J. Binns and O.K. Harling, “Performance characteristics of the MIT fission converter based epithermal neutron beam,” *Phys. Med. Biol.* **48** pp. 943-958, 2003.

[19] Ben Phoenix, 2012, 'Dose Effects in Boron Neutron Capture Therapy', PhD thesis, University of Birmingham.

[20]] K.J. Riley and P.J. Binns, „Dosimetry Measurements in the FCB for Treatment Planning Validation,‟ MIT Nuclear Reactor Laboratory Technical Report, 2002.

[21] Glenn F. Knoll, Radiation Detection and Measurement, Third Edition, J. Wiley (January 5, 2000).

[22] EU Dosimetry protocol. Petten, 2003. Recommendations for the Dosimetry of Boron Neutron Capture Therapy (BNCT), 21425/03.55339/C.

[23] Charlton, D. E., A. I. Kassis, et al. (1994). "A Comparison of Experimental and Calculated Survival Curves for V79 Cells Grown as Monolayers or in Suspension Exposed to Alpha Irradiation from 212Bi Distributed in the Growth Medium." *Radiation Protection Dosimetry* 52(1-4): 311-315.

[24] Hill, M. A., M. D. Vecchia, et al. (1998). "Production and dosimetry of copper L ultrasoft x-rays for biological and biochemical investigations." *Physics in Medicine and Biology, 43*(2): 351.

[25] Neti, P. V. S. V. and R. W. Howell (2006). "Log Normal Distribution of Cellular Uptake of Radioactivity: Implications for Biologic Responses to Radiopharmaceuticals." *Journal of Nuclear Medicine*, *47*(6): 1049-1058.

[26] Chung, Y 2008, "Radiobiological Evaluation of New Boron Delivery Agents for Boron Neutron Capture Therapy", PhD thesis, Massachusetts Institute of Technology.

[27] Detlef Gabel, Ralph G. Fairchild, Börje Larsson and Hans G. Börner. "The Relative Biological Effectiveness in V79 Chinese Hamster Cells of the Neutron Capture Reactions in Boron and Nitrogen." *Radiation Research*, Vol. 98, No. 2 (May, 1984), pp. 307-316

[28] Sorensen, B. S., J. Overgaard, et al. (2011), "In vitro RBE-LET dependence for multiple particle types." *Acta Oncologica*, *50*(6): 757-762.

[29] ICRU report #36,. *Microdosimetry* (International Commission on Radiation Units and Measurments, Bethesda, MD, 1983).

[30] Eckerman KF, Ryman JC, Taner AC, Kerr GD. Traversal of cells by radiation and absorbed fraction estimates for electrons and alpha particles. In: Schlafke-Stelson AT, Watson EE, eds. Proceedings of the Fourth International Radiopharmaceutical Dosimetry Symposium. Oak Ridge, Tennessee; Oak Ridge Associated Universities; 1985:67–81.

[31] M. Kellerer, "Chord length distributions and related quantities for spheroids," *Radiat. Res.*,vol. 98, pp. 425-437, 1984.

[32] White, SM 2001, "Biological Dosimetry of Neutron Beams for Neutron Capture Therapies", PhD thesis, Massachusetts Institute of Technology.

[33] Mason, A. J., V. Giusti, et al. (2011) "Interaction between the biological effects of high- and low-LET radiation dose components in a mixed field exposure." *International Journal of Radiation Biology*, *87*(12): 1162-1172.

[34] Yam, C. S. and R. G. Zamenhof (2000). "Computational validation of the stereology principle applied to the microdosimetry of boron neutron capture therapy." *Medical Physics, 27*(3): 549-557.

[35] MATLAB version 6.5.1. Natick, Massachusetts: The MathWorks Inc., 2003.

[36] Rogus, RD. 1994, "Design and Dosimetry of Epithermal Neutron Beams for Clinical Trials of Boron Neuton Capture Therapy at The MITR-II Reactor", PhD thesis, Massachusetts Institute of Technology.

[37] arXiv:nucl-ex/0202004v1

[38] Deconninck, G. and Demortier, G. (1972). "Quantitative analysis of aluminium by prompt nuclear reactions," *Journal of Radioanalytical and Nuclear Chemistry*, *12*(2): 189-208.

[39] "Surface Characterization and Corrosion Behaviour of Ti Based Alloys in Fetal Bovine Serum," U.P.B. Sci. Bull., Series B, Vol. 71, Iss. 4, (2009) ISSN 1454-2331.

[40] Schettino, G., M. Folkard, et al. (2003). "Low-Dose Studies of Bystander Cell Killing with Targeted Soft X Rays." Radiation Research 160(5): 505-511.

[41] Culbertson et al. (2003) "Energy Calibration of the 3 MV Dynamitron Accelerator at Birmingham." *Proceedings of international workshop on Neutron capture therapy* : state of the art, and 3rd Young members neutron capture therapy meeting : Pisa (Italy).

[42] Burmeister, J., Riley, K., Coderre, J.A., et al. (2003) "Microdosimetric intercomparison of BNCT beams at BNL and MIT." *Medical Physics*, 30: (8): 2131-2139.

[43] Michael A. Davis, John B. Little, K. M. M. S. Ayyangar and A. R. Reddy. "Relative Biological Effectiveness of the 10B(n,alpha)7Li Reaction in HeLa Cells." *Radiation Research*, Vol. 43, No. 3 (Sep., 1970), pp. 534-553.

Appendix A: Conference Proceedings and Publications

1. Neutron self-shielding effects and correction factors for foil activation measurements used in BNCT dosimetry

Z. Ghani[a], S. Green[a,b], C. Wojnecki[a,b]

[a] *School of Physics and Astronomy, University of Birmingham, United Kingdom*

[b] *Department of Medical Physics, University Hospital Birmingham, United Kingdom*

Abstract

Self-shielding correction factors for metal foils used to determine B and N kerma by activation analysis have been evaluated by simulation in MCNPX. Correction factors were calculated for two types of foil, one set being non-dilute (solid/metallic) foils of Au and Mn/Ni, the other being dilute foils of 1 % Mn or Au in Al. The non-dilute gold foils exhibit the largest flux depression, perturbing the flux by as much as 80 % at shallow depths and 30 % at depths approaching 10 cm. The non-dilute Mn/Ni foils cause a 5-10 % perturbation at various depths along the central axis of the phantom. Experimental data is presented to validate these simulation results. Further simulations show that the dilute foils, both MnAl and AuAl, perturb the field by less than 1 %.

2. BNCT beam monitoring, characterisation and dosimetry

Z. Ghani[a], S. Green[a,b], C. Wojnecki[a,b], R. P. Hugtenburg[c]

[a] *School of Physics and Astronomy, University of Birmingham, United Kingdom*

[b] *Department of Medical Physics, University Hospital Birmingham, United Kingdom*

[c] *School of Medicine, University of Swansea, United Kingdom*

Abstract

Work has been recently carried out at the University of Birmingham Neutron Capture Therapy facility to relocate two neutron monitor chambers (^{235}U fission chambers - Centronic Ltd.). IEC requirements for monitoring radiotherapy beams require the chamber to be in the 'treatment' beam. The problem then arises of neutrons backscattering from patient or phantom affecting the counts at these detectors which are to be located within a 25 mm layer of Lithium polyethylene shielding surrounding the exit port of the treatment facility. The revised monitor position was chosen after detailed consideration of sensitivity to backscattered radiation and detector count-rate. Detailed design calculations with MCNPX are reported and experimental validation of final detector count rates and neutronic coupling presented.

3. **Design study to further optimise the Birmingham orthogonal accelerator epithermal neutron beam**

Z. Ghani[1], S. Green[2], C. Wojnecki[2]

[1] School of Physics and Astronomy, University of Birmingham, United Kingdom

[2] Department of Medical Physics, University Hospital Birmingham, United Kingdom

Abstract

A detailed study has been carried out on comparing various moderator and reflector materials in order to quantify any improvements that can be made to the current Birmingham facility.

The motivation for optimising and re-modelling the treatment facility was to maximize the dose to tumour tissue while keeping the weighted dose to healthy brain tissues below 12.5 Gy. Five key indices were calculated for three moderator materials (Fluental, MgF_2 and Teflon) and two reflector materials (Graphite and Lead):

1. Treatment Time
2. Therapeutic Ratio (TR) at 6.5cm into the brain
3. Max TR is the ratio of Maximum Tumour Dose to Maximum Tissue Dose
4. Advantage Depth (AD) and
5. Skin dose

Changing the graphite reflector to one made of lead (for 25 cm Fluental moderator) delivered a substantial improvement. It resulted in an increase in beam quality in terms of Therapeutic Ratio and AD. The AD increased from 9.1 to 9.8 ±0.1cm, the TR at 6.5 cm deep from 2.23 to 2.75 and the max TR from 5.34±0.05 to 5.40±0.05, with a 10 % reduction in treatment time from 198 minutes to 176 minutes.

In order to increase the dose rates obtained with the MgF_2 moderator / lead reflector, and thus reduce the treatment time, it becomes necessary to compromise beam quality. By moving to a shorter moderator depth of 18.1 cm treatment time was brought down from 258 minutes to 146 minutes. The change in other key indices being AD from 9.1±0.1 to >10cm, the TR from 2.23 to 2.76 and the max TR from 5.34 ±0.05 to 5.26 ±0.03 when compared to the current facility.

Further calculations will be presented to show that the addition of a Li-Si filter does not affect our choice of the optimum length of moderator and reflector, and to quantify the effect of an additional patient collimator on beam performance indices.

4. Improving Time Course Predictions Of Boronophenylalanine (BPA) Uptake In Brain Tumours

Z. Ghani[1], A. Detta[2], G. S. Cruickshank[2], S. Green[1, 3], C. Wojnecki[1, 3], A. Boddy[5], D. Ngoga[2], T. Sheehan[4], N. D. James[1], J. Doran[1], J. Hardie[1], M. Chester[1], N. Graham[1], G. Halbert[6], M. Elliot[6], S. Ford[6], R. Braithwaite[4], J. Vickerman[7], N. Lockyer[7], G. Croswell[8], A. Chopra[8] and R. Sugar[8]

[1] *School of Physics and Astronomy, University of Birmingham, UK*

[2] *Department of Neurosurgery, University Hospital Birmingham, UK*

[3] *Department of Medical Physics, University Hospital Birmingham, UK*

[4]*Regional Laboratory for Toxicology, Sandwell & West Birmingham Hospitals Trust, UK*

[5]*Northern Institute for Cancer Research, University of Newcastle, Newcastle-Upon-Tyne, UK*

[6]*CR-UK Formulation Unit, University of Strathclyde, Glasgow, UK*

[7]*Surface Analysis Research Centre, The University of Manchester, Manchester, UK*

[8]*CR-UK Drug Development Office, London, UK.*

Introduction: BNCT delivery is frequently conducted based on assumed boron levels in tumour and their time course. Boron levels are approximated to be ~15ppm and ~52.5ppm in healthy tissue and tumour respectively. A great deal of effort is expended in calculating ideal treatment plans, field directions and timings to maximise patient benefit. No treatment planning to date factors in the patients' propensity to take up boronophenylalanine (BPA) into tumours at varying levels. A cell-level pharmacokinetic model is proposed to provide predictive time course information on BPA levels in blood, tumour tissue and healthy tissue.

Materials and Methods: A physiologically relevant cell-level mathematical model incorporating phase 1 clinical trial data, comprising of post infusion, time course levels of BPA in blood, extracellular fluid (ECF), tumour biopsies, debulked tumour and urine has been constructed for each of the first 6 patients inducted in the University Hospital Birmingham's clinical drug study. Two cohorts of patients had BPA administered intravenously, with and without a mannitol bolus, at 350mg/kg over 120 minutes. Blood, urine and ECF levels were sampled periodically, tumour and brain-around-tumour biopsies were also taken. A modelling approach has been developed to correlate BPA uptake to the expression of the LAT-1 transporter which is critical in BPA uptake in both tumour and healthy tissue. This model will be incorporated into a modified two compartmental open pharmacokinetic model and will also factor in varying levels of LAT-1 density.

Results and Discussions: ^{10}B levels in blood peaked at 25.7 and 42.2mg/kg for the two cohorts. Mean model rate constants for a two compartmental open model fitted to the time course of ^{10}B concentration in blood were k_{12}, k_{21}, k_{10} of 0.0117, 0.0061, 0.0039 for cohort I, and 0.0201, 0.0078 and 0.0072 for cohort II, respectively. Volumes of distribution for the central compartments (V1) were calculated to be 0.296 and 0.161 L/kg respectively. LAT transporter profiles are currently being quantified and will be incorporated in the more detailed kinetic model by iterative modelling.

5. Assessing The Impact Of Treatment Room Shielding On Dose To Critical Organs From Scattered Radiation

Z. Ghani[1], G. Hall[1], S. Green[1, 2] and C. Wojnecki[1, 2]

[1] *School of Physics and Astronomy, University of Birmingham, United Kingdom*

[2] *Department of Medical Physics, University Hospital Birmingham, United Kingdom*

Introduction: The existing University of Birmingham's, experimental, BNCT treatment facility has been re-evaluated using Monte Carlo simulations to assess the impact of further neutron shielding materials on the walls and ceiling of the treatment room and whether or not they can potentially reduce patient dose to vital organs from scattered radiation.

Materials and Methods: The 3MV Dynamitron accelerator - based treatment facility was simulated using the MCNPX radiation transport code. A 4mm voxelised whole body human phantom (VIP man) was used to assess neutron and photon doses delivered to 62 organs defined in the material description of the phantom. The simulations were carried out with the phantom positioned at the end of the beam shaping assembly. Scattered radiation from walls and ceiling was flagged to identify the dose to organs from the primary beam and that which contributed from scatter via walls or ceiling. Simulations were repeated with 5cm thickness Premadex® neutron shielding on the walls and ceiling of the treatment room and the changes in dose rate were assessed.

Results and Discussions: Adding neutron shielding materials to the walls of the treatment room reduced the calculated scattered dose to each and every organ in the voxelised phantom. The fraction of the scattered dose was reduced by different extents depending on the location and size of the organ. Shielding only the walls led to an average decrease in scattered neutron contribution to the total dose of ~ 25%. An average decrease in dose of 8% and decrease in dose to the lungs of 3.6% was calculated.

The effect of shielding the walls and ceiling compared to the current room showed an average decrease in scatter of approximately 50% with an average decrease in dose of 12%, the largest decreases being seen in the testes, prostate and urinary bladder. The decrease in the dose to the lungs with walls and ceiling shielded was shown to be 6% when compared to the existing facility.

List of publications:

1. Minsky, D. M., A. A. Valda, et al. "First tomographic image of neutron capture rate in a BNCT facility." Applied Radiation and Isotopes **69**(12): 1858-1861.

2. Minsky, D. M., A. A. Valda, et al. (2009). "Experimental feasibility studies on a SPECT tomograph for BNCT dosimetry." Applied Radiation and Isotopes **67**(7â€“8, Supplement): S179-S182.

3. Minsky, D. M., A. Valda, et al. "Progress In The Development Of A Tomographic SPECT System For Online Dosimetry In BNCT." AIP Conference Proceedings **1265**(1): 415-418.

4. Cruickshank, G. S., D. Ngoga, et al. (2009). "A cancer research UK pharmacokinetic study of BPA-mannitol in patients with high grade glioma to optimise uptake parameters for clinical trials of BNCT." Applied Radiation and Isotopes **67**(7â€“8, Supplement): S31-S33.

5. Roca, A., Y.-H. Liu, et al. (2009). "A preliminary inter-centre comparison study for photon, thermal neutron and epithermal neutron responses of two pairs of ionisation chambers used for BNCT." Applied Radiation and Isotopes **67**(7â€“8, Supplement): S134-S136.

6. Cellular ^{10}Boron visualisation and microdosimetry in human glioblastoma: bases for improving boron neutron capture therapy

Allah Detta[1], Nicholas P. Lockyer[2], Alessia Longobardo[2], John C. Vickerman[2] ,W. S. Kiger III[3], Xing-Qi Lu[3], Zamir Ghani[4], Stuart Green[5], Garth S. Cruickshank[1]

[1]Department of Neurosurgery, Queen Elizabeth Hospital Birmingham, Edgbaston, Birmingham B15 2TH and the School of Cancer Sciences, College of Medicine & Dentistry, The University of Birmingham, B15 2TT, UK.

[2]Surface Analysis Research Centre, Manchester Interdisciplinary Biocentre & School of Chemical Engineering & Analytical Science, The University of Manchester, Manchester M1 7DN, UK.

[3]Department of Radiation Oncology, Beth Israel Deaconess Medical Center, Harvard Medical School, Boston, Massachusetts 02215, USA.

[4]School of Physics and Astronomy, University of Birmingham, Birmingham, UK,

B15 2TT.

[5]Hall-Edwards Radiotherapy Research Group, Department of Medical Physics, University Hospitals Birmingham NHS Trust, Edgbaston, Birmingham, B15 2TH, UK.

ABSTRACT:

Boron neutron capture therapy (BNCT) is an experimental radiation therapy for cancer which allows dose escalation and may therefore improve treatment outcome. The determination of the intracellular location of the boron atom —which largely dictates the site of damage and is a major determinant of BNCT effectiveness —is a fundamental biological challenge that has checked the clinical progress of this therapy. Here we show, using biopsies *ex vivo*, morphological ^{10}B visualisation, measurement and derivation of attendant biological microdosimetry following specific boronophenylalanine (BPA) accumulation in human glioblastoma-related tissue. Secondary ion mass spectrometry (SIMS) analysis of imprinted biopsies revealed highly diffusible inorganic ions such as K^+ and, importantly, $^{10}B^+$ localised on the cellular scale. Boron density was 2.4× higher in the tumour compared with brain-around-tumour (BAT) samples and the boron was found compartmentalised intra- and extra-cellularly at a ratio of ~2 in both. Microdosimetry simulations based on the boron microdistributions measured using SIMS yielded effective energy deposition, although there was a 2.4 fold increase in the mean specific energy in the tumour cells compared with BAT (20.7 ± 5.5 Gy *vs*

8.5 ± 3.4 Gy), and cell survival curves that were separated by more than 3 decades of cell killing for the same neutron fluence. This study provides a basis for a new approach to evaluate the effectiveness of BNCT.

7. The Birmingham Boron Neutron Capture Therapy (BNCT) project : developments towards selective internal particle therapy

Green, S. and Phoenix, B. and Mill, A. J. and Hill, M. and Charles, M. W. and Thompson, J. and Jones, B. and Ngoga, D. and Detta, A. and James, N. D. and Doran, J. and Graham, N. and Ghani, Z. and Wojnecki, C. and Halbert, G. and Elliott, M. and Ford, S. and Sheehan, T. M. T. and Vickerman, J. and Lockyer, N. and Croswell, G. and Boddy, A. and King, A. and Cruickshank, G. S. (2011) *The Birmingham Boron Neutron Capture Therapy (BNCT) project : developments towards selective internal particle therapy.* Clinical Oncology, 23 (3). S23-S24. ISSN 0936-6555

Full text not available in this repository. (Request a copy from the Strathclyde author)

Official URL: http://dx.doi.org/10.1016/j.clon.2011.01.378

Abstract

This paper will review progress on two aspects of the Birmingham BNCT project. Firstly on evaluation of the effects of high and low LET radiations when delivered simultaneously, and secondly on attempts to optimise delivery of the boron carrier compound BPA through pharmacokinetic studies. Simultaneous or non-simultaneous irradiations of V79 cells with alpha-particle and X-ray irradiations were performed. Alpha doses of 2 and 2.5 Gy were chosen and the impact on survival when delivered separately or simultaneously with variable doses of X-rays was evaluated. The pharmacokinetics of the delivery of a new formulation of BPA (BPA-mannitol) are being investigated in brain tumour patients through a study with 2 × 2 design featuring intravenous and intracarotid artery infusion of BPA, with or without a mannitol bolus. On the combined effect of low and high LET radiations, a synergistic effect was observed when alpha and X-ray doses are delivered simultaneously. The effect is only present at the 2.5 Gy alpha dose and is a very substantial effect on both the shape of the survival curve and the level of cell killing. This indicates that the alpha component may have the effect of inhibiting the repair of damage from the low LET radiation dose delivered simultaneously. On the pharmacokinetics of BPA, data on the first three cohorts indicate that bioavailability of BPA in brain ECF is increased substantially through the addition of a mannitol bolus, as well as by the use of intracarotid artery route of infusion. In both cases, for some patients the levels after infusion approach those seen in blood, whereas the ECF levels for intravenous infusion without mannitol are typically less than 10% of the blood values.

Appendix B:

Design study to further optimise the Birmingham orthogonal accelerator epithermal neutron beam

Design Study to Further Optimise the Birmingham Orthogonal Accelerator Epithermal Neutron Beam

Z. Ghani[a], S. Green[a,b], C. Wojnecki[a,b], R. P. Hugtenburg[c]

a School of Physics and Astronomy, University of Birmingham, United Kingdom
b Department of Medical Physics, University Hospital Birmingham, United Kingdom
c School of Medicine, University of Swansea, United Kingdom

Beam Shaping Assembly

Extensive modelling work has been carried out using the Monte Carlo transport code MCNPX. Published findings indicate that MgF_2 might, perhaps, serve as a better moderating material in accelerator driven systems over other materials more commonly used. Various moderator and reflector materials have been assessed for their impact on improved therapeutic depth dose profiles.

The current Birmingham facility has a 25.1cm FLUENTAL™ moderator, which provides an extremely good beam profile in phantom. The aims of this study were to compare the merits of FLUENTAL™ to MgF_2 / Teflon moderators and to assess the effects of Graphite and Lead reflectors on designing and building an optimal facility.

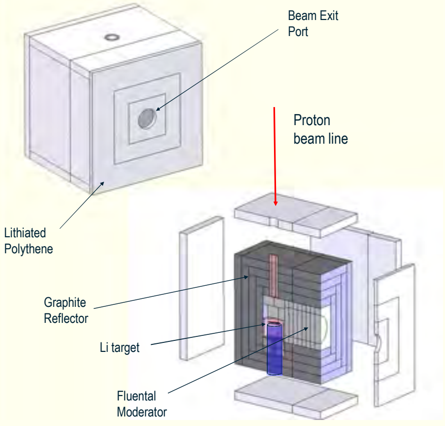

Figure 1 - The existing Birmingham NCT facility.

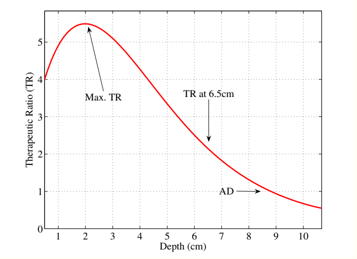

Figure 2. A schematic to illustrate the Therapeutic Ratio used to derive 3 of the Figures of Merit

The optimisation of the Beam Shaping Assembly (BSA) was carried out in three stages.

- Stage 1: Moderator and reflector design.
- Stage 2: Addition of a Thermal Neutron filter [Li-Si, 5% ^{6}Li, 5mm thick]
- Stage 3: Addition of post moderator reflector (PMR) [Lead]

At each stage only a near optimal subset of results was considered for further design considerations.

Parameter	Value
CBE Boron healthy tissue / tumour / skin	1.3 / 3.8 / 2.5
RBE Hydrogen (proton recoil: $^1H(n,n')^1H$)	3.2
RBE Nitrogen (thermal neutron capture)	3.2
RBE Photon	1
Boron ($\mu g.g^{-1}$) healthy tissue / tumour / skin	15 / 52.5 / 22.5

Table 1. Assumed values for the optimisation simulations.

Figures of Merit

The Figures of Merit (FOM) used to assess the various Beam Shaping Assembly designs are:

- Therapeutic Ratio (TR) – defined as the weighted dose to the tumour at that depth divided by the maximum weighted dose to healthy tissue.
- Therapeutic Ratio at mid-brain (i.e. 6.5 cm),
- The peak or maximum Therapeutic Ratio
- Treatment Time (the time taken to deliver a weighted dose to healthy tissue of 12.5 Gy). [based on 1mA proton beam current]
- The Advantage Depth (AD) – the depth at which the Therapeutic Ratio falls to 1.

Stage I: Beam Shaping Assembly (BSA)

The FOMs of the current Birmingham facility shown in Table 2 (**in bold**) exhibit extremely good Therapeutic Ratios and a relatively modest skin dose when compared to the other BSA materials. Improvements in all FOMs can be seen with the 21.1 cm MgF_2 / Lead assembly over the current Birmingham assembly.

Moderator / Reflector / no filter	Moderator Length (cm)	AD (cm)	TR at 6.5cm	Max TR	TT (min)	Skin Dose (Gy)
Fluental / Graphite	21.1	9.1	2.24 ± 0.02	5.08 ± 0.06	140 ± 2	15.4
Fluental / Graphite	**25.1**	**9.1**	**2.23 ± 0.02**	**5.34 ± 0.05**	**198 ± 2**	**14.6**
Fluental / Lead	21.1	9.6	2.44 ± 0.02	4.73 ± 0.07	120 ± 2	16.0
Fluental / Lead	25.1	9.8	2.75 ± 0.02	5.40 ± 0.03	176 ± 2	15.7
Fluental / Lead	27.6	9.8	2.73 ± 0.02	5.39 ± 0.06	203 ± 2	14.5
MgF_2 / Lead	18.1	9.6	2.58 ± 0.03	5.13 ± 0.05	117 ± 1	15.6
MgF_2 / Lead	21.1	9.6	2.54 ± 0.02	5.41 ± 0.06	150 ± 2	15.8
MgF_2 / Lead	25.1	9.5	2.5 ± 0.2	5.59 ± 0.05	201 ± 1	15.0

Table 2. Figures of Merit for the near optimal assemblies.

Stage II: Beam Shaping Assembly + Li-Si Filter

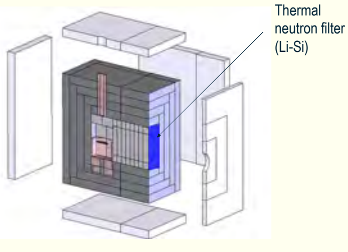

Figure 3. BSA with Li-Si filter at beam exit port.

Moderator / Reflector / with filter	Moderator Length (cm)	AD (cm)	TR at 6.5cm	Max TR	TT (min)	Skin Dose (Gy)
Fluental / Graphite	18.1	9.2	2.35 ± 0.04	4.66 ± 0.08	130 ± 2	15.6
Fluental / Graphite	21.1	9.5	2.54 ± 0.02	5.19 ± 0.03	185 ± 1	14.7
Fluental / Lead	21.1	9.7	2.55 ± 0.04	4.63 ± 0.07	135 ± 2	16.1
Fluental / Lead	25.1	>10	2.95 ± 0.03	5.36 ± 0.04	202 ± 1	15.3
MgF_2 / Lead	18.1	>10	2.76 ± 0.02	5.26 ± 0.03	146 ± 1	14.9
MgF_2 / Lead	21.1	>10	2.79 ± 0.02	5.45 ± 0.04	188 ± 1	13.1

Table 3. Figures of Merit for the near optimal assemblies with Li-Si filter.

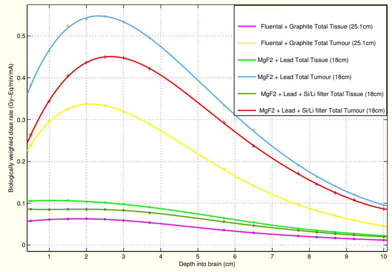

Fig. 3. Weighted Boron-Tissue, Boron-Tumour dose distributions for 18 cm of MgF_2 / Lead with and without Li-Si filter vs dose distribution for current FLUENTAL™ / Graphite assembly.

Stage III: BSA + filter + Lead Post Moderator Reflector (PMR)

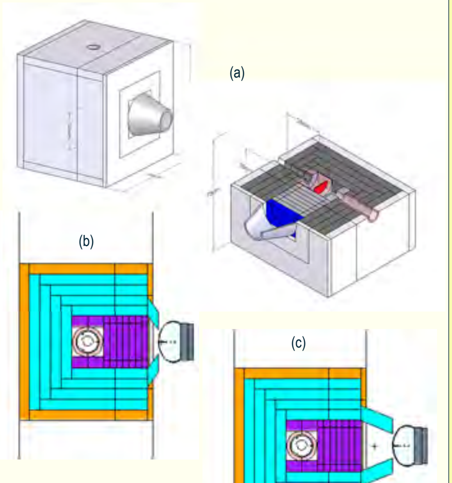

Figure 5. Optimum MgF_2 / Lead BSA and Li-Si filter with short (5cm) (b) and long (15cm) (c) post moderator reflectors.

Moderator / Reflector / with filter	Moderator / PMR Length (cm)	TR at 6.5cm	Max TR	TT (min)	Skin Dose (Gy)
MgF_2 / Lead / short PMR	21.1 / 5	3.1 ± 0.02	5.48 ± 0.03	157± 1	16.3
MgF_2 / Lead / long PMR	21.1 / 15	2.79 ± 0.02	5.54 ± 0.04	228 ± 1	12.1

Table 4. Figures of Merit for the near optimal assemblies with Li-Si filter and Post Moderator Reflector (PMR) .

It is evident from the above TRs that deeper seated tumours are better treated with the short PMR at the beam exit port. The mid-brain TR increases by a considerable 11% advantage over the filtered MgF_2 assembly without PMR and 39% over the existing facility. Treated times are severely impacted with increased PMR length as well as mid-brain TRs.

If a facility were to be designed for the treatment of ONLY shallow tumours, the TR at 6.5 cm and the AD are not as important a factor as the Max TR. Which shows very little improvement with the addition of the filter and post moderator reflector (PMR).

Discussion and Conclusion

Various compositions of beam shaping assembly have been considered for optimal dose delivery. Competing merits make it difficult to single out any one design as being optimal, especially when costs and practicality / construction are factored in. The MgF_2 / Lead assembly has a small advantage over the existing Birmingham facility (max TR has less than a 2% advantage) and shorter treatment time, but exhibits a higher skin dose.